LEIBNIZ-INSTITUT FÜR FESTKÖRPER-
UND WERKSTOFFFORSCHUNG,
BEREICH MATHEMATIK UND NATURWISSENSCHAFTEN
DER TECHNISCHE UNIVERSITÄT DRESDEN

Details of 3D electronic structure of some Fe-based superconductors and their superconducting order parameters

DISSERTATION ZUR ERLANGUNG DES
DOKTORGRADES DER NATURWISSENSCHAFTEN
(DOCTOR RERUM NATURALIUM)

Vorgelegt von Yevhen S. Kushnirenko
geboren am 16 August 1992 in Bilhorod-Dnistrovskyi

Doktorvater: Prof. Dr. Bernd Büchner

29 November 2019

Abstract

Superconductivity allows one to build unique devices, which can be used for a variety of purposes: transporting electrical power, medical examination, scientific research, electronics, etc. Since 1986, superconductivity at unexpectedly high temperature has been observed in two broad classes of materials. However, their critical temperatures are still considerably lower than room temperature, and these materials require cooling with cryogenic liquids to be superconducting. This restricts superconductivity from being widely used. Knowledge of a mechanism of superconductivity is essential for designing new materials, which superconduct at a higher temperature. However, the mechanism of high-temperature superconductivity remains unknown. Knowledge of the details of the electronic structure of existing superconducting materials can help to shed light on it.

In this thesis, we analyze the electronic structure of two materials: FeSe and LiFeAs, which belong to iron-based superconductors, a relativly new family of superconductors. To access the electronic structure, we use angle-resolved photoemission spectroscopy. In our analysis, we focus on the following aspects of the electronic structure: structure of the superconducting gap and influence of nematicity on the electronic structure.

We have revealed changes in the electronic structure of FeSe caused by nematicity in all parts of the Brillouin zone. A scale of these changes is smaller than it was believed earlier. Also, we have observed an anomalous shift of the dispersions in opposite directions with temperature in this material. We have observed anisotropic superconducting gap on all sheets of the Fermi surfaces of both: FeSe and LiFeAs. We have shown that in LiFeAs, rotational symmetry is broken in the superconducting state, which manifests not only in the gap symmetry but also in the shapes of the Fermi surfaces sheets. This result indicates a realization of a novel phenomenon of superconductivity-induced nematicity.

Contents

vi

Introduction

Superconductors are materials which can conduct electricity without dissipation (have zero resistivity) at temperatures below a certain critical temperature. Superconductors can be used for a variety of purposes. Nowadays, the prevalent application of superconductors is in strong electromagnets which are used for medical examination (MRI technique) and widely in science. Another application of superconductors is electronics, e.g., SQUID (superconducting quantum interference device) – a device which is extremely sensitive to changes of magnetic field, which is thus the best type of a magnetometer. And, of course, superconductors can be used for transporting electrical power without dissipation. However, there is one huge obstacle on the way to widespread usage of superconducting devices: low critical temperature. Superconductivity was observed for the first time in 1911 in mercury, the critical temperature of which is 4 K. After that, superconductivity was observed in many other materials. However, until the eighties of the last century, critical temperatures of all known at that time superconductors were below 30 K. To explain superconductivity in these materials, which are commonly referred to as conventional superconductors, BCS theory was developed in 1957[1]. In this theory, two electrons, which usually tend to repel each other, effectively attract each other by emitting and absorbing a phonon, which results in forming of electron pairs. In other words, one electron polarizes a crystal lattice, which consists of positively charged ions, and another electron is attracted into this area, where the positive charge was accumulated. Pairs of electrons are bosons and at low-temperature form Bose-Einstein condensate which "flows" without dissipation.

In 1986, superconductivity at 35 K was observed by J.G. Bednorz and K.A. Mueller on lanthanum barium copper oxide. This discovery started an era of high-temperature superconductors. Since that time, superconductivity at temperatures up to 134 K[2] was observed in a large number of cuprates

---

[1] This theory was developed by J. Bardeen, L. Cooper, and J.R. Schrieffer and named after them. For this theory, they were awarded the Nobel Prize in Physics in 1972.

[2] This temperature still is a record of superconductivity at ambient pressure. Under higher pressure, a critical temperature can be higher. However, the difference is not so large, and the

(copper-oxide-based superconductors). This was a big step forward. Nevertheless, we are still far away from our "Holy Grail": superconductivity at room temperature. Another family of high-temperature superconductors, which was discovered in 2008, is Fe-based superconductors. However, neither cuprates nor Fe-based superconductors obey BCS theory, and no another universally accepted scenario for superconductivity in high-temperature superconductors still has been developed. This means we do not know how it works and as a consequence are not able to design entirely new superconducting compounds with high critical temperatures in order to make a dream of room-temperature superconductivity come true. We have only some hints which point the way of modifying existing materials for increasing critical temperature and help to predict the presence/absence of superconductivity in other members of the existing families.

Now, after discovery of Fe-based superconductors, we have more chances to disentangle this complicated problem, since we can compare the two families. They are, on the one hand, similar (e.g., both of them are layered materials) and, on another hand, different (e.g., electronic structure of Fe-based superconductors is way more complex).

In this work we investigate Fe-based superconductors using angle-resolved photoemission spectroscopy. This experimental technique allows one to measure the electronic structure of material directly (both energy and momentum of an electron are resolved). Electronic interactions, which are possible candidates for the role of a glue helping electrons to form pairs in high-temperature superconductors, change an electronic structure of a material in both normal and superconducting state. So, investigation of the electronic structure with angle-resolved photoemission spectroscopy is important for solving the mystery of high-temperature superconductivity.

This thesis

In this work angle-resolved photoemission spectroscopy studies of LiFeAs and FeSe, which are high-temperature Fe-based superconductors, are presented. Here, we focus on the following aspects of the electronic structure of these materials: structure of the superconducting gap and influence of nematicity on the electronic structure.

---

necessity of applying pressure makes these materials even less appealing for employment in real devices.

In the first chapter, we present a background of our study. It includes general information about superconductivity and other properties of iron chalcogenides and iron pnictides as well as more detailed information about properties of LiFeAs and FeSe obtained by various experimental techniques.

In the second chapter, we describe the experimental technique. This chapter includes an introduction into the theory of photoemission, a description of central units of a typical angle-resolved photoemission spectroscopy setup (analyzer, light sources, manipulator, vacuum enclosure), a description of sample preparation, and technical specifications of a setup with which the majority of the results was obtained.

In the third chapter, we track a temperature evolution of the electronic structure of FeSe from several Kelvins up to almost room temperature. Observed changes can be divided into two groups: (i) rapid changes related to a nematic transition[3] at ∼90 K, and (ii) gradual shifts of the dispersions with temperature. We observed an influence of nematicity on all dispersions which cross the Fermi level and show that the scale of this influence was strongly overestimated. Concerning gradual shifts, we show that they are observed in both temperature ranges (bellow and above the nematic transition). These shifts are different for different dispersions.

In the fourth chapter, we analyze the structure of the superconducting gap in FeSe on all its Fermi surfaces. We analyze data sets measured with different photon energies which allow us to access parts of the Brillouin zone with different k_zs[4]. We present the first evidence for a presence of the superconducting gap on electron pockets of the Fermi surfaces of FeSe from a photoemission experiment. We show that the gap on all pockets of the Fermi surfaces is anisotropic. At the end of the chapter, we compare our experimental results with existing theories in order to identify the nature of the gap anisotropy in this material.

In the fifth chapter, we analyze the electronic structure and the gap function of LiFeAs. We show that in this material at low temperatures rotational symmetry is broken: both Fermi surface and gap function have two-fold symmetry. The difference between dispersions which corresponds to two orthogonal directions is present not only near the Fermi level but also at higher binding energies. Measurements at higher temperatures show that in the normal (non-superconducting) state this difference disappears. We argue that the observed result is a manifestation of a novel phenomenon of

---

[3]A definition of the nematic transition in iron-based superconductors and a description of the effect can be found in subsection 1.1.5.

[4]Out of plane component of momentum.

superconductivity-induced nematicity.

Chapter 1

Iron-based superconductors

1.1 Introduction to iron-based superconductors

Superconductivity in iron pnictides was discovered in 2006 [1]. It was LaOFeP with a critical temperature $T_c \sim 5$K. In 2008 LaO$_{1-x}$F$_x$FeAs with $T_c = 26$K was discovered [2]. This temperature is higher than 23K, which was a record temperature before the discovery of Cu-based superconductors in 1986 [3]. This fact allowed one to call LaO$_{1-x}$F$_x$FeAs a high-temperature superconductor and attracted interest of many researchers to it and to similar compounds. In the next few years, superconductivity with a critical temperature up to 55K [4] was found in many iron-based superconductors (IBS) compounds. These results, even more, stimulated the interest in this class of materials.

1.1.1 Crystallographic structure

Like cuprate superconductors, Fe-based superconductors have a layered structure. All of them have common iron-pnictogen or iron-chalcogen plane. On this bases high-temperature Fe-based superconductors can also be divided into 2 classes: if they contain pnictogen (P, As), they are called "iron pnictides", if they contain chalcogen (S, Se, Te), they are called "iron chalcogenides". On the another hand, IBS can be classified according to their crystallographic structure type. They can be divided into 4 main families: "11" (FeSe, FeTe and FeS), "111" (AFeAs where A is an alkali metal), "122" (XFe$_2$As$_2$ where X is an alkaline earth metal and A$_x$Fe$_{2-y}$Se$_2$ where A is an alkali metal) and "1111" (XFe$_2$As$_2$ where X is an alkaline earth metal). Crystallographic structures of these families are shown schematically in Fig 1.1. The lattice parameters can be determined by X-ray diffraction or neutron diffraction experiments. Knowing the lattice parameters one can make predictions regarding the properties of the material, sometimes even including superconducting

properties. For instance, a correlation between the bond angle of the As-Fe-As layer and the temperature of superconducting transition has been empirically established in iron pnictides: the highest T_c corresponds to the structure in which iron atom and its four arsenic neighbors form an ideal tetrahedron (the bond angle is 109.5 degrees) [5]. A similar correlation was also observed in FeSe [6].
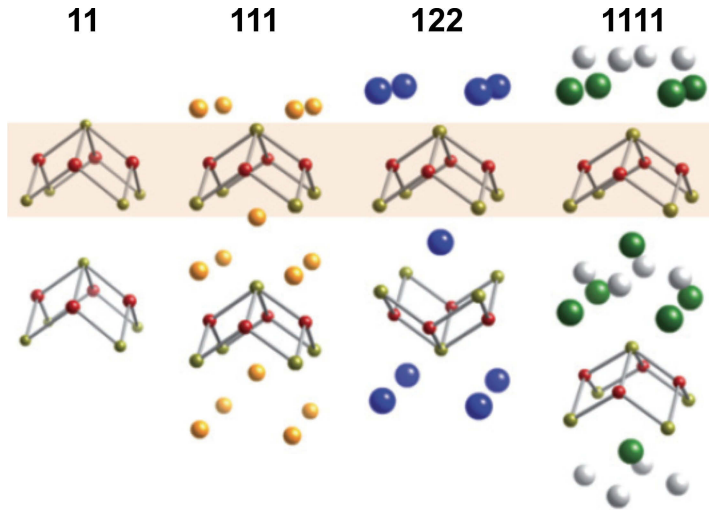

FIGURE 1.1: Crystallographic structures of the iron-based superconductors, adapted from [7]

1.1.2 Electronic structure

Early density functional theory calculations using local density approximation (LDA) for iron-based superconductor shown that the part of their electronic structure near the Fermi level are formed exclusively by $3d$ orbitals of iron: d_{xy}, d_{xz} and d_{yz} (as an example, see the results of the calculations for LaFeAsO in Fig.1.2(a)). For a single iron atom (1-Fe) unit cell, there are three hole-like dispersions in the center of the Brillouin zone (BZ) ($\tilde{\Gamma}$ point) and two of them cross the Fermi level forming two circular Fermi surfaces. Electron-like dispersions near the boundaries of the BZ ($\tilde{X}$ point and $\tilde{Y}$ point) form elliptical pockets (see Fig.1.2(b)). Such 1-Fe Fermi surface is often used in theoretical studies. However, real unit cell contains two atoms of iron because a half of the pnictogen (chalcogen) atoms is above the iron plane and another half of them is below it (see Fig.1.1). Because of this, real BZ and, as a consequence, Fermi surface are folded and become two times smaller. In such a 2-Fe BZ the bands from parts near $\tilde{X}$ point and $\tilde{Y}$ point overlap and form two elliptical Fermi surfaces in the corner of new BZ (M point)(see Fig.1.2(c)). An orbital character of the dispersions and Fermi surfaces formed by them is depicted with a color of arrows and contours on Fig.1.2. Here we

have shown results for LaFeAsO, but for other IBS calculations show a very similar electronic structure. The only quantitative difference with electronic structure calculations is a position of d_{xy} hole-like dispersion. It can cross the Fermi level and form one more hole-like Fermi surface or be below it. However, it varies not only for different materials but also from study to study e.i. in modern calculations [8] of LaFeAsO it is shown, that this band crosses the Fermi level as well as in FeSe from "11" family, LiFeAs from "111" family and $BaFe_2As_2$ from "122" family (see Fig.1.3). d_{xy} hole-like dispersion forms circular Fermi surface in the corner of 1-Fe BZ which moves to the center in 2-Fe BZ (shown with the dashed contour in Fig.1.2(b) and (c)). Further in this thesis, I will refer to 2-Fe BZ. I will explicitly mention the difference when mentioning both types of the BZ.
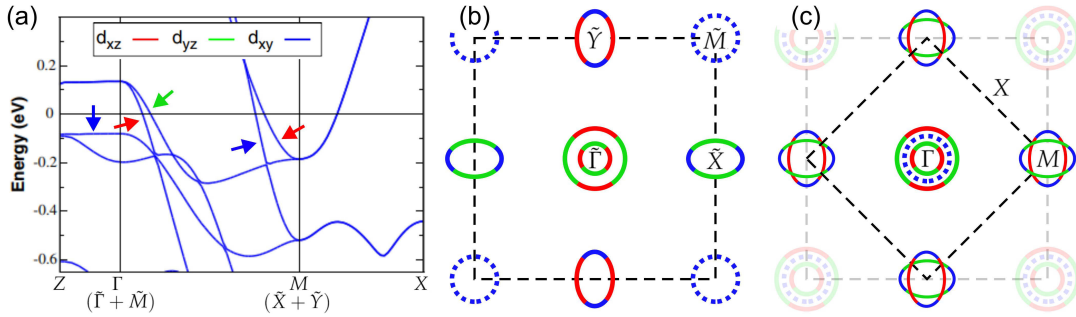
FIGURE 1.2: Electronic structure calculations for LaFeAsO (a) and schematic Fermi surface of IBS for 1-Fe unit cell (b) and 2-Fe unit cell (c). Here color of arrows on (a) and contours on (b) and (c) depict orbital character of the dispersions, dashed lines show borders of the BZ. (a) adapted from [9]. (b) and (c) inspired by [10]

However, the electronic structure observed already in early ARPES data showed a different picture. There are also three hole-like and two electron-like dispersions near the Fermi level. Though, there are two essential distinctions between calculated electronic structure of IBSs and an experimental one, which is observed in ARPES: a band renormalization and a shift of the dispersions with respect to each other and the Fermi level. Strong renormalization was observed in different IBS [11, 12, 13, 14, 15, 16]. As it was shown for NaFeAs in [11], dispersions in the bottom of the valence band, between 2 and 5 eV binding energies almost match the calculated dispersions, which correspond to the $4p$ bands of arsenic. They are located at the same binding energies and have the same bandwidth. Unlike these dispersions, the dispersions near Fermi level, which correspond to the $3d$ bands of iron, are heavily renormalized. Moreover, this renormalization is orbital-dependent and for some bands can be as big as 9 (d_{xy} dispersion in FeSe

FIGURE 1.3: Electronic structure of IBS upturned by the LDA calculations using the linear muffin-tin orbital method. Blue and grey lines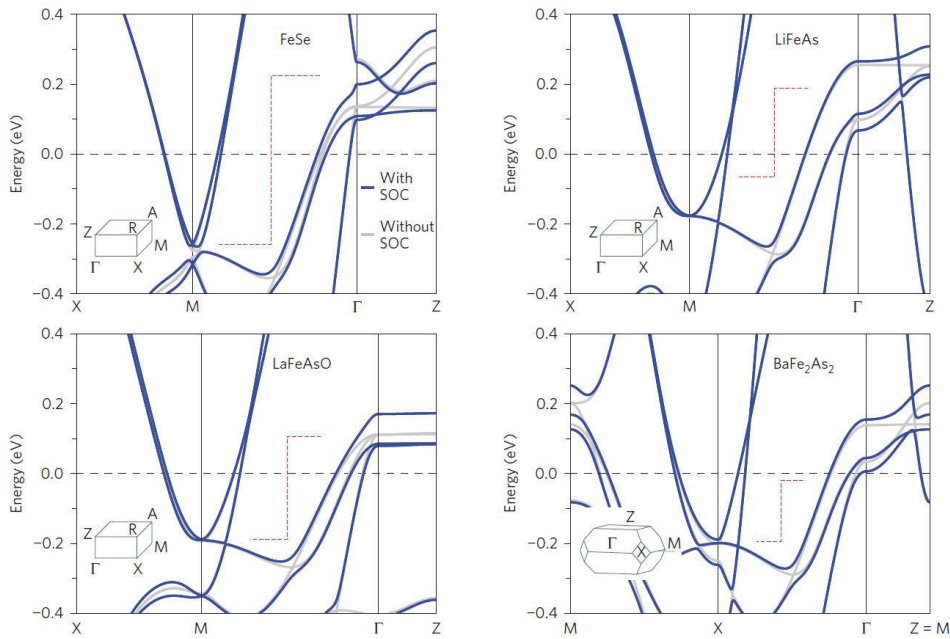 represent results of calculations with and without spin-orbit coupling included respectively. Horizontal parts of the red dashed lines depict an approximate position of the experimental Fermi level position near the center and the corner of the BZ obtained in ARPES.
Adapted from [8].

[13]). Analysis of ARPES spectra of NaFeAs presented in Ref.[11] shows that observed renormalization cannot be explained just by phonons and/or spin-fluctuations since the corresponding bosonic spectrum is not extending to energies as height as 500 meV, which is needed for such a renormalization. It is proposed, that the best candidate is Hund's coupling J [17, 18, 19] instead. Another intrinsic distinction from calculations is a band shift. In the experimental electron structure, hole-like dispersions are shifted down to higher binding energies, and electron-like dispersions are shifted up to lower binding energies. This effect is usually called "red-blue" shit[1]. As well as band renormalization, red-blue shift is generic for all IBS [20, 21, 22, 12, 13, 8, 23]. Such band shift leads to the proximity of the Fermi level to the tops/bottoms of the dispersions (see red dashed lines in Fig.1.3) and, as a consequence, to the shrinking of the Fermi surface. Such proximity of the tops/bottoms of the dispersions to the Fermi level is important for superconductivity (see section 1.1.6). There are several theoretical approaches which attempt to describe the red-blue shift. It can be described in terms of electronic instability called

---

[1]Analogy to red/blue shit of photons. Which is a shift of their energy to lower/higher energies and is caused by gravity or Doppler effect.

Pomeranchuk effect [24, 25, 26, 27, 28]. Another approach which describes the red-blue shifts is based on the renormalization of the bands by spin fluctuations [29, 30]. As one can see from Fig.1.3, the red-blue shift results not only in a reduction of the pockets size but also in vanishing of some pockets, since the tops of the dispersions which form them move to another side of Fermi level. Nevertheless, experimental Fermi surface of most of IBS has at least one hole pocket in the center, and one electron pocket in the corner of the BZ[2].

1.1.3 Phase diagram
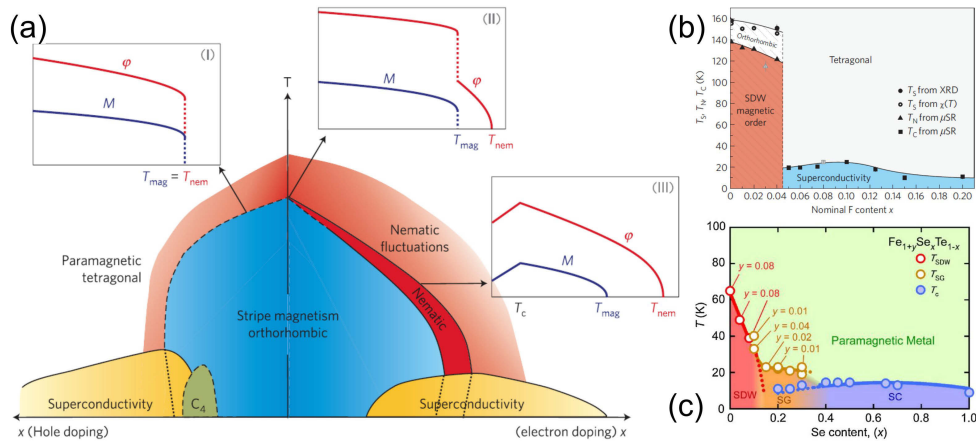
FIGURE 1.4: (a) Schematic phase diagram of $BaFe_2As_2$. For quantitative phase diagram of $BaFe_2As_2$ on electron-doped side, see Ref.[34, 35] and on hole-doped side, see Ref.[35]. (b) phase diagram of $LaO_{1-x}F_xFeAs$. (c) phase diagram of $FeTe_{1-x}Se_x$.
(a) adapted from [36]. (b) adapted from [37]. (c) adapted from [38]

Fig.1.4 shows examples of the phase diagrams for materials from 3 different families of IBS. As one can see, at high temperature all these materials are paramagnetic metals with tetragonal symmetry of the lattice. Usually, the pristine parent compounds of IBS are not superconducting at any temperatures. They become superconducting if elements which add electrons or holes are substituted into the material. Such substitution is called a hole(electron) doping. In some cases substitution with element, which has the same valence, also can make material superconducting, as it is for $FeTe_{1-x}Se_x$ (see Fig.1.4(c)). Another interesting thing which can be seen in

---

[2]It is the case for optimally-doped (level of doping at which T_c is maximal) superconductors, under-doped superconductors and parent compounds which are usually not superconducting. Nevertheless, in some rare cases of over-doped compounds which still remain superconducting, electron pockets or hole pockets can be absent [12, 31, 32, 33]. Such superconductors are not considered in this thesis.

Fig.1.4(c) is its right part, which corresponds to pristine FeSe and is inside the superconducting dome. In other words, FeSe is stoichiometric superconductor which, as mentioned earlier, is not typical. Also, some materials can become superconducting under pressure [39] or, if a material is already superconductor, pressure in some cases can increase T_c. Another two phases which usually present on a phase diagram are a magnetically ordered phase and a nematic phase in which magnetic order is not developed yet, but rotational summery is already broken. These phases usually can be observed in pristine and slightly doped materials. In the next three subsections, we will discuss these three phases (magnetic, nematic, and superconducting).

1.1.4   Magnetism

Phase diagrams in Fig.1.4 show that parent compounds of IBS usually become magnetically ordered below a specific temperature. A typical spin structure of IBS in the magnetically ordered phase is shown in Fig.1.5. It can be described as stripe order, here spins are aligned antiferromagnetically in one direction and ferromagnetically in the other. This magnetically ordered phase usually called a spin-density wave (SDW). Such naming stresses that the magnetism is of itinerant electrons rather than of localized electron spins [40]. It is believed that nesting between electron pocket and hole pocket of the Fermi surface with commensurate vector (π, π) that matches magnetic ordering vector observed in parent compounds of IBS[3] is the origin of magnetic ordering. This statement is supported by experimentally observed correlation of presence of the SDW and nesting: In parent compounds from 122 family and NaFeAs were nesting is good SDW is observed and in doped members of 122 family and LiFeAs where nesting is absent or poor SDW is also absent (see Ref.[41] (and references in it), Ref.[42] and Ref.[43]).

1.1.5   Nematicity

The nematic transition in iron-based superconductors is a transition under which the spatial directions x and y became non-equivalent which breaks the rotational symmetry of the lattice which transforms from tetragonal to orthorhombic. The time-reversal symmetry and translational symmetry are preserved under this transition. This makes the order parameter for this transition similar to the order parameter in the nematic phase of liquid crystals.

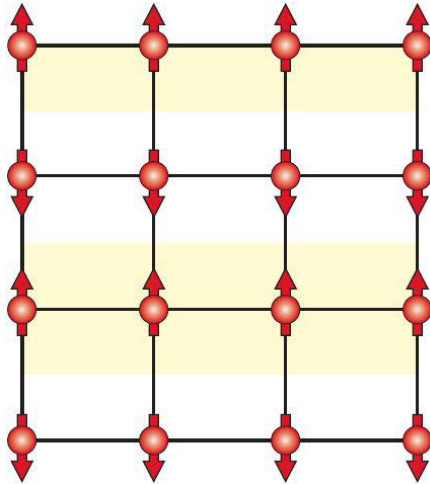[3]Except of ordering magnetic vector in FeTe which is $(\pi, 0)$.

FIGURE 1.5: A spin structure in the stripe magnetically ordered phase. The arrows representing magnetic moment directions.
Adapted from [44]

Because of this similarity, the orthorhombic phase of the iron-based superconductor is called the nematic phase, and the transition between tetragonal and orthorhombic phases is called the nematic transition. In some compounds e.g. Co-doped $BaFe_2As_2$, the nematic transition and magnetic transition occur at different temperatures, when in some other compounds e.g. K-doped $BaFe_2As_2$ they occur simultaneously[45]. With changing a doping level, the temperature of the nematic transition (T_{nem}) behaves in the same way as the temperature of the magnetic transition (T_{mag}) approaching the superconducting dome. This shows that nematicity and superconductivity are interconnected. Indeed the theoretical studies (see Ref.[46, 47]) show that nematic fluctuations can mediate superconductivity. Therefore it is important to understand the origin of this order as it may influence the superconductivity.

However, it is still unknown what does drive the nematic transition. One can think this transition as a regular structural transition driven by phonons. However, theoretical studies show that this transition more likely is driven by electronic degrees of freedom [48, 49]. This theoretical result is supported by experimental results, e.g. transport measurements on detwinned samples[4] show that anisotropy of the d.c. resistivity anisotropy is considerably larger than the lattice anisotropy [48, 49].

To describe the nematic phase, one should identify the appropriate order parameter. Nematic order has three experimental manifestations, each of them is associated with a different origin of this state [36]. (i) Structural distortion: in-plane lattice parameters a and b become different [50]. Such

---

[4]It means that almost all domains are oriented in one direction. This can be reached by applying strain to the sample.
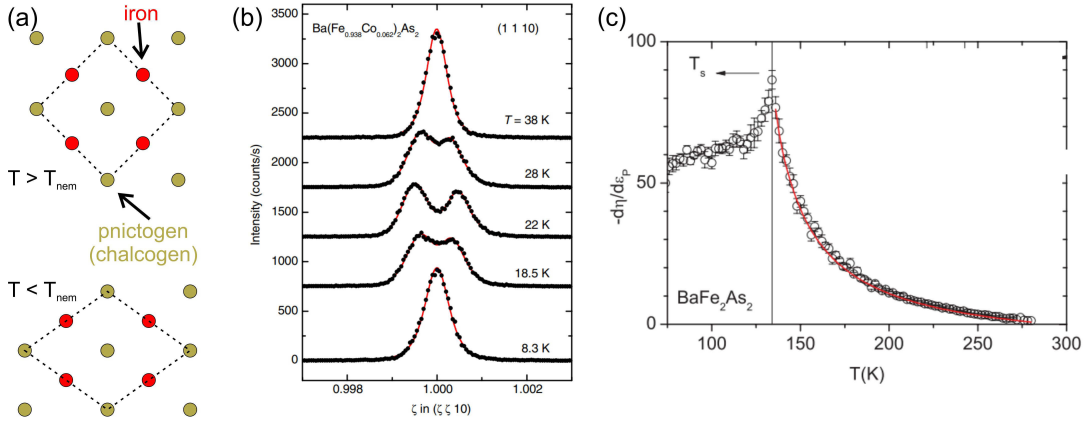
FIGURE 1.6: (a) schematic representation lattice deformation under the structural transition in iron-based superconductors (only iron-pnictogen/chalcogen plane is shown). Dashed line depict borders of 2-Fe elementary cell. (b) Temperature evolution of the (1 1 10) Bragg peak splitting, in Co-doped $BaFe_2As_2$. (c) Temperature dependence of the nematic response in $BaFe_2As_2$. (b) adapted from [34]. (b) adapted from [53]

an order typically points to a phonon-driven scenario of the structural transition. (ii) Orbital order: the occupations of the d_{xz} and d_{yz} orbitals become different [51]. Such an order typically points to charge fluctuations. (iii) Spin order: the static spin susceptibility becomes different along the q_x and q_y directions in the reciprocal space at temperatures above T_{mag} at which conventional SDW state is not developed yet [52]. Such an order typically points to quadrupole magnetic fluctuations.

At this moment we face a dilemma: all three types of order are present in the nematic phases, since the development of one of them necessarily induces the other two [36], and it is not clear which order parameter is the primary one and, as a consequence, a type of fluctuations responsible for the nematic instability is also unknown.

Most of the experimental results show that the nematic transition is electronically driven: as it has been already mentioned, measurements of the resistivity anisotropy on detwinned samples [48, 49, 54] show that this anisotropy is significantly larger than the relative distortion of the lattice. This result is inconsistent with the structural scenario. ARPES measurements detected energy shift between d_{xz} and d_{yz} orbitals in the orthorhombic phases in detwinned samples as well as in non-detwinned samples [51, 55, 56, 57, 58, 42]. This result indicates the orbital order. Another evidence that the nematic transition is electronically driven is a suppression of nematicity in the superconducting phase. It manifests in decrease of lattice distortion observed by X-ray diffraction measurements[34] (see Fig.1.6(b)) and in decrease of the

splitting of ^{77}Se NMR lines which is caused by nematicity [59]. These results are in a good agreement with the electronic scenario since in this case, such a suppression can be a result of the competition for the electronic states between two orders, both of which are electronically driven. Another strong evidence for the electronic scenario has been observed in measurements of the resistivity anisotropy Ref.[53]. In this study dependence of the relative change of resistivity $\eta = \Delta\rho/\rho_0$ on strain $\varepsilon = \Delta L/L$ (the relative change of length along the current direction) was measured at different temperatures. It was shown that the nematic response $\partial\eta/\partial\varepsilon$ diverges near the temperature of the nematic transition (see Fig.1.6(c)). This indicates that structural distortion is not the primary order parameter. Otherwise, the relative change of resistivity on strain dependence should be the same for all temperatures.

In order to disentangle two electronic scenarios: orbital one and magnetic one, the experimental results should be compared with the results for microscopic models for these scenarios. Theoretical study for the magnetic scenario[60] predicted three possible types of system behavior, which are realized for different values of the nematic coupling. (i) In the case of strong nematic coupling, nematic and magnetic transitions are first-order transitions and occur simultaneously. (ii) In the case of intermediate nematic coupling, the nematic transition is a second-order transition, and magnetic one occurs together with a so-called meta-nematic transition at lower temperature. (iii) In the case of weak nematic coupling, nematic and magnetic transitions are second-order transitions and occur at different temperatures ($T_{mag} < T_{nem}$). The microscopic calculations found that the nematic coupling decreases with electron doping[36]. This is in a perfect agreement the experimental results: all three predicted types of behavior could be found on the phase diagram of $BaFe_2As_2$ which is based on the experimental results (see Fig.1.4). In pristine $BaFe_2As_2$, the second-order nematic transition followed by a meta-nematic transition and magnetic transition at a lower temperature was observed [50, 52, 61], which is a second type of behavior. In hole-doped $BaFe_2As_2$, nematic transition and magnetic transition occur simultaneously [45], which is a first type of behavior. In electron-doped $BaFe_2As_2$, nematic transition and magnetic transition are split ($T_{mag} < T_{nem}$), which is a third type of behavior.

The results of resistivity anisotropy measurements also favor spin-driven nematic order scenarios. Orbital order and spin-driven nematic order influence on the resistivity in different ways in the nematic state. Orbital order causes anisotropy in Drude weight, and spin-driven nematic order makes the scattering rate anisotropic. The calculated magnetic scattering rate anisotropy

is in agreement with experiment [62], whereas the calculated the Drude weight anisotropy has the opposite sign to the one observed experimentally [63, 64].

Interestingly, electronic nematic phases have also been proposed in cuprate superconductors and heavy-fermion materials. [65]

1.1.6   Superconductivity

As it was said before, IBS can exhibit superconductivity at temperatures up to 55K in bulk samples [4] and even higher, up to 100K, in single-layer of FeSe on strontium titanate substrate [66, 67]. Nature of superconductivity in this class of material is unknown. BCS theory which successfully describes super-conductivity in conventional superconductors does not succeed in describing of superconductivity in IBS. First-principles studies predict T_c in these materials is $\approx$ 1 K in case of the conventional phonon-mediated scenario of superconductivity which is considerably smaller than critical temperature observed by experiments. Since phonons unable to explain such high T_c, screened Coulomb interaction become a most likely source of the pairing. In general, this interaction is a repulsion. However, the theoretical possibility of superconductivity which originates from repulsive electron-electron inter-actions was observed a long time ago [68, 69]. Indeed, at short distances, the screened Coulomb interaction is repulsive, but at large distances it ex-hibits complex behavior and can have attractive components[5]. In this case excitations responsible for pairing are either spin fluctuations or charge fluc-tuations. In the conventional case of interaction with slow ions of the lattice, retardation in time can be realized. In contrast to ions, electrons are fast; thus the electronic fluctuations exist on the same time scales as the motions of the electrons which are expected to be paired. So, in this case, the electrons avoid each other in space rather than time in order to escape the effects of the repulsive Coulomb interaction. Coupling via such attractive components of Coulomb interaction leads to a highly anisotropic gap function. It often contains areas on the Fermi surface with a different sign [40]. In the cuprates, this results in a d-wave symmetry of the gap with nodes (zero gap regions) at $k_y = \pm k_x$.

In IBS, which in contrast to cuprates are multiband systems, a gap with s-wave symmetry can be potentially realized if the gap sign remains the same

---

[5]If the interaction between the two fermions can be expended in a set of components which correspond to interactions in the subspaces with a given angular momentum of the two interacting fermions, one can factorize the BCS gap equation and write it as a set of equations for each pairing channel.[68] One attractive component is enough to induce su-perconductivity in the system.
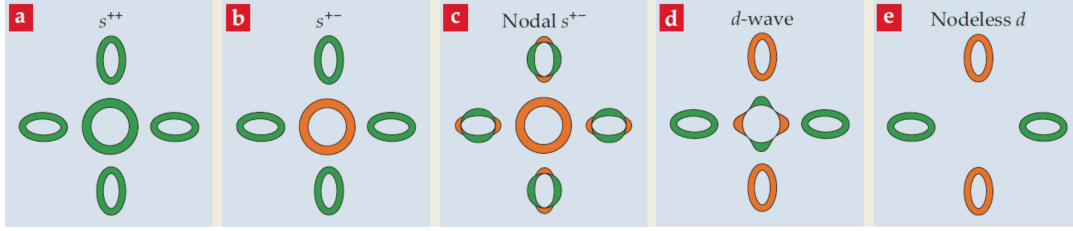
FIGURE 1.7: Schematical representations (for 1-Fe BZ) of various gap symmetries possible in IBS. Here different colours represent different sign of the gap.
Adapted from [40].

on each sheet of the Fermi surface. However, the gap sign is expected to be different on the different sheets of the Fermi surface [9] (see Fig.1.7(b)). Such gap symmetry is called s^{+-} or enhanced s-symmetry. The s^{+-} gap could occur it a system where repulsion between pockets is stronger than within them. This is possible if interpocket interactions between electron and hole pockets are enhanced due to spin fluctuations. This additional interaction is essential since the usual screened Coulomb interaction is weaker between pockets than within them.[40].

There is a popular opinion, that in lightly and optimally doped IBS the gap has s^{+-}-symmetry. The strongest evidence for s^{+-}-symmetry of the gap is the results of inelastic neutron scattering experiment [70] in which resonance peak in the superconducting spin-excitation spectrum was observed. This result indicates that a sign of the gap on hole and electron pockets are different. Also, the presence of a region of coexistence of magnetic ordering and superconductivity in the IBS evidence for s^{+-} gap, because the first-order transition between these two states is more likely for s^{++} gap. Nevertheless, various studies show that the physics of the pairing is more complicated than it was thought as a result of the multiorbital/multiband nature of fermionic excitations [71]. Both, the symmetry and the structure of the gap, arise from a nontrivial interplay between intraband Coulomb interaction, spin-fluctuation exchange, and the momentum structure of the interactions. Because of this, besides s^{+-}-symmetry, s^{++}-symmetry and d-symmetry can be realized in IBS.

s^{++}-wave gap is another name for conventional s-wave gap, which does not change a sign on different parts of the Fermi surface. Such gap symmetry is peculiar to phonon scenario, but can be realized not only in this case. In the framework of the electronic scenario, s^{++}-wave gap can emerge if the interpocket interaction is again dominated, but this interaction should be attractive rather than repulsive. It was shown, that in case of Fe-site substitution

in iron-pnictides orbital fluctuations can give rise to a sign-preserving s^{++}-wave pairing [72, 73, 74]. Another gap symmetry which can be realized in IBS is d-wave symmetry. The origin of d-wave pairing can be a repulsive interaction between the two electron pockets. Assuming that this interaction is stronger than other interactions, one obtains another case of plus-minus symmetry, when the sign of the gaps changes between the two electron pockets [75, 76, 10]. Such symmetry when the superconducting gap changes sign under a $\pi/2$ rotation in momentum space is d symmetry. d-wave symmetry is most likely a symmetry of the gap in strongly electron-doped IBS for which the interaction between electron and hole pocket is relatively small [71].

Here I should notice, that nodes are not inherent and unique feature of d-wave gap. There are cases when the gap with s^{+-} symmetry has nodes and when the gap with d symmetry does not have nodes [40, 71]. In case of s^{+-} symmetry gap can switch its sign on electron pockets and, as a consequence, form nodes on them (see Fig.1.7(c)). Nodes in d-wave gap are expected on a hole pocket. So, if all hole pockets disappear (in case of strong electron doping) d-wave becomes nodeless (see Fig.1.7(e)). The latter case is particularly interesting: since hole pocket is absent but superconductivity still present [77], the normal scenario of superconductivity in IBS which involves both types of pockets and spin fluctuations can be eliminated. This means that at least in some cases an interaction between the two electron pockets (one at $\tilde{X}$ point and one at $\tilde{Y}$ point of 1-Fe BZ) is strong enough to cause superconductivity.

An empirical correlation between the electronic structure and critical temperature which is generic for all families of IBS was observed: T_c is maximal
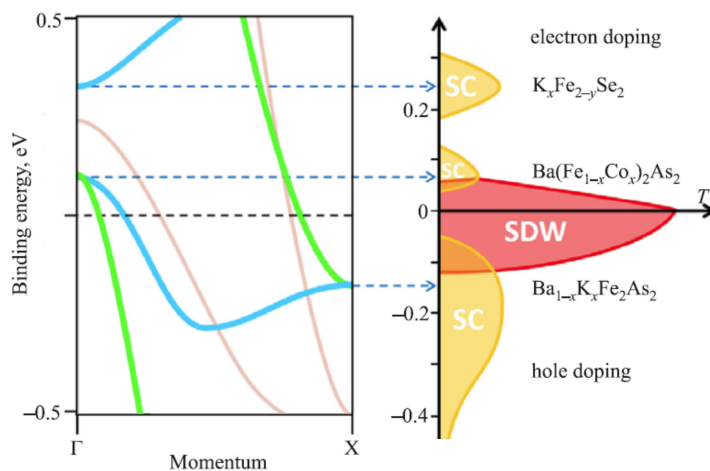

FIGURE 1.8: Schematic band structure and phase diagram. Here, blue dashed lines represent Fermi level position for different optimally doped compounds and arrows point to parts of the phase diagram to which they correspond.
Adapted from [78]

when the electronic structure is close to Lifshitz transition[6] [12, 78]. The proximity of Lifshitz transition also means that Van Hove singularity which in this case is an edge of the band (top of a hole-like one or bottom of an electron-like one) is close to the Fermi level. The electronic structure which is close to Lifshitz transition was observed for the optimally hole-doped members of 122 family ($Ba_{1-x}K_xFe_2As_2$, $Ba_{1-x}Na_xFe_2As_2$, and $Ca_{1-x}Na_xFe_2As_2$) [20, 80, 81, 82, 83], electron-doped member of 122 family ($Ba(Fe_{1-x}Co_x)_2As_2$) [12, 84], member of 111 family (LiFeAs and NaFeAs which exhibit the highest T_c without doping) [14, 15, 85, 86, 87]. Interestingly, T_c is increasing with the number of band-edges near the Fermi level: $(CaFeAs)_{10}Pt_{3.58}As_8$ has three band-edges near the Fermi level and $T_c = 35$ K while critical temperature of $(CaFeAs)_{10}Pt_{3.58}As_8$ which has only one band-edges near the Fermi level is 15 K. Optimally doped members of 1111 family ($SmFe_{0.92}Co_{0.08}AsO$ and $NdFeAsO_{0.6}F_{0.4}$) also have 2–3 band edges near the Fermi level [88, 44]. Perhaps, such a correlation between Lifshitz transition and T_c can be explained via shape resonance effects [89, 90, 91, 92, 93, 94].

1.2   LiFeAs - special iron-based superconductor

Lithium iron arsenide (LiFeAs) is one of the most intriguing superconductors. This compound was synthesized in 2008 by several groups simultaneously [95, 96]. Together with NaFeAs it represents the main members of "111" family of IBS and has a typical crystallographic structure (see Fig.1.9(a)): it is tetragonal, with the lattice parameters $a = b \approx 3.77$Å and $c \approx 6.35$Å, obtained from X-ray diffraction experiments [97, 95, 98]. Because of the presence of lithium on the surface, the single crystals of LiFeAs are sensitive to moisture in the air. Therefore, single crystals should be grown, stored, transported and measured in noble gas atmosphere or vacuum. LiFeAs is stoichiometric compound, which means that it nominally does not have defects, e.g. vacancies or substituted atoms, and elemental composition can be represented by integers. The material superconducts at temperatures below 18K (see [95, 14]) without the chemical doping or applying pressure. This fact makes LiFeAs very special, since most of IBS members become superconducting when other atoms provide additional charge carriers or isovalently substituted or pressure is applied [39]. Interestingly, LiFeAs shows just the opposite behavior: applying pressure suppresses superconductivity, as was

---

[6]Lifshitz transition – transition under which Fermi surface changes its topology.[79]

demonstrated by the resistivity measurements [99, 100]. In addition, super-conductivity in LiFeAs can also be suppressed by electron doping. Studies of LiFe$_{1-x}$Co$_x$As (Ref. [101, 102, 103]) show T_c decreasing with increasing the Co concentration x with the superconductivity vanishing at $x \approx 0.17$.
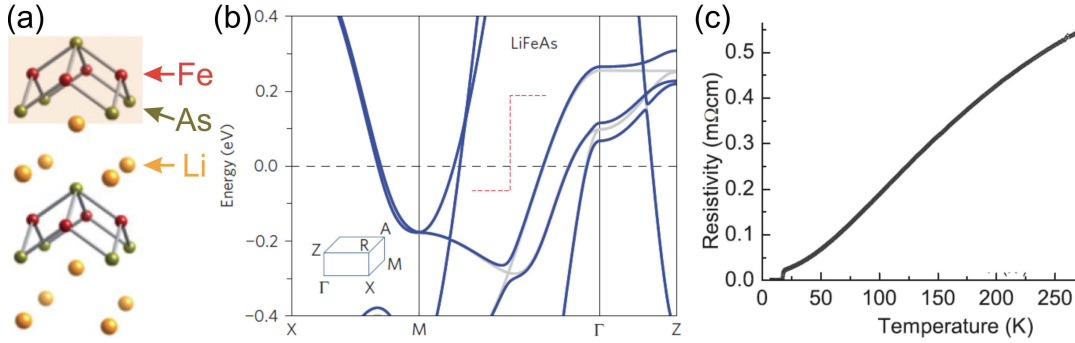
FIGURE 1.9: (a) crystallographic structure of LiFeAs. (b) calculated electronic structure of LiFeAs. Blue and grey curves show results of calculations with and without spin–orbit coupling respectively. (c) temperature dependence of in-plane resistivity of LiFeAs. (a) adapted from [7]. (b) adapted from [8]. (c) adapted from [104].

The first band structure calculations (see [105, 106]) yielded low-energy electronic dispersion, shapes of the Fermi surfaces and densities of states similar to those, found for the members of "1111" and "122" families. These calculations also predicted that LiFeAs should have an antiferromagnetic ground state, as in the case of "122" and "1111" systems, due to the SDW instability. However, resistivity and susceptibility experiments did not show any evidence for the magnetic transition [107, 95, 97, 104]: ρ(T) dependence showed only a rapid drop at ∼18K, indicating a superconducting transition Fig.1.9(c)). This is in contrast to undoped BaFe$_2$As$_2$, SrFe$_2$As$_2$ and LaOFeAs, which undergo a SDW transitions at 140 K, 200 K and 135 K respectively with a peculiar ρ(T) dependence near these characteristic temperatures [2, 108, 109, 110, 111]. Muon-spin rotation experiments also have not confirmed the presence of SDW state [112]. The absence of SDW state is thus another qualitative distinction of LiFeAs from most of IBS.

Fig.1.10(a) shows one of the first Fermi surface maps of this material measured with ARPES [14]. More recent ARPES studies show similar results [85, 113]. At least three pockets can be seen on this map: one small dumbbell-like pocket in the center of the BZ, one big barrel-like pocket around it and roundish pocket in the corner of the BZ. The last one is actually a superposition of 2 pockets which can be seen from the more detailed map measured using photons with lower energy [8] 1.10(c). Panels of Fig.1.10(b) show spectra measured along the momentum cuts passing through the pockets located

in the center and in the corner of the BZ. Both directions are indicated on the map with white lines. They show that there are two electron-like dispersions in the corner of the BZ, which cross Fermi level and 3 hole-like dispersions in the center. The outer hole-like dispersion always crosses the Fermi level forming a big pocket. The inner one never (at all k_z-s) crosses Fermi level, but the middle one can either cross the Fermi level at certain k_z-values and thus forms a small hole-like Fermi surface or runs just be very close to it. This can be seen from Fig.1.10(d) and (e) which were measured with different photon energies (25 eV and 36.5 eV). These energies approximately correspond to Γ and Z points in 3D BZ. This electronic structure mostly matches up with the calculated one (see Fig.1.9(c)), provided the global renormalization by the factor of 3 is applied with subsequent "red-blue" shifts (see section 1.1.2).
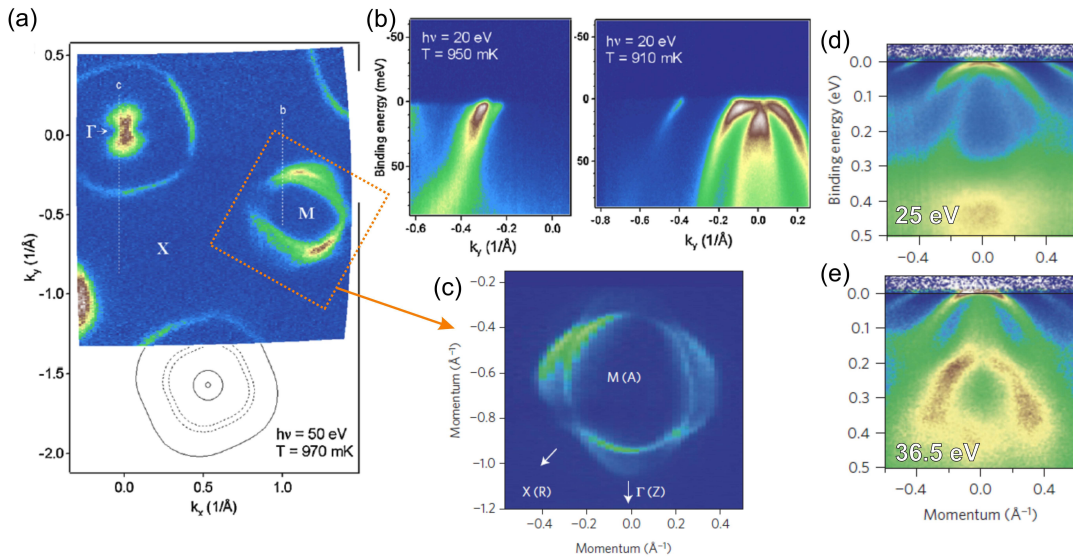
FIGURE 1.10: Electronic structure from ARPES. (a) Fermi surface map. (b) spectra measured along the cuts passing through the electron and hole pockets respectively. Directions in which the spectra were measured are shown on the map (a) with lines. (c) High-precision Fermi surface map of electron pockets. (d) and (e) spectra measured near Γ and Z points in 3D BZ respectively. (a)-(b) adapted from [14]. (c)-(e) adapted from [8].

Such an agreement between the experimental electronic structure from low-temperature ARPES measurements and the calculated one from LDA is the evidence for the nonmagnetic ground state in LiFeAs. Specifically, the Fermi surface does not show any signatures of commensurate or incommensurate ordering, such as replica, due to any kind of a reconstruction. Another observation is that the Fermi surface does not appear to be nested, meaning that none of the different pockets are of the same size or have parallel sections.

Another ARPES study revealed that the electronic structure of LiFeAs is renormalized by both electron-phonon and electron-electron interactions [15]. Coupling to phonons is seen as kinks in the shape of d_{xy} hole-like dispersion (see the yellow curve in Fig.1.11(a)). This dispersion exhibits already three kinks at binding energies, which are in agreement with the energies of three optical phonon modes: 15, 30, 44 meV, found in the calculations [114]. Also, fingerprints of phonons can be seen in the width of the momentum-distribution curves (MDC): a derivative of its energy dependence appears to be in agreement with the calculated phonon spectrum (see Fig.1.11(b)). The strength of electron-phonon interaction estimated from these ARPES results is considerably [15] higher than the calculated one [114]. This result suggests an important role of phonons in the mechanism of pairing in this material. If only electron-phonon interaction was responsible for the mentioned above renormalization (by approximately factor 3), the energy dependence of MDC width would be more step-like and would saturate at energy near 44 meV, but from Fig.1.11(c) the presence of another component is clearly seen. This component is present at all energies including the range below and above the phonon energy range and seems to be linearly dependent on energy. This component was associated with an electron-electron scattering. Also, the presence of electron-electron scattering in LiFeAs was confirmed by the transport measurements. Measurements of resistivity showed quadratic dependence on temperature at low temperatures, up to 40K [104]. Such behavior indicates strong electron-electron scattering in this material. This result not only qualitatively confirms the presence of electron-electron scattering detected in ARPES, but also is in a quantitative agreement with ARPES results. Kadowaki-Woods ratio[7] directly calculated from the results of the resistivity measurements [104] and specific heat measurements [116] is 6 times higher than the value calculated from tight-binding parameters obtained from ARPES results [14, 12]. It is still a quite good agreement.

The absence of the Fermi surface nesting is in line with the absence of the SDW order since SDW order in other iron-based superconductors is usually associated with the strong scattering between electron and hole pockets (see Ref. [117]), naturally improved by nesting. Though static magnetic order was never observed in LiFeAs, magnetic fluctuations were indeed observed.

Inelastic neutron-scattering was used for detecting the magnetic order and magnetic excitations in copper-based and iron-based superconductors

---

[7]Kadowaki-Woods ratio is a ratio of the quadratic term in the temperature dependence of the resistivity to the coefficient of the linear term in the temperature dependence of the specific heat [115].
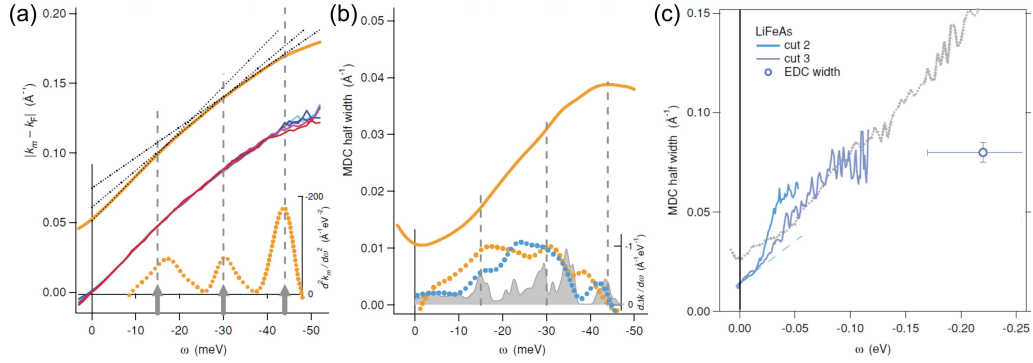
FIGURE 1.11: Shape of the dispersions from ARPES. Evidence for the
renormalization on phonons and electron-electron interaction. Adapted
from [15].

and established itself as a powerful method for this purpose. For example, a
map of neutron-scattering intensity measured on Co-doped $BaFe_2As_2$ sam-
ple (see Fig.1.12(a)) presents a clear feature at $Q = (0.5, 0.5, 0)$ which is asso-
ciated with a magnetic signal. Fig.1.12(b) shows a results of the same experi-
ment on LiFeAs. This map also displays a signal near $Q = (0.5, 0.5, 0)$, but it
is weaker and clearly split into two components in the transverse direction to
$Q_{inc} = (0.5 \pm \delta, 0.5 \mp \delta, 0)$. Such splitting has been observed in several studies
[118, 119, 120] and indicates incommensurability of the magnetic excitations.
Two interpretations were suggested to explain the origin of the magnetic sig-
nal: it can be either due to scattering between the electron pockets and inner
hole pocket [119] or between electron pockets and the outer hole pocket [121].
The study of Queshi et al. [120] shows even more interesting result: a care-
ful examination of the incommensurate signal reveals that it consists of four
components, instead of two. It can be seen from Fig.1.12(c), which shows a
distribution of intensity along transverse direction (shown with dashed line
on Fig.1.12(b)). The second pair of peaks appears as shoulders in the distribu-
tion. A fit of two pairs of Gaussian functions to this distribution gives values
of incommensurability of $\delta_1 \approx 0.07$ and $\delta_2 \approx 0.15$. Presence of two signals
can be interpreted as a presence of both earlier suggested ways of scattering:
(i) between the outer hole pocket and the inner electron pocket, (ii) between
the outer hole pocket and the outer electron pocket. The magnetic signal was
detected up to energy transfer of 60 meV and it remains incommensurate up
to at least 30 meV [120] (at higher energies it cannot be determined because
of not sufficient resolution). In the superconducting state at low energies in-
tensity of the signal is suppressed almost to the background level (see Fig.
2(a-b) in Ref. [118]), while for energies above a certain value it is enhanced
in the superconducting state. This can be seen from Fig.1.12(d), which shows

energy dependence of the INS scattering intensity at $Q_1 = (0.5 - \delta_1, 0.5 + \delta_1, 0)$ and $Q_2 = (0.5 - \delta_2, 0.5 + \delta_2, 0)$ in the normal and the superconducting state. Both pairs of curves display such behavior. For Q_1 the intensity has a broad minimum at $\sim$4.5 meV while for Q_2 such minimum is at $\sim$7 meV. The difference of these values confirms the assumption of their independent origin and indicates the presence of 2 different gaps in material, which was confirmed by other methods (see below in this section).
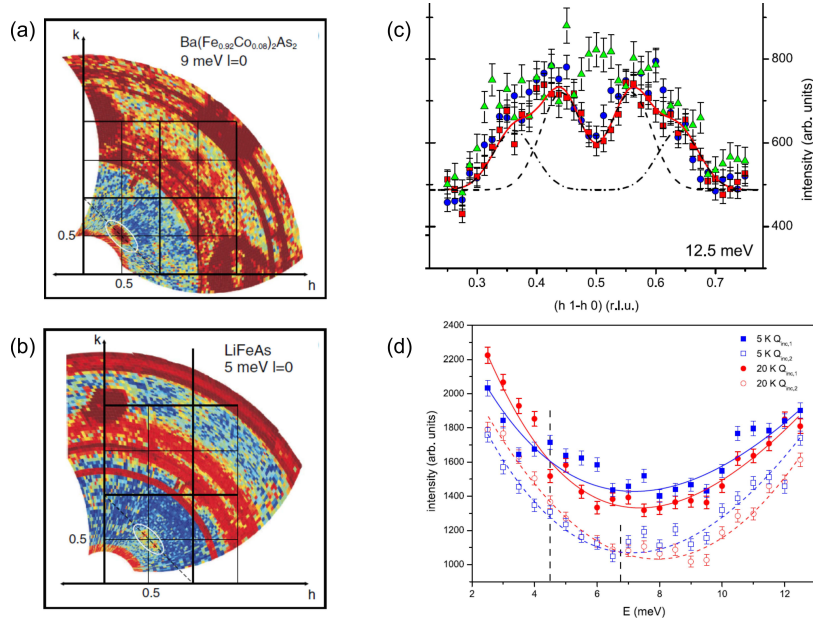
FIGURE 1.12: (a) distribution of neutron-scattering intensity measured on optimally Co doped BaFe$_2$As$_2$. (b) distribution of neutron-scattering intensity measured on LiFeAs. (c) distribution of intensity along transverse direction at 12.5 meV energy transfer. (d) energy dependence of the INS scattering intensity at Q_1 and Q_2 in the normal and the superconducting state. (a)-(b) adapted from [118]. (c)-(d) adapted from [120].

Early quasiparticle interference (QPI) study [122], which is based on tunneling spectroscopy and microscopy (STS/STM) measurements, is in contradiction to ARPES results. Similarly to ARPES, this study claims the presence of 3 hole-like dispersions in the center of the BZ, but in contrast to ARPES results all dispersions including the most central one cross the Fermi level and the middle dispersion forms a considerably larger Fermi surface. According to the interpretation of the authors (which considers only intraband scattering) this result follows from the presence of 3 circular futures in QPI patterns (Fourier transformed tunneling spectroscopic maps) (Fig.1.13(a) and (b)) and their evolution with binding energy (Fig.1.13(c)). Here h_1, h_2 and h_3 features are associated with the scattering between all three hole-like pockets. Newer QPI studies [123, 124] present similar experimental results (Fig.1.13(e)), but
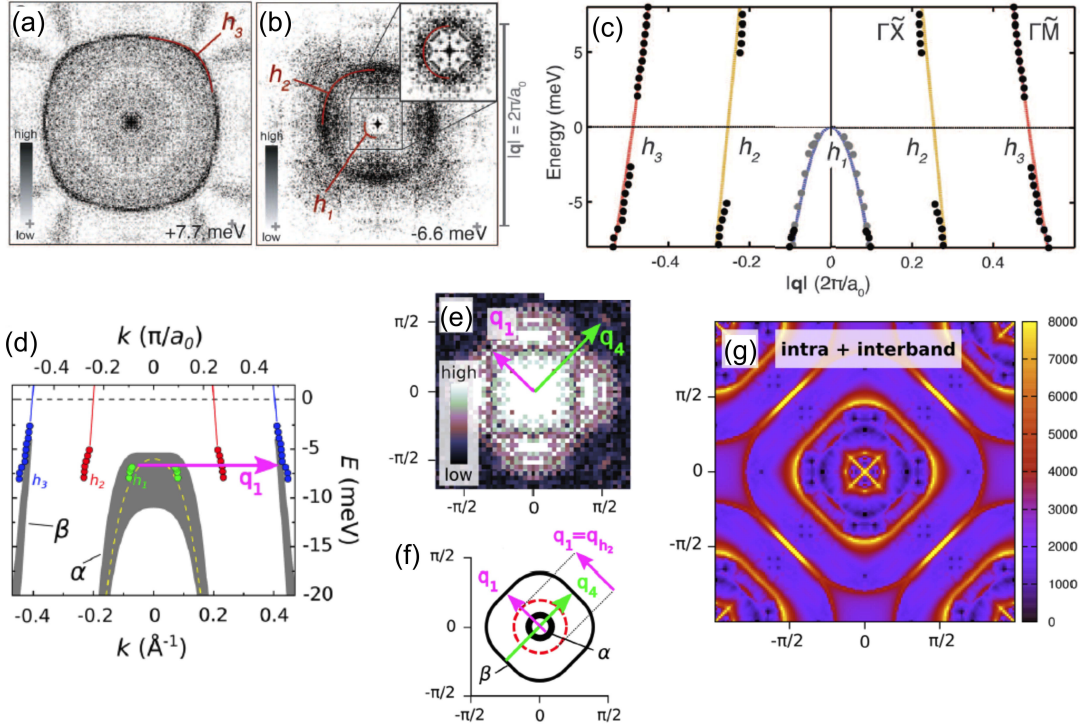
FIGURE 1.13: (a) and (b) QPI patterns for 2 different energies. (c) energy dependence of 3 QPI figures from (a) and (b). (d) comparison of band-structure from ARPES (broad dark contours) with QPI results (colored circles, the same as (c)). (e) QPI pattern from another study. (f) guide to the eye which shows the interpretation, of scattering vectors on (e). (g) numerical simulation of a QPI pattern which considers both intraband and interband scattering. In Ref. [123] one can also find patterns cases of only intraband and only interband scattering. (a)-(c) adapted from [125]. (d)-(g) adapted from [123].

they suggest another interpretation for them. This interpretation resolves ARPES-QPI paradox by including the intraband scattering. According to this interpretation, h_3 future is associated with the scattering within the outer hole-like dispersion, h_1 future is associated with scattering within the middle hole-like dispersion, h_2 future is associated with the scattering between these two dispersions (Fig.1.13(d) and (f)). A comparison of experimental QPI pattern (Fig.1.13(e)) with the corresponding numerical simulation (Fig.1.13(g)) was performed by Hess *et al.* [123]. There the tight-binding parameters have been obtained from ARPES results on LiFeAs [14, 85]. The comparison shows a good agreement between them. From this one can conclude, that QPI and ARPES results are consistent when both intraband and interband scatterings are considered.

Understanding of the mechanism of high-temperature superconductivity

in IBS requires precise knowledge of the symmetry and structure of the order parameter, i.e. the superconducting energy gap. Presence of more than one superconducting gap in LiFeAs was detected by several experimental techniques. As mentioned above, inelastic neutron-scattering experiments reveal two components of the magnetic signal, which become suppressed in slightly different ways in the superconducting state. This indicates the presence of two energy gaps with magnitudes of ∼4.5 and ∼7 meV. In STS experiment with the presence of more than one superconducting gap can be already concluded from a single spectrum (energy dependence of differential conductance) (see Fig.1.14(a)). Two big peaks at $|E| \approx 6$ meV correspond to the bigger gap and two small peaks which appear as shoulders at $|E| \approx 3$ meV correspond to the smaller gap. Near $E = 0$ the signal is absent, which indicates that LiFeAs is a fully gapped superconductor. By applying quasiparticle interference analysis to STS/STM results one can shed light on a gap distribution in the momentum space: identify to which Fermi surface pocket which gap corresponds and whether the gaps on these pockets are anisotropic. Such analysis of the STS/STM results was performed by Alan *et al.* [122]. Gap anisotropy on big hole pocket associated with h_3 QPI feature can be seen from QPI pattern (see Fig.1.14(b)) at energy of 2 meV above the Fermi level. It displays intensity in $\Gamma - M$ direction, but this intensity is absent along $\Gamma - X$ direction. This indicates that the gap in $\Gamma - M$ direction is larger than in the $\Gamma - X$ direction. Further analysis leads to the conclusion that the gap on this pocket changes in a range from 2 to 3 meV and has C4 symmetry with a minimum corresponding to $\Gamma - M$ direction (see Fig.1.14(c)). Also, this study shows that gap on small hole-like Fermi surface pocket associated with h_1 QPI feature is larger ($\sim 6\pm1.5$ meV) than on the big hole-like pocket.

ARPES is the only technique which is able to access the electronic structure directly, without any processing of raw data (such as, e.g. Fourier transformation in QPI-method). Because of this, ARPES is the most relevant technique for measuring superconducting gap anisotropy. Detailed investigations of the superconducting gap size in LiFeAs with ARPES were performed in at least two studies by Borisenko *et al.* [85] and Umezawa *et al.* [113]. Both of them revealed that: (i) all pockets of the BZ are gapped, (ii) the biggest gap is on the small hole pocket and the smallest gap is on the big hole pocket, (iii) the gap on the same pockets is anisotropic. However, there were also some differences in mentioned studies. Let's have a more detailed look at the results. Presence of the gap anisotropy on the large hole-like pocket can be seen

from Fig.1.14(e) which shows dispersions along A and B cuts (see Fig.1.14(d)) obtained by tracking energy distribution curves' (EDC) maxima. It is clear that the gap from cut B is larger than that from cut A. The result of extracting a position of a maximum of EDC at k_F as a function of direction is shown on Fig.1.14(f) (55% of the pocket was analyzed). It implies that the gap on this pocket has C4 symmetry with a maximum corresponding to $\Gamma - X$ direction and its magnitude varies around ~3.4 meV with an amplitude of ~0.4 meV [85].
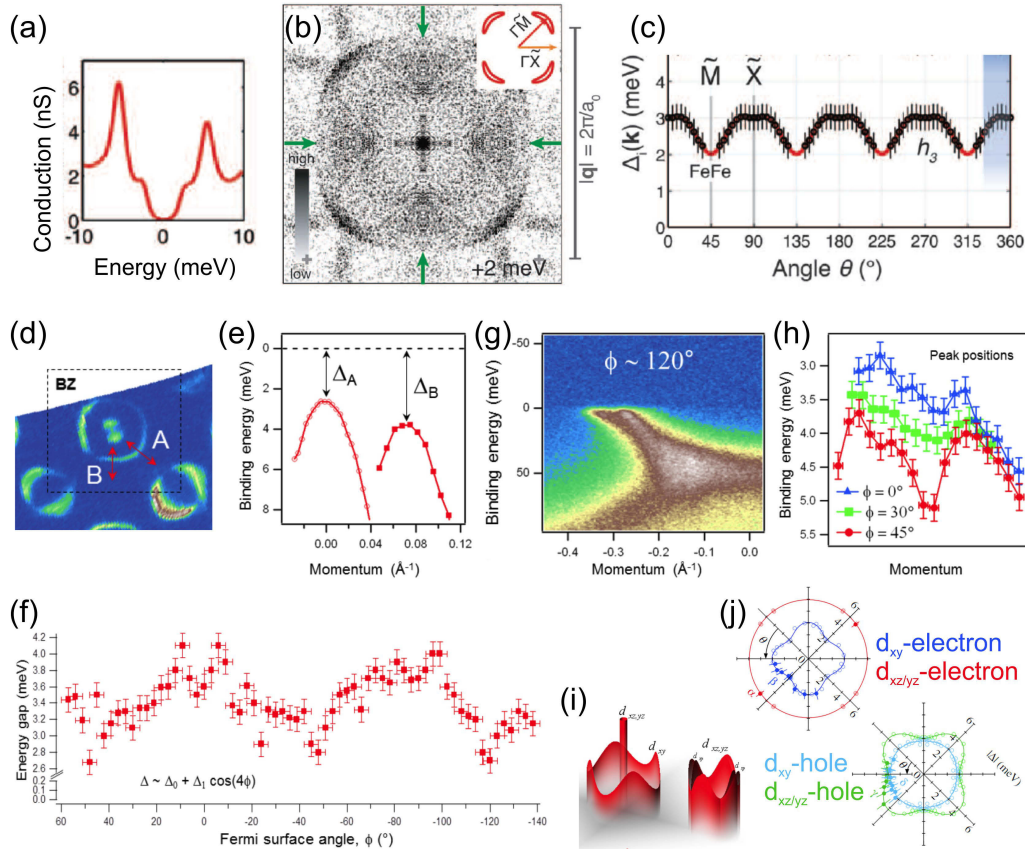
FIGURE 1.14: Superconducting gap. (a) STS spectrum averaged over the sample. (b) QPI pattern at energy 2 meV. (c) superconducting gap anisotropy on the outer (big) electron pocket from QPI. (d) Fermi surface map from ARPES. Red arrows show the location of the cuts A and B. (e) dispersions along A and B cuts obtained by tracking EDC's maxima. (f) superconducting gap anisotropy on the outer electron pocket from ARPES. (g) typical radial momentum cut through electron pockets. (h) the results of tracking EDC's maxima on 3 different cuts. (i) and (j) present the overviews of the results from [85] and [113] respectively. A shape of the contour in (i) represents the shape of the pockets and height - the gap magnitude on it. In (j) the gap magnitude is shown as a function of the angle in polar coordinate system. (a)-(c) adapted from [122]. (d)-(i) adapted from [85]. (j) adapted from [113].

The other study [113] presents quantitatively the same result, but with a

smaller average gap size of ~2.6 meV. Gaps on electron pockets are different and both are anisotropic. These can be seen from Fig.1.14(h) which shows results of tracking EDC's maxima on three different cuts (like the one shown in fig.1.14(g)) through the electron pockets. Here the right peak corresponds to the inner pocket and the left peak corresponds to the outer one. Further analysis shows the gap on the outer electron pocket having C4- symmetry with a maximum in $\Gamma - M$ direction and varying around ~3.6 meV with an amplitude ~0.5 meV as well as the gap on the inner pocket behaving in the same way, but having a slightly larger value [85]. In contrast to this result, the other study [113] did not detect any noticeable gap anisotropy on the inner electron pocket. The gap anisotropy analysis of the inner hole-like pocket was not performed because of its small size, but the average gap size on it was estimated in both studies to be of the order of 5 – 6 meV [113, 85]. The overviews of the final results from Ref.[85] and Ref.[113] are shown in Fig.1.14(i) and (j) respectively.

This section makes an impression that all details of the electronic structure of LiFeAs are known except k_z variation of the superconducting gap. However, our ARPES data measured in order to investigate the k_z dependence of the gap reveals unexpected results. The in-plane variation of the gap was different from one detected in earlier studies. Moreover, it reveals a peculiarity of the electronic structure which has not been observed before. This motivated us for additional measurements and more detailed analysis of the results.

1.3   FeSe - structurally simplest iron-based superconductor

FeSe was synthesized in 1979 [126], but superconductivity in it was discovered only in 2008 [127]. As well as LiFeAs, FeSe is a stoichiometric superconductor: it becomes superconducting without doping at temperatures below 8.5K. A crystallographic structure of this material is shown on Fig.1.15(a). It belongs to 11 family of IBS. FeSe was only one stoichiometric member of this family for a long time until discovery of superconductivity in FeS at 5K in 2015[128]. This made FeSe the simplest IBS and attracted additional attention to it. In contrast to stoichiometric LiFeAs in which superconductivity

becomes suppressed with doping and applying pressure, in FeSe, temperature of the superconducting transition can be increased by doping or applying pressure. The resistivity measurements [129, 130, 131, 6] show that if pressure is applied, critical temperature increases, reaching a maximum of $\sim$37 K at $\sim$8 GPa (see Fig.1.15(e) and (h)). By substitution Se with Te, the critical temperature can be increased up to 13.5 K, which corresponds to a doping level $x \approx 0.5$ (see a phase diagram on Fig.1.15(f)). This was shown in the resistivity measurements [132] (see Fig.1.15(c)) and susceptibility measurements [37, 133]. A similar effect can be also caused by S-doping. As it was shown with various techniques: resistivity measurements [132, 134] (see Fig.1.15(d)), susceptibility measurements [125, 135] specific heat measurements [125] critical temperature in $FeSe_{1-x}S_x$ increases with increasing of doping level and reach maximal value of $\sim$10.5 K at doping level $x \approx 0.11$. Upon further doping, critical temperature starts to decrease and at doping levels $x = 0.4 - 0.5$ zero-resistivity state has not been observed (see a phase diagram on Fig.1.15(g)).
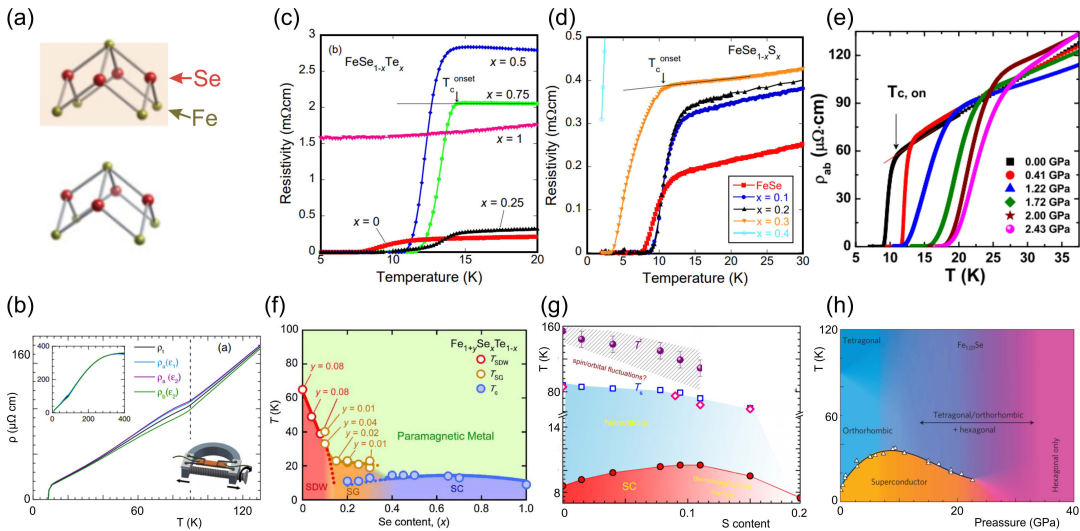
FIGURE 1.15: (a) Crystal structure of FeSe. (b) results of the transport measurements on a detwinned sample. (a) and (d) results of the transport measurements on samples doped with Te and S, respectively. (e) results of the transport measurements on samples under pressure. (f), (g) and (h) phase diagrams which represent influence of doping and applying pressure. (a) adapted from [7] (b) adapted from [136] (c) and (d) [132] (f) [37] (g) adapted from [135] (h) adapted from [129]

FeSe exhibits structural transition from tetragonal to orthorombic phase at $\sim$ 87 K. As it was mentioned before, this transition is common for parent compounds of IBS and is followed by magnetic transition. Unlike this common case, FeSe dose not exhibit transition to magnetically ordered phase.

Also, FeSe is not similar to LiFeAs in which neither magnetic nor structural transition was observed. Changes of crystal structure of FeSe with a temperature were detected by plenty of X-ray diffraction and neutron diffraction experiments [137, 138, 139, 140, 141]. Upper panel of Fig.1.16(b) shows X-ray diffraction profile measured at 20K on $Fe_{1.01}Se$ sample. The splitting of some peaks in this profile indicates an orthorhombicity of the sample. The splitting of the peak can be better seen in Fig.1.16(c), which demonstrates a zoomed in region of X-ray diffraction profile from another study. Such splitting is absent for the profile measured on $Fe_{1.03}Se$ sample which apparently does not exhibit structural transition. Also, this figure demonstrates developing of this splitting with temperature. Two main parameters which describe structural distortion leading to orthorhombicity are Fe-Fe distances (d_{Fe1} and d_{Fe2}) for two orthogonal directions (see Fig.1.16(a)). The temperature-dependence of these parameters is shown in Fig.1.16(d). It is seen from this plot, that deformation is small $D = 2(d_{Fe1} - d_{Fe2})/(d_{Fe1} + d_{Fe2}) = 0.45\%$ but it is comparable with ones in other IBS. Despite very small changes in the crystal structure this transition is accompanied by noticeable changes in properties, e.g. transport measurements on detwinned[8] sample show noticeable anisotropy in resistivity [136] (see Fig.1.15(b)).

Magnetic ordering is not observed in FeSe down to 5K. Mössbauer effect measurements do not display significant changes in a spectrum shape with temperature in a range from 5 to 295 K. [140, 142, 129]. All Mössbauer spectra (see Fig.1.17(a,b)) exhibit a single quadrupole paramagnetic doublet without an additional splitting into a sextet which is expected for an ordered magnetic phase. For comparison in Fig.1.17(c), we show Mössbauer spectra of LaOFeAs which demonstrate such sextet in the ordered magnetic phase [143].

Nuclear magnetic resonance measurements show that orbital-driven nematic scenario is prefereble in FeSe. [59, 144]. Both studies show a temperature dependencies of spin–lattice relaxation rate $(T_1)^{-1}$ which dose not display enhancement of magnetic fluctuations at temperature of structural transition (see Fig.1.17(d)). Considerable increase of $(T_1T)^{-1}$ which indictes enhancement of magnetic fluctuations occurs only at lower temperatures. This indicates, that spin-driven nematic scenario is unlikely, because this orbital-driven scenario was considered as the most feasible scenario in FeSe. In contrast to NMR measurements, inelastic neutron scattering measurements on a

---

[8]It means that almost all domains are oriented in one direction. This can be reached by applying strain to the sample
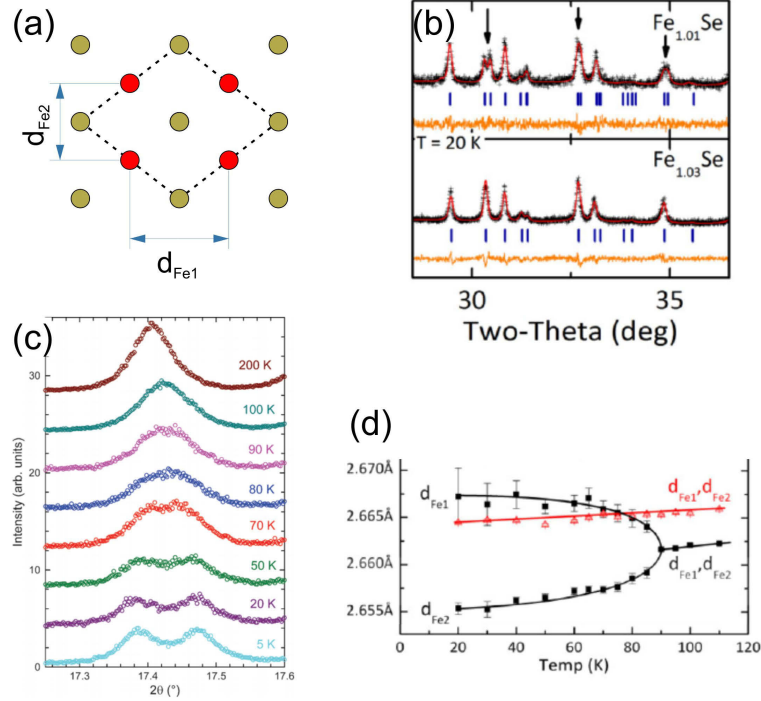
FIGURE 1.16: (b) X-ray powder diffraction profiles measured on $Fe_{1}.01Se$ and $Fe_{1.03}Se$. (c) temperature evolution of one of the diffraction peaks. (d) temperature evolution of the lattice parameters extracted from X-ray powder diffraction results. (b) and (d) adapted from [140]. (c) adapted from [138].

single crystal found evidences for spin-driven scenario [145]. The commensurate scattering signal which are associated with magnetic excitations has been detected. This persists becomes enhanced in the nematic phase on a whole measured range of energies (see Fig.1.17(e)). The temperature dependence of the scattering at 2.5 meV (Fig.1.17(f)) has onset at temperature of structural transition an behaves similar to orthorhombic deformation. This indicates that the nematic order is originated from spin fluctuations. The contradiction between neutron scattering and NMR results can be explained by the fact that the latter probes only momentum integrated spin fluctuations at very low energies. However, NMR is not only the one technique, which shows results dissonant with spin-driven scenario, the results of thermal-expansion measurements also contradict it [146].

An investigation of influence of nematicity on the electronic structure of the material can help to shed light on its origin. Fig.1.18(a) shows a calculated band structure of FeSe which is simular to calculated electronic structures of other IBSs. It has 3 hole-like dispersions γ formed by d_{xy}, α formed by d_{xz}, and β formed by d_{yz} orbitals of Fe which cross the Fermi level near Γ point which is the center of the BZ. Two electron-like dispersions δ are formed by
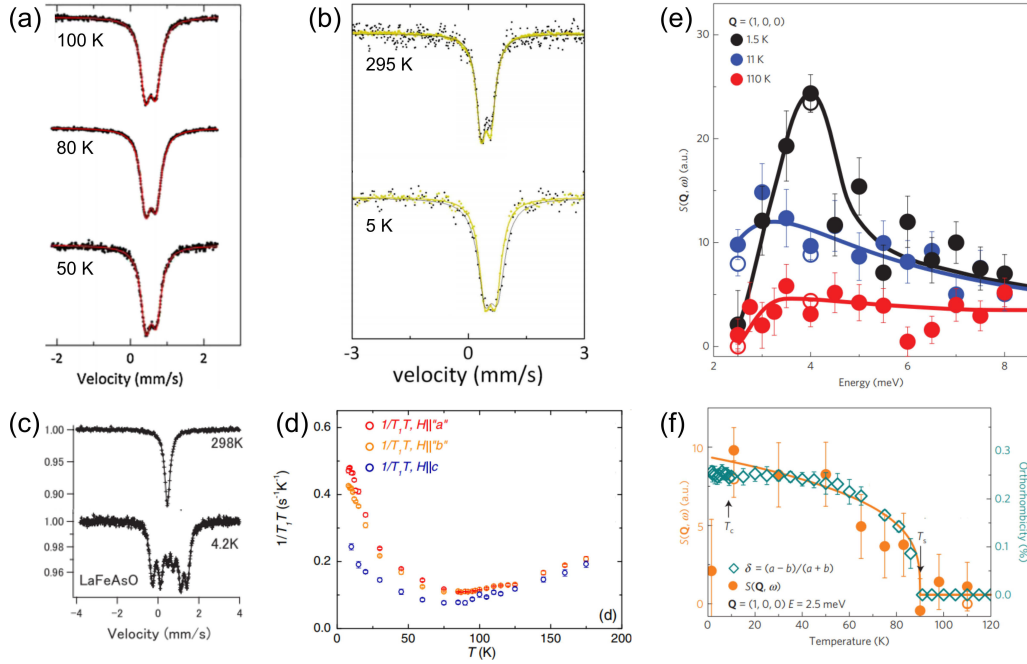
FIGURE 1.17: (a) and (b) Mössbauer spectra of FeSe at several temperatures. (c) Mössbauer spectra of LaFeAsO. (d) temperature dependence $(T_1 T)^{-1}$ for a different direction of the applied field. (e) Energy dependence of the dynamic spin correlation function at Q=(1,0,0) measured at different temperatures. (f) temperature dependence of spin correlation function at energy 2.5 meV and the orthorhombic deformation. (a) adapted from [140]. (b) adapted from [142]. (c) adapted from [143]. (d) adapted from [144]. (e) and (f) adapted from [145]

d_{xy}, and ε formed by d_{yz} orbitals of Fe, which cross the Fermi level near M point – the corner of the BZ.[9]. Such electronic structures corresponds to Fermi surface with 3 big concentric pockets in the center of the BZ and two pockets in its corner. ARPES measurements on FeSe were performed by several groups [13, 55, 56, 57, 58, 147, 16, 148, 149]. Fig.1.18(b) shows the first experimental Fermi surface map of FeSe. It has a pocket (pockets) in the center and pocket (pockets) in the corner of the BZ, as it is predicted by calculations. However, they are considerably smaller which is a hallmark of the "red-blue" shift. Newer studies [58, 148, 149] succeeded in resolving details of these structures in the center and corner of the BZ Fig.1.18(c, d) respectively. The structure in the center and corner of the BZ Fig.1.18(c) consists of two crossed ellipses which are oriented orthogonal to each other. From Fig.1.18(e), which shows the spectrum measured through the pocket center in a vertical direction, and Fig.1.18(f), which shows results of its fitting, it is seen, that only dispersion formed by α crosses the Fermi level, other two dispersions being

---

[9]For a direction orthogonal to this one dispersions change there orbital character from d_{yz} to d_{xz} and vice versa.

bellow it. It is clear, that this dispersion is split to two dispersions, which correspond to two ellipses. This can be the explained by presence of domains with two different orientations in the sample in the orthorhombic phase. In ARPES, a size of a probed area of the sample, which is determined by the beam spot size, is bigger than typical domain size. As a result, one detects a photoemission signal, which is a superposition of signals from different domains. Another peculiarity of FeSe, which is seen in Fig.1.18(e,f), is a strong renormalization of γ hole-like dispersion. It is renormalized by a factor of $5-9$ [13, 16] which is larger than for other dispersions in FeSe as well as for this dispersion in other IBS. As it is seen from Fig.1.18(d), the structure in the corner of the BZ also consists of two crossed pockets, which are formed by two electron-like dispersions (see Fig.1.18(g, h)). There is no consensus on the interpretation of this result. A popular interpretation is that these two pockets are a superposition of single electron pockets from two different domains. as well as it for the hole pockets. In this interpretation two electron-like dispersions, which are seen in Fig.1.18(g, h) are split by 50 meV. ε dispersions originated from domains with different orientations and δ dispersions are not observed. This interpretation is supported by the fact, that these two dispersions cannot be resolved in tetragonal phase [55, 56, 57, 58]. On another hand, inability to resolve them can be caused by temperature blurring, since the measurements should be carried at temperature higher than 90 K, which correspond to tetragonal phase. This fact together with mystical disappearance of δ dispersions and huge splitting of 50 meV which is bigger then a scale of nematic splitting (10 meV) estimated in Ref.[8], makes this interpritation inconsistent. So, more studies are needed.

There are plenty experimental studies of the superconducting gap in pristine FeSe and its Te- and S-doped siblings using different techniques: STS [150, 151, 152, 153, 154, 155, 156], ARPES [149, 157, 158], specific heat [159, 160, 125, 161, 150] and London penetration depth [153, 125]. Nevertheless, there is no consensus on the size and symmetry of the gap in the full BZ. The majority of STS experiments detect the presence of more than one superconducting gap in FeSe. Fig.1.19(a) shows STS spectrum (dI/dV) in which one can see two pairs of coherence peaks. One pair at ± 2.3 meV appears as real peaks and another pair at ± 1.5 meV appears as shoulders on the spectrum (see arrows on Fig.1.19(a). This spectrum features almost V-shape gap with a small (± 0.15 meV) flat part near zero-voltage (Fermi level), which indicates that superconducting gaps (either both or only one of them) are highly anisotropic but without nodes. The smallest gap is ~ 0.15 meV. There is also
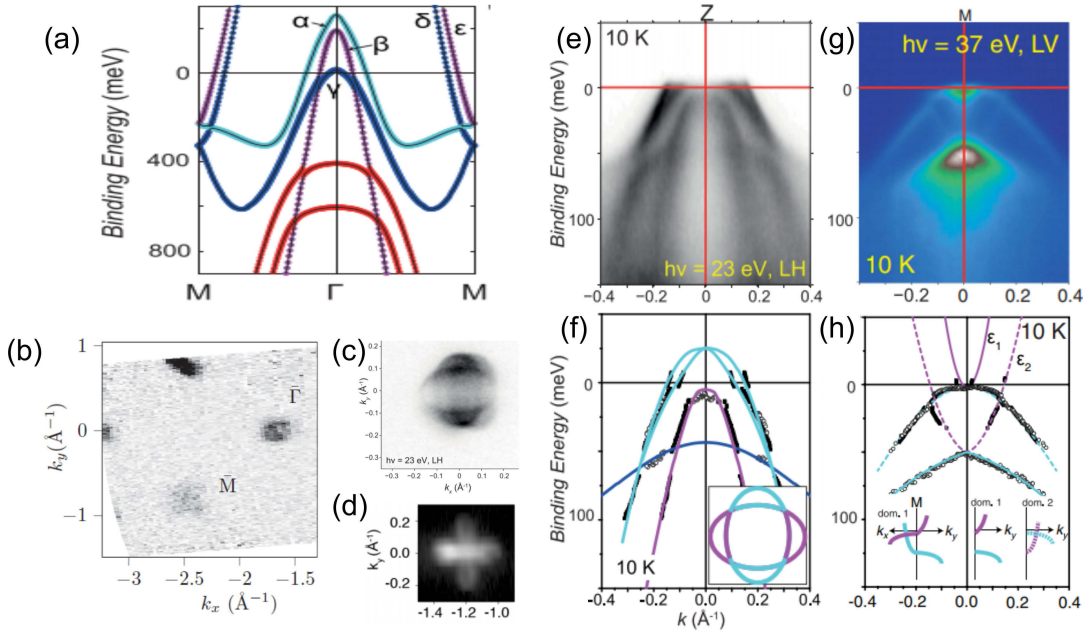
FIGURE 1.18: (a) electronic structure calculations for FeSe in the tetragonal phase. Here green dashed line shows real Fermi level position obtained from ARPES. (b), (c), (d) overview Fermi surface map and detailed Fermi surface maps of the center and the corner of the BZ respectively obtained by ARPES. (e) and (g) ARPES spectra measured through the center of the hole pocket the center of the electron pocket respectively. (f) and (h) dispersion from MDC and EDC fitting spectra in (e) and (g) Here coloured lines shows an interpretation of these results according to Ref.[58].
(a), (c), (e)-(h) adapted from [58]. (b) adapted from [13]. (d) adapted from [148]

another pair of shoulders at ± 3.5 meV. In some studies, it is associated with a possible another superconducting gap [153], but most likely it is caused by the electronic density of states redistribution associated with the boson mode in strongly coupled superconductors [162, 152]. The next step is measuring superconducting gap anisotropy, which can be done with ARPES or QPI. A resent QPI study (Ref.[151]) claims anisotropic gap on both pockets. Gap on the hole pocket in the center of the BZ has C2 symmetry with maximal magnitude 2.3 meV on a short axis of the pocket (see Fig.1.19(b)). Gap on the electron pocket in the corner of the BZ is smaller. It has C2 symmetry with maximal magnitude 1.6 meV on a short axis of the pocket (see Fig.1.19(c)).

As mentioned before, ARPES remains the only method of direct determination of the gap as a function of momentum. Nevertheless, there is no consensus even in ARPES results. For instance, one study (Ref.[158]) reported an isotropic gap with the magnitude of 2.5 meV on the electron pocket in $FeSe_{0.45}Te_{0.55}$, while another study reported smaller and considerably anisotropic

gaps in the very similar sample FeSe$_{0.4}$Te$_{0.6}$[10] (Ref.[157]). As for the pristine FeSe, there is only one ARPES study on a slightly S-doped FeSe. In this study, anisotropic gap was detected on the hole pocket near Z point, while no gap has been observed on the electron pockets. As one can see, this result is not in agreement with STS results which indicate more than one gap. Presence of 2 gaps also follows from the specific heat and London penetration depth measurements [125, 150, 161, 159]. Also, there are no studies, which are able to shed light on a possible k_z dependence of the gap Therefore, it is important to determine the behavior of the gap function in all parts of three-dimensional BZ precisely. Preferably, it should be done by the same technique.
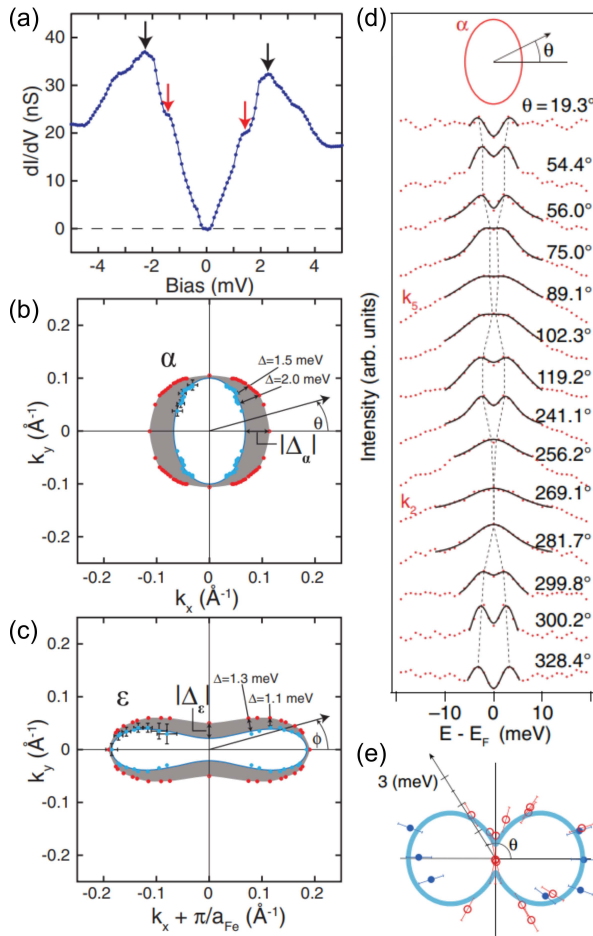
FIGURE 1.19: (a) STS spectrum (dI/dV). (b) and (c) superconducting gap anisotropy on the hole and electron pockets respectively obtained by QPI. Here shape of a contour represents shape of a corresponding pocket and a contour thickness represents the gap size on it. (d) symmetrized EDCs taken from different parts of the hole hole pocket (see inset at the top of the plot). (e) polar plot which represents superconducting gap anisotropy on the hole pocket obtained by fitting curves from (e) (a)-(c) adapted from [151]. (d)-(e) adapted from [149]

---

[10]Both samples are nearly optimal doped. There are no peculiarities near this doping level near this doping level on the phase diagram (see Fig.1.15(f)). So, no quality differences in the gap structure are expected.

Chapter 2

Angle-Resolved Photoemission

2.1 Introduction

Angle-resolved photoemission spectroscopy (ARPES) is a technique based on the photoelectric effect, which is an emission of electrons from matter exposed to the light. This effect was first observed by Heinrich Hertz in 1887 [163] and was not explained until 1905, when Albert Einstein developed a theory based on a quantum nature of light [164]. In this explanation a photon (single corpuscle of light) is absorbed, its energy transfers to electron and if absorbed energy is sufficient, the electron can be emitted from the matter. Energy and angle of emission of this electron are unambiguously connected to its initial state. This fact underlies photoemission spectroscopy. The main formula of photoelectric effect is

$$E_B = h\nu - \Phi - E_{kin} \tag{2.1}$$

As it can be seen from this formula, photoemission can occur only if photon energy ($h\nu$) is higher than the work function (Φ) of the material which is usually of the order of 5 eV. Light sources which can be used for ARPES experiment will be discussed later. From the momentum conservation law one can obtain an in-plane (parallel to the sample surface) component of the momentum of the electron in its initial state. Here one can neglect momentum of the photon. This can be done because for photon energies of 15-120 eV (which are usually used for ARPES) its momentum varies from small fraction of a percent to several percents of a typical size of the BZ. So, we can assume that in-plane component of the momentum of the electron in the initial state inside the sample is equal to the one of the photoelectron in the final state outside the sample: $\hbar k_{i\parallel} = p_{i\parallel} = p_{f\parallel}$. A component perpendicular to the sample surface is not conserved, due to the lack of translational symmetry along this direction.

Principal scheme of photoemission spectroscopy experiment is shown in Fig.2.1(a). A sample is shone by monochromatic ultraviolet or X-ray beam which causes the photoemission. Emitted electrons can be collected and characterized by an electron energy analyzer. Photoelectrons can be characterized by the kinetic energy E_{kin} and the direction of emission. This knowledge allows one to calculate absolute value of momentum of the photoelectron in a final state outside the sample $p_f = \sqrt{2mE_{kin}}$ as well as all of its components. From energy conservation law one can obtain binding energy of the electron in its initial state in the sample before photoemission took place.

2.2   Theory of photoemission

Phenomenologically, photoemission process can be described using so-called "three-step model" in which it is divided into to 3 independent steps: (i) optical excitation of the electron in the solid, (ii) travel of the excited electron to the interface between the solid and vacuum, (iii) transmission of the electron into vacuum. [165, 166]

In the second step, the excited electron can interact with the solid and can be inelastically scattered when it travels toward the interface. The probability that the electron will not be scattered on its way is proportional to $e^{-\frac{d}{\lambda cos(\gamma)}}$, where λ is the mean free path, d is the depth and γ is the angle between the direction of the electron propagation inside the solid and normal to the interface. It is generally believed that a mean free path does not strongly depend on a material and is less than 1 nm for typical energies (15 – 120 eV) used in for ARPES experiment, which is only 1 – 2 lattice constants [167]. However, ARPES results from some materials disprove this. If ARPES is sensitive only to ~1 upper layer, no electronic structure along a component of momentum perpendicular to the sample surface (k_z) can be resolved. This follows from the uncertainty principle [168]. Nevertheless, many ARPES studies e.g. Ref.[8] show that k_z-variation of the band structure[1] can be clearly resolved. From these results, one can ruffly estimate the mean free path as ~10 lattice constants. Also, ARPES results for materials, surface states of which are considerably different from their bulk states (e.g. topological insulators), exhibit both bulk and surface states and signal from the bulk is at least as intense as

---

[1]For measuring k_z-dependence one should vary the photon energy.

one from the surface. Anyway, only electrons from a finite depth can reach the surface unscattered, potentially escape the solid and be detected. [2]

Now let us consider the first step of the model mentioned above. Probability for an optical excitation of N-electron system from the initial state Ψ_i^N with energy E_i^N to the final state Ψ_f^N with energy E_F^N can be described with Fermi's golden rule:

$$w = \frac{2\pi}{\hbar}|\langle\Psi_f^N|H_{int}|\Psi_i^N\rangle|^2\delta(E_f^N - E_i^N - h\nu) \tag{2.2}$$

Here delta-function is responsible for energy conservation during excitation process. H_{int} is a photoemission perturbation operator which describes the interaction between the electrons in the solid with electromagnetic field.

$$H_{int} = -\frac{e}{2m_e c}(\mathbf{A}\cdot\mathbf{p} + \mathbf{p}\cdot\mathbf{A}) + \frac{e}{2m_e c}\mathbf{A}^2 \tag{2.3}$$

where $\mathbf{A}$ is the electromagnetic vector potential and $\mathbf{p} = -i\hbar\nabla$ is the electronic momentum operator. The quadratic term in $\mathbf{A}$ is relevant only for extremely high intensities, which are not typical for ARPES experiment. So, it can be neglected. [169] If $\mathbf{A}$ constant over atomic dimensions (dipole approximation) $\mathbf{p}\cdot\mathbf{A}$ can be, also, neglected since $\nabla\cdot\mathbf{A} = 0$.[3][169] Taking into account these approaches perturbation operator can be rewritten in a following form:

$$H_{int} = \frac{i\hbar e}{2m_e c}(\mathbf{A}\cdot\nabla) \tag{2.4}$$

In an approach of sudden approximation, the photoemission process of excitation and transferring the electron to the surface is assumed to be instantaneous, without interaction between the photoelectron and the excited system left behind. It was shown in Ref.[170] that this approach can be applied for electrons with energies above 20 eV which are typical for ARPES. In a framework of sudden approximation, the wave function of the system in a final state can be factorized into wave function of photoelectron and of (N-1)-electron system.

$$\Psi_f^N = \mathcal{A}\phi_f^{\mathbf{k}}\Psi_m^{N-1}$$

Where Ψ_m^{N-1} one of possible excited states of (N-1)-electron system left behind. E_m^{N-1} is the energy of this state. $\mathcal{A}$ is an antisymmetric operator which

---

[2]The electrons which were scattered, also can be able to escape the solid, but they do not contain information about initial state of the electron anymore and just form a secondary electron background in a photoemission signal.

[3]The dipole approximation can be used for bulk, but near the surface $\nabla\cdot\mathbf{A}$ might become important.

antisymmetrizes in order to satisfy Pauli principle. In a framework of Hartree-Fock formalism the wave function of the system in an initial state can be also factorized.

$$\Psi_i^N = \mathcal{A}\phi_i^{\mathbf{k}}\Psi_i^{N-1} = \mathcal{A}\phi_i^{\mathbf{k}}c_{\mathbf{k}}^{-}\Psi_i^N$$

Here $c_{\mathbf{k}}^{-}$ is the annihilation operator for an electron with momentum $\mathbf{k}$.

Now we can write Eq.2.2 in a following form:

$$w = \frac{2\pi}{\hbar}|\langle\Psi_f^{\mathbf{k}}|H_{int}|\Psi_i^{\mathbf{k}}\rangle|^2 \sum_m |\langle\Psi_m^{N-1}|c_{\mathbf{k}}^{-}|\Psi_i^N\rangle|^2\delta(\omega + E_m^{N-1} - E_i^N) \qquad (2.5)$$

Were $\omega = -E_{bind}$ is the energy of the photohole with respect to the Fermi level. Here we summarize over all possible m final excited states of (N-1)-electron system. The photoemission signal is proportional to a sum over all possible transitions.

$$I(E_{kin},\mathbf{k}) \propto \sum_{f,i} |M_{f,i}|^2 \sum_m |\langle\Psi_m^{N-1}|c_{\mathbf{k}}^{-}|\Psi_i^N\rangle|^2\delta(\omega + E_m^{N-1} - E_i^N) \qquad (2.6)$$

Here $M_{f,i} = \langle\Psi_f^{\mathbf{k}}|H_{int}|\Psi_i^{\mathbf{k}}\rangle$ is the one-electron dipole matrix element. It depends on properties of light (photon energy, polarization) shone on a crystal and experimental geometry (orientation of the crystal with respect to the beam). $A(\mathbf{k},\omega) = \sum_m |\langle\Psi_m^{N-1}|c_{\mathbf{k}}^{-}|\Psi_i^N\rangle|^2\delta(\omega + E_m^{N-1} - E_i^N)$ is a one particle spectral function which describes a chance to remove an electron with energy ω and momentum $\mathbf{k}$ from a system which can be treated as probability to find an electron with ω and $\mathbf{k}$. Finally, photoemission intensity can be written as

$$I(\omega,\mathbf{k}) \propto \sum_{f,i} |M_{f,i}|^2 A(\mathbf{k},\omega)f(\omega) \qquad (2.7)$$

Here the fact that electron can be removed only from the occupied electronic states is accounted by adding a Fermi–Dirac function $f(\omega) = 1/(exp(\frac{\omega}{kT}) - 1)$. Where k is Boltzmann constant and T is temperature. As can be seen from Eq.2.7 using ARPES one is able to measure the spectral function directly. Actually, some parts of it can be partially or completely suppressed by matrix elements. Nevertheless, these parts can be measured with different photon energy and/or in a different experimental geometry. By measuring the spectral function one can have an access to the interactions within the system.
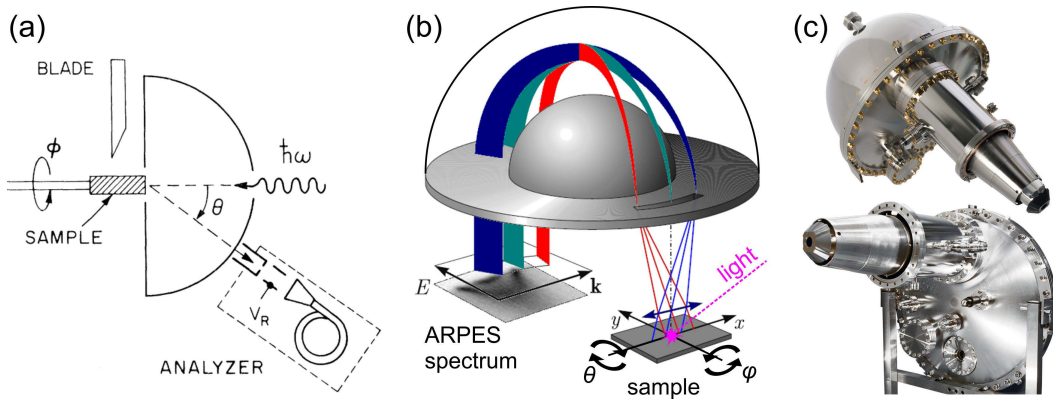
FIGURE 2.1: (a) Schematic diagram of the first angle-resolved photoemission spectroscopy setup. (b) Schematic diagram of a modern ARPES setup with a hemispherical electron analyzer. (c) pictures of a modern commercial hemispherical electron analyzer: *Scienta DA30*. (a) adapted from [171], (b) created by V. Zabolotnyy, modified by A. Kordyuk and Y. Kushnirenko, (c) adapted from [173]

2.3 Electron analyzer

In early ARPES experiments [171] electron energy analyzers able to collect electrons emitted only in one detection at the same time were usually used. For measuring the signal at other angles the analyzer should have been shifted or the sample should have been rotated, or both. These movements have been implemented e.g. in the setup of Smith and Traum [171] (see Fig.2.1(a)). In modern ARPES experiments, hemispherical angle-multiplexing analyzers are widely used. The first one was launched by *VG Scienta* in 1989 [172]. A schematic representation of this hemispherical analyzer is shown in Fig.2.1(b). Such analyzer is able to collect electrons emitted in one plane in a wide range of angles (up to tens of degrees) and characterize them not only by E_{kin} but also by angle of emission.

Let's consider the hemispherical electron energy analyzer in more details. It consists of an electron lens, a hemispherical capacitor, and a detector. The electron lens projects photoelectrons emitted from the sample, which should be placed in its viewpoint, onto the entrance slit of the hemispherical capacitor. With this, electrons emitted in the same direction from different parts of the sample are focused to the same point on the entrance slit and this point is different for different directions of emission. Inside the hemispherical capacitor these electrons are split up according to their kinetic energy because radius of curvature of their trajectories depends on energy. As a result, they land on the detector separated along the direction, perpendicular to the slit

(marked as "E" on the schematic diagram in Fig.2.1(b)). Actually, only electrons within a small range of kinetic energies can pass the capacitor. Central energy of this range is called "pass energy" and it depends on the voltage applied between hemispheres. The electron analyzer is designed in a way that it has only discrete set of pass energies (the sets for *Scienta R4000* and *Scienta DA30* analyzers are listed in Table 2.1). So, for analyzing the photoelectrons with kinetic energies around particular value they should be decelerated (or in some rare cases accelerated) to one of the preset pass energies. This deceleration is achieved by changing voltages on the elements of the lens Distribution of the electrons along another axis of the detector (marked as "k" in the schematic diagram) replicates the distribution on the entrance slit and, as a consequence, corresponds to different angles of emission.

The detector consists of two electron multipliers, the so called multi-channel plates (MCP), and a phosphorous screen. If photoelectron riches a certain place of the detector, it is multiplied in a certain channel of MCP and causes a light pulse in a certain place of the phosphorous screen. These light pulses are then captured by a CCD camera and the signal is transferred to the computer. A field-terminating mesh placed in front of the MCP terminates the field of the analyzer and repels low energy secondary electrons by the negative bias voltage on it. Despite the mesh is a standard component of the analyzer, a modification of a model *R4000* from *VG Scienta* without a mesh is used in ARPES setup at Beamline I05 of *Diamond Light Sourceentrance*, thus no imprint of the mesh structure is visible on the detector image. [174] Usually, one can get rid of this imprint performing the measurements in a swept mode (read below), which is more time-consuming and can influence both energy and angular resolution. On the other side, in such configuration, a fixed mode can be used. Other specifications of *Scienta R4000* analyzer can be found in Table 2.1.

To summarize this part, a hemispherical electron analyzer provides a 2-dimensional spectrum which represents a distribution of photoelectrons emitted in a plane formed by the analyzer slit and "optical axis" of the lens by kinetic energy and angle of emission within this plane. As follows from discussed above relation of angle with momentum and conservation laws, this distribution can be converted into distribution of electrons in the initial state as a function of binding energy and one of two in-plane components of the momentum (let us call it k_x-component since it is parallel to x axis of the sample in Fig.2.1(b)). The value of another in-plane component of the momentum

(k_y component) remains constant [4].

Characteristic	Value
Acceptance angle	$\pm$15 degrees
Angular resolution	<0.1 degrees
Energy resolution	<1 meV
Pass energies	1, 2, 5, 10, 20, 50 and 100 eV
Minimal entrance slit	100 μm
Resolving power ($E_{kin}/\Delta E$)	4000

TABLE 2.1: Technical specs of *R4000* hemispherical electron analyzer from *VG Scienta*

2.4 Manipulator

Since the analyzer is able to analyze the electrons emitted only in one plane and only in an angular range limited by the acceptance angle, in order to analyze electrons emitted in other directions, one should shift the analyzer or rotate the sample. The latter can be easily realized. In order to do this, the sample-holder with the sample should be mounted on a manipulator with transitional and rotational degrees of freedom. The transitional degrees of freedom are used for placing the sample exactly to the viewpoint of the analyzer. The rotational ones are used for scanning different directions of emission. We call the rotation around y axis of the sample (angle φ) tilting. This rotation does not change the plane but shits the analyzed range of angles and, as a consequence, the k_x range. We call the rotation around x axis (angle θ) polar shift. This degree of freedom is the most useful one, it allows one to do scans for different values of k_y component. If large number of such (E_B, k_x) spectra for different values k_y is measured, these spectra can be stacked together forming a so-called map which is a distribution of electrons by E_B and both in-plane components of momentum (k_x,k_y). Such set measured with high-energy photons ($h\nu \gtrsim 80eV$) and using the analyzer with the wide acceptance angle ($\gtrsim 30$ degrees) can even cover more than one BZ. If measurements should be performed with low-energy photons one can also measure the whole BZ, but for this the sample the tilting should also be involved. That was a qualitative explanation of scanning the momentum space with aid of a manipulator. If a real experiment is performed, one should know to

---

[4]Actually, the value of this component is not always the same across the full detector (see Eq.2.10).

which values of k_x and k_y does the signal detected by the analyzer at angle α correspond, when the analyzer is in a certain position.

A direction of emission can be written in terms of direction cosines $(e_x, e_y, e_z)^T$: cosines of the angles between the vector of direction and the coordinate axes. If the sample is orthogonal to direction of the analyzer ($\theta = 0$, $\varphi = 0$) a signal detected by the analyzer at angle α corresponds to the following direction of emission:

$$\begin{pmatrix} e_{x0} \\ e_{y0} \\ e_{z0} \end{pmatrix} = \begin{pmatrix} sin(\alpha) \\ 0 \\ cos(\alpha) \end{pmatrix} \tag{2.8}$$

If the sample is rotated around axis x ($\theta \neq 0$), the vector of direction should be multiplied by the rotation matrix for x axis. After that, if the sample is rotated around axis y ($\varphi \neq 0$), this product should be multiplied by the rotation matrix for y-axis. Here it should be mentioned that the order of applying of rotation matrices is substantial and is determined by manipulator construction. Present order corresponds to a common configuration in which the axis of tilting changes its orientation together with the sample when polar angle is changed. After changing the tilt and polar angles, the signal detected by the analyzer at angle α corresponds to the following direction of emission:

$$\begin{pmatrix} e_x \\ e_y \\ e_z \end{pmatrix} = \begin{pmatrix} cos(\varphi) & 0 & sin(\varphi) \\ 0 & 1 & 0 \\ -sin(\varphi) & 0 & cos(\varphi) \end{pmatrix} \begin{pmatrix} 1 & 0 & 0 \\ 0 & cos(\theta) & sin(\theta) \\ 0 & -sin(\theta) & cos(\theta) \end{pmatrix} \begin{pmatrix} e_{x0} \\ e_{y0} \\ e_{z0} \end{pmatrix} =$$

$$= \begin{pmatrix} sin(\varphi)cos(\alpha)cos(\theta) + cos(\varphi)sin(\alpha) \\ sin(\theta)cos(\alpha) \\ cos(\varphi)cos(\alpha)cos(\theta) - sin(\varphi)sin(\alpha) \end{pmatrix} \tag{2.9}$$

This direction corresponds to following values of in plane components of momentum.

$$k_x = \frac{p}{\hbar}e_x = \frac{\sqrt{2mE_{kin}}}{\hbar}\left(sin(\alpha + \varphi) - \left(1 - cos(\theta)\right)sin(\varphi)cos(\alpha)\right)$$

$$k_y = \frac{p}{\hbar}e_y = \frac{\sqrt{2mE_{kin}}}{\hbar}sin(\theta)cos(\alpha) \tag{2.10}$$

It is clear that all directions of emission can be mapped by changing polar and tilt angles. Nevertheless, it can be useful to have one more rotational degree of freedom - azimuthal angle, which is rotation around z axis of the sample. It is needed when a spectrum in a specific direction in the reciprocal
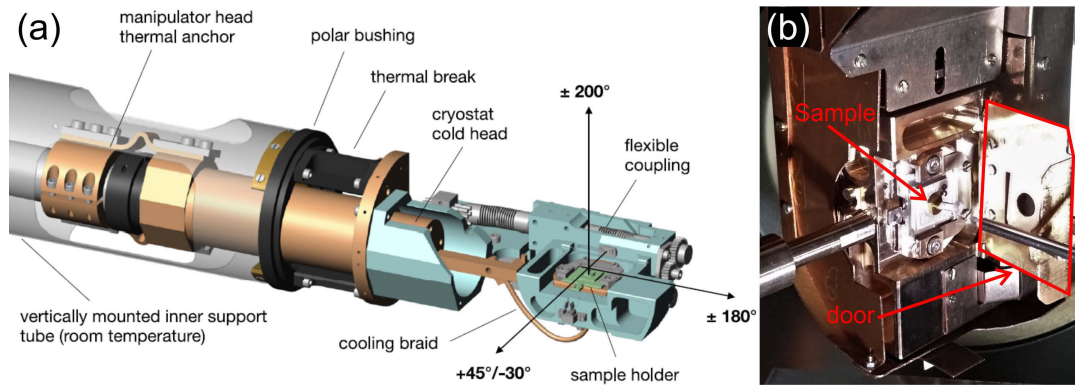
FIGURE 2.2: (a) Rendering of the cryogenic sample manipulator head. (b) Photo of the manipulator head with an uncleaved sample inside it. Here the door is not closed. (a) adapted from [174]

space should be measured. Surely, the spectrum can be interpolated from a map as well, but it is indeed better to have an opportunity to measure it directly, it is less time-consuming, more precise and convenient. Also, some parts of its electronic structure can be invisible because of matrix elements at particular orientations of the crystal with respect to the beam, determined by light polarization and geometry of the experiment. Changing azimuth can solve this problem.

Fig.2.2 shows a rendering of the cryogenic sample manipulator head used in ARPES setup at Beamline I05 of *Diamond Light Source*. It has all 3 rotational degrees of freedom together with 3 transitional degrees of freedom. Three translations are provided by a bellow-sealed xyz-stage. Polar rotation is provided by a deferentially pumped rotary seal. A tilt and azimuthal rotation are provided by a system of spur gears and worm shafts/helical wheels connected with backlash-free Inconel flexible couplings to rotary feedthroughs. [174]

2.5 Swept mode

The width of kinetic energy window of the detector is $\sim 8.4\%$ of the pass energy. In order to measure spectra with considerably wider energy range, the so-called swept mode can be used. In this mode deceleration voltage of the lens is scanned step-wise in a range. The scan is performed in a way that the desired energy range moves over the entire detector. The results of each step are automatically summed up by software. Besides the opportunity to measure wide energy ranges the swept mode has another benefit. It reduces the influence of the defects of the MCP by averaging over all energy channels.

2.6   Measurement conditions and sample preparation

As mentioned earlier, ARPES is sensitive only to a limited number of upper layers. Because of this limitation, the experiment should be performed in ultra-high vacuum (UHV) in order to prevent surface degradation. A typical pressure in the measurement chamber is less than 1×10^{-10} mbar. In order to prepare a clean surface, the sample should be cleaved in UHV shortly before the measurements[5]. In order to achieve this, the sample should be glued between the sample-holder and the cleavage-post in air[6] and transferred to the vacuum chamber where it will be cleaved. In order to quickly ($\sim 1 - 5$ hour) transfer the sample from ambient pressure to the measurement chamber and keep there a suitable vacuum, the sample goes step by step through several chambers which are separated by valves and are pumped separately. The first one is the so called "fast entry" or "load lock", which is a small chamber and can be quickly pumped down from ambient pressure to 10^{-8} mbar pressure range. The second, preparation chamber has the vacuum in 10^{-10} mbar pressure range. Also, this camber is usually used as a storage for uncleaved (and in some cases cleaved) samples and sometimes is used as preparation chamber in which one can evaporate different materials on the sample surface, if needed. The last chamber is the measurements chamber. As mentioned earlier, the pressure here is less than 1×10^{-10} mbar. ARPES setup at *Diamond* is not an exception and its design is approximately described above. To be precise, the main chamber in this setup is divided to an upper one, in which sample is cleaved, and a lower one, in which measurements are performed. Obviously, the valve in between has to be open during the measurements, so, vacuum-wise they can be considered as one chamber.

As even a small magnetic field, comparable to the magnetic field of the Earth, can change trajectories of photoelectrons, the measurements chamber and the electron energy analyzer have to be shielded from such fields. The chambers should be made of μ-metal or/and have an internal μ-metal shielding. Also, the use of magnetic materials, such as stainless steel, should be avoided in the vicinity of the sample. This is one of the reasons why sample-holders and lower parts of the manipulators are made of a very clean copper. Another, and the main reason, why they are made out of copper is

---

[5]The sample surface can degrade even in such a high vacuum. A degradation time varies for different materials and can be from several hours to many days.

[6]Air-sensitive samples should be glued and transported in the argon atmosphere

its high thermal conductivity which is needed for cooling the sample down to several Kelvins. Low temperature is important for the resolution and is necessary for measuring the sample in the SC state. The cryogenic sample manipulator, used in ARPES setup at *Diamond*, allows to perform measurements at the sample temperature of 7K in the standard mode [174] and at less than 5K in the so-called single-drop mode, which can be reached by pumping the gas out of the cryostat.[7] These temperatures are very low considering that the manipulator has three rotational degrees of freedom. In this system the entire manipulator head is thermally decoupled from the room-temperature support tube and cooled by the exhaust gas of the cryostat. In order to improve contact between the sample-holder and the sample receptacle, it can be pressed down with 2 screws (see photo on Fig.2.2). Also, in Fig.2.2 one can find a door which covers entire sample receptacle (except small window, which allows a beam to reach the sample and photoelectrons to escape) and acts as a radiation shield for it. An additional cylindrical cooling shield is installed in the measurements chamber. This shield surrounds the entire manipulator head and is cooled down by an independent cryostat to a temperature of 18 K. This temperature is sufficient to condense all residual gases. All these measures together allow one to reach indicated above low temperatures of the sample. However, this is not a record temperature considering synchrotron-based ARPES setups. "One-cubed" ARPES setup which uses ^{3}He-cryostat and 3 levels of radiation shielding (1 K, 4.2 K, and 77 K screens) allows one to cool the sample down to temperatures lower than 1 K [175]. On the other hand, "One-cubed" end-station does not allow to change tilt angle and azimuth angle can be only roughly adjusted and usually requires raising the temperature up to 20 K. The flexibility in the k-space makes the ARPES setup at *Diamond* more convenient for the problems solved in this thesis. In addition, the sample can be heated up to 350 K with a heater located near the cold-head of the cryostat, which allows one performing temperature dependent measurements. Heating up the system causes thermal contraction of the manipulator head, which shifts the sample position vertically by ~0.3 mm. This drift can be corrected automatically with a software routine that uses the temperature of the manipulator support structure to control the vertical axis of the xyz-stage. [174]

---

[7]Unfortunately, this single-drop mode is usually unstable and thus not very convenient, which is why it is rarely used.
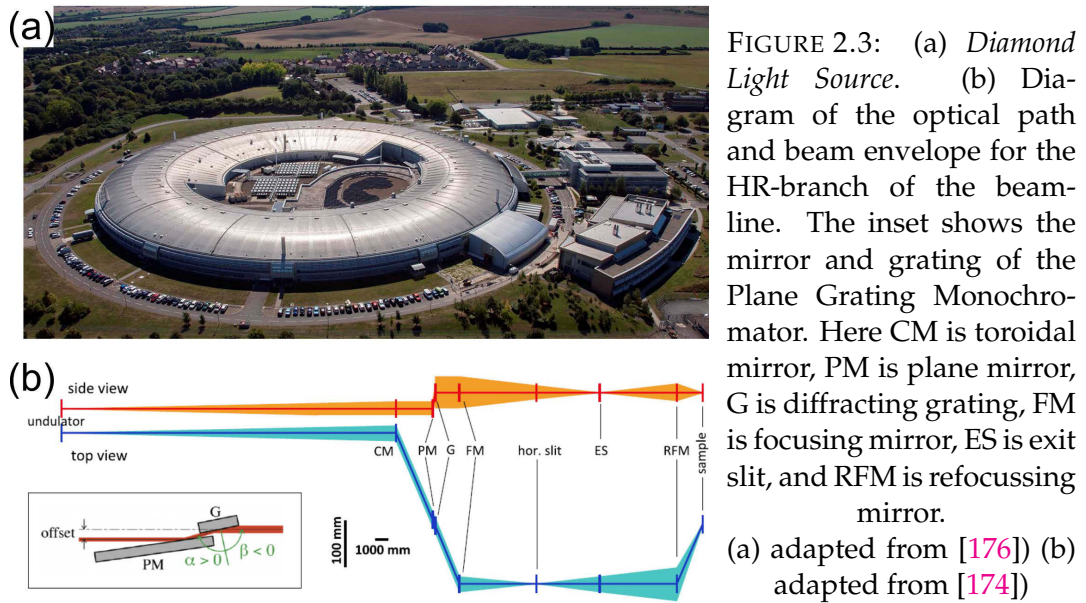
2.7   Synchrotron radiation

In principle, any monochromatic source with sufficient photon energy (> 5 eV) can be used as a light source for ARPES experiments. However, neither gas-discharge nor laser can give such flexibility as synchrotron can. It allows one not only continuously change photon energy in a wide range but also to choose the polarization. Its radiation is intense can be focused in a small spot.

When a charged particle is accelerated, it produces an electromagnetic radiation. This effect stands behind synchrotron radiation. Electrons with high energy, gained in the linear accelerator, are injected into quasi-circular storage ring where they move along the closed trajectory under UHV conditions. The storage ring consists of straight sections, between which the electron trajectory is bend by large electromagnets (called dipole magnets, or bending magnets). Diamond Light Source has a 562 m long storage ring with 48 bending magnets. The kinetic energy of electrons in the ring is 3 GeV [176]. As the electrons continuously lose their energy due to emission of electromagnetic radiation, they should be accordingly accelerated. For this purpose the radio frequency cavities are used. In order to produce synchrotron radiation which matches required photon energy and polarization, the electrons should pass through the undulator. The latter is placed in one of the straight sections of the storage ring. In the undulator magnetic field is periodically modulated by two arrays of magnets. Electron, passing through such periodic field, wiggles and emits electromagnetic radiation. The radiation from each wiggle in the series interfere with each other resulting in even more intense radiation with narrower spectral width than radiation from bending magnets. By varying the positions of the magnets in the undulator, it is possible to tune the properties of generated light, such as photon energy and polarization.

Beamline I05 of *Diamond* uses a variable polarization undulator of Apple-II type [177]. This undulator is able to produce light in the photon energy range from 18 to more than 500 eV of all four polarizations: linear horizontal (LH), linear vertical (LV), left-circular (CL), and right-circular (CR) ones.[8] The radiation from the undulator should be additionally monochromatized and focused onto the sample. For this purpose, the set of UV optics is used at I05 beamline, as shown in Fig.2.3. The light is monochromatized by a collimated Plane Grating Monochromator. A grating of 800 lines/mm is used. Collimation in the vertical plane is performed by the first toroidal mirror, which

---

[8]Here, all technical specifications of the undulator, monochromator, and focusing elements are taken from [174].

FIGURE 2.3: (a) *Diamond Light Source*. (b) Diagram of the optical path and beam envelope for the HR-branch of the beamline. The inset shows the mirror and grating of the Plane Grating Monochromator. Here CM is toroidal mirror, PM is plane mirror, G is diffracting grating, FM is focusing mirror, ES is exit slit, and RFM is refocussing mirror.
(a) adapted from [176]) (b) adapted from [174])

also forms the horizontal intermediate focus. The focusing mirror captures the collimated beam and focusses it onto the exit slit. The intermediate horizontal focus is formed by horizontal focusing of a toroidal mirror at 5 m upstream of the exit slit, thus making the intermediate focus astigmatic. The refocusing mirror is an elliptical torus. It demagnifies vertically by 3 and horizontally by 11/2. By design, the nominal horizontal beam spot size is approximately 50 μm over the whole photon energy range and with exit slit openings between 20 and 200 μm the vertical spot size varies between 7 and 70 μm.

Chapter 3

Temperature evolution of the electronic structure of FeSe

In this chapter, we explore the electronic structure of FeSe and its evolution in a wide range of temperatures by using high-resolution ARPES. We determine the actual scale of the changes in the electronic structure caused by nematicity in this material. We present experimental pieces of evidence for decreasing of "red-blue" shift with temperature increasing and comparison of these results with existing theoretical approaches for "red-blue" shift.

3.1 Effects of nematicity from low-temperature measurements

In this section we present results of the low-temperature ARPES measurements and extract scale of the nematicity induced changes from these data.

We start presenting our ARPES data by showing the Fermi surface map of FeSe in Fig.3.1(a). Both electron pockets at the corners of the BZ and hole pocket in its center can be seen on the map, which is a typical Fermi surface for iron-based superconductors. Fig.3.1(b) shows an experimental photoemission intensity distribution along the diagonal of the BZ ($M - \Gamma - M$ direction) measured at 10K which is well bellow the temperature of the structural transition. It represents dispersions which form both hole and electron pockets of the Fermi surface. A comparison of this result with band structure calculations of FeSe in the tetragonal phase (without nematicity) (see Fig.3.1(c)) shows good correspondence between them: all bands presented in the calculations can be identified in experimental electronic structure. There are two main distinctions between experimental and calculated electronic structure. First one is the renormalization of all bands near the Fermi level. The renormalization factor is orbital-dependent and varies from 2 to 9. The second

distinction is the blue/red shifts which are energy shifts of the dispersions near the center and the corner of the BZ in opposite directions in respect to Fermi level [20, 8, 22]. Such changes lead to the shrinking of the Fermi surfaces in comparison with the calculated ones which we observe on Fig.3.1(a). Both of these effects are intrinsic for all IBS (see section 1.3) and were observed experimentally in both nematic and tetragonal phases. This means, that they are not consequences of nematicity.
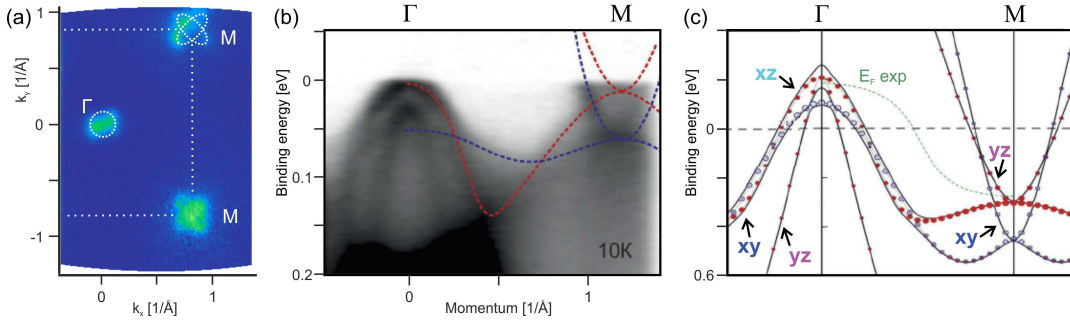

FIGURE 3.1: (a) Fermi surface map of FeSe measured with ARPES. Dashed lines schematically show the shapes of the pockets in the tetragonal phase and boundaries of the BZ. (b) ARPES intesity along the diagonal of the BZ. (c) band structure calculations of FeSe in the tetragonal phase. (a) adapted from [178]. (b) adapted from [179].

So, all distinctions which have large energy scale can be explained without involving nematicity. From such a good agreement between calculations in the tetragonal phase and ARPES results measured on the sample in the nematic phase, we can assume that the nematic order does not change the electronic structure significantly.

3.1.1   Effects of nematicity near the corner of the BZ

In order to check our assumption we should examine other parts of the band structure, not only the diagonal cut. Primarily, we should examine a part near the corners of the BZ, where, according to previous studies, a large nematic splitting was observed. Fig.3.2(a) shows a Fermi surface map of this part of the BZ. There are two electron pockets crossing each other. Both of them has a peanut-like shape[1]. This map was measured in a geometry, in which analyzer slit is parallel to the edge of 2-Fe BZ ($M - X - M$ direction). This allowed us to see both pockets. In other ARPES studies [58, 149], the measurements were carried out in a geometry, in which analyzer slit is parallel to the diagonal of the BZ ($M - \Gamma - M$ direction). Probably the best map measured in such

---

[1]Actually, it has a more complicated structure which will be disused later.

geometry is shown on Fig.3.2(b). As one can see on this map, one of the pockets is heavily suppressed by matrix elements. Furthermore, the ends of another pocket on its long axis are also suppressed.

Fig.3.2(c) shows a Fermi surface map near the corner of the BZ, obtained from calculations of the electronic structure at 250 meV, which corresponds to the experimental Fermi level position. This map is averaged in a small energy window of 5 meV. There is a good agreement between this map and the experimental one in Fig.3.2(a). Also, we compared several other energy-momentum cuts taken near the corner of the BZ (see Fig.3.2(d)) with those simulated by slightly broadened results of density functional theory (DFT) calculation (see Fig.3.2(e)). As one can see, not only high-symmetry direction cut but also other experimental cuts, as well as the Fermi surface map, show clear agreement with calculations. This confirms our assumption and allows us to build our interpretation of the presence of two ellipses in the corner of the BZ.
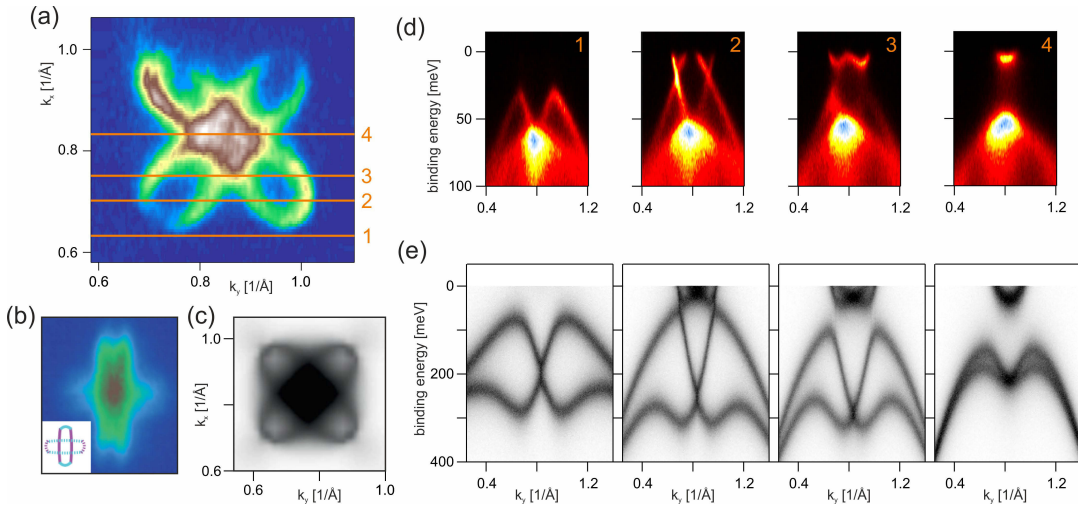

FIGURE 3.2: (a) Fermi surface map near the corner of the BZ measured with ARPES. (b) a similar map measured in another experimental geometry. (c) Fermi surface map near the corner of the BZ obtained from calculations. (d) ARPES spectra measured in the directions shown with lines on the plot (a). (e) intensity plots which represent cuts through calculated electronic structure.
(b) adapted from [58]. (c) and (e) adapted from [179].

In our interpretation, both observed pockets are also present in the tetragonal phase as well as in detwinned sample in the orthorhombic phase. They are formed by d_{yz} (or d_{xz} for another ellipse) orbital near the short axis of the ellipse and by d_{xy} near the long axis of the ellipse. This is in contrast to the popular interpretation [55, 57, 58, 147] in which two ellipses arise from two

different domains and both have $d_{xz,yz}$ orbital character and the other electron pocket which is present in band structure calculations and formed by d_{xy}, disappears below the transition. Here, it should be noted that these ellipses do not actually cross each other because of a spin-orbit splitting. There is an inner pocket formed by $d_{xz,yz}$ orbitals and the outer electron pocket formed by d_{xy} orbital which only resemble crossed ellipses.

Our interpretation does not exclude the fact, that nematicity influences the electronic structure in this part of the BZ. However, it plays only a secondary role. In this interpretation, the structure which we see on the map is a superposition of two different sets of crossed "peanuts"[2] originated from two domains. Each set consists of two orthogonal peanuts: a longer one and a shorter one. These two sets are orthogonal to each other since domains from which they are originated are orthogonal. As a consequence, each of the two observed peanuts is a superposition of two slightly different shapes.

In order to show that this is the case and to determine scale of changes in electronic structure caused by nematicity, we compare ARPES results with the fully relativistic band structure calculations of the orthorhombic phase. In these calculations values of in-plane lattice constants were unequal: a = 5.33426 Å, b = 5.30933 Å. These values were taken from neutron powder diffraction study [137]. The presence of the spin-orbit splitting was observed in all IBS [8]. Because of this, spin-orbit interaction was also involved in the present calculations. In the orthorhombic phase two diagonals of the BZ are not equal anymore. Because of this, in order to mimic superposition of signals from of two different domains, we show the superposition of the results of the calculations for both diagonals in one plot (see Fig.3.3(a) and (b)). The results for different directions are shown with colors: blue and green. There are also red lines on these plots, which represent results of calculations of the tetragonal phase and help to visualize changes. A noticeable difference between the electronic structure of different domains as well as between the electronic structure of the tetragonal sample and each of the two domains can be seen from these plots. It means that even believed almost negligible 0.45% changes in the crystal structure [137, 138, 139, 140, 141] can drive considerable changes in the electronic structure. The striking qualitative changes are splittings in the orthorhombic phase, which occur where bottoms of upper and lower electron-like dispersions touch other bands in the tetragonal phase.

---

[2]From this moment we are calling the shape of electron pocket peanuts since it different from elliptical.
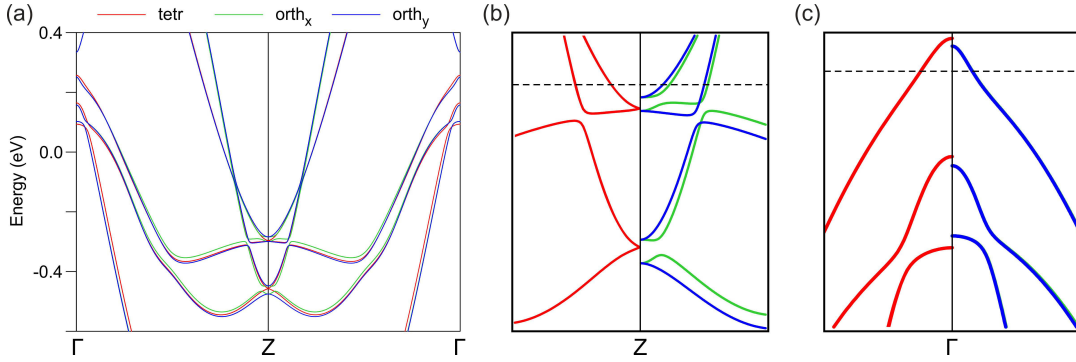
FIGURE 3.3: (a) full relativistic DFT calculations for the tetragonal and orthorhombic phases of FeSe. (b) and (c) zoomed-in view of regions near the corner and the center of the BZ, respectively.

In Fig.3.4(a) and (b) we show an experimental photoemission intensity distributions in the diagonal direction near the corner of the BZ, which was measured with different photon energies: 28 eV and 42 eV, respectively. These results exhibit features which are predicted by calculations of the orthorhombic phase but not present in calculations of the tetragonal phase. We emphasize, that any kind of misalignment is ruled out, since the data are taken from the maps of electron pockets recorded at different photon energies. In particular, they exhibit splitting at the bottom of both electron-like dispersions, as calculations predicted it. At first glance, these splittings are not seen on these plots. However, they can be seen in the energy distribution curves shown in Fig.3.4(c). Two components of the split upper dispersion appear as a peak and a well-pronounced shoulder at the left side of it on the EDCs and two components of the split lower dispersion appear as a peak and a shoulder at the right side of it. Fitting EDCs from Fig.3.4(a) allows us to estimate magnitudes of these splittings. They are 12 and 10 meV for upper and lower dispersions respectively, which is lower than those in the calculations. This difference is explained with the renormalization.

Also, it is seen in Fig.3.3(b) that green and blue dispersions cross the Fermi level in different places. So, in the experiment we should see two sets of Fermi surfaces, one set for each domain. Indeed, one can see signs of this on the map in Fig.3.5(a). At first glance, this electron-like Fermi surface indeed consists of only two peanuts. However, upon closer visual inspection the map reveals a more complex structure. The first observation which indicates this is a doubling, which is clearly seen near the end of the top-left "petal" of the Fermi surface (shown by black arrows in Fig.3.5). Another doubling is located near a base of this petal (shown by orange arrows). The second
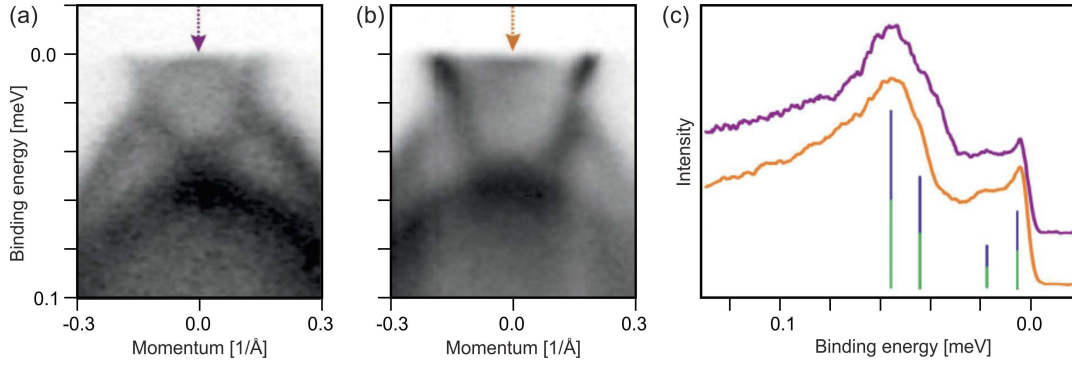
FIGURE 3.4: (a) and (b) photoemission intensity distribution in the diagonal direction near the corner of the BZ measured at 6.4 K with 42 eV and 28 eV photons, respectively. (c) EDCs obtained from (a) and (b) at momentum which corresponds to the BZ center.
Adapted from [179].

double-feature looks more fuzzy, because of the properties of used color-scale. Nevertheless, the doubling of both of these features is clearly seen as peaks in the momentum distribution curve taken along the red line on the map (see Fig.3.5(b)). Another peculiarity of the map, which is indicated the presence of two sets of ellipses, is the shape of the pockets themselves. One can see, that petals are not the same. If we try to fit a pair of identical peanut-like contours (see appendix A) orthogonal to each other to the pocket shape, it is not possible to obtain a good fit for all pockets simultaneously. For example, one can fit[3] quite well the upper-left petal Fig.3.5(d) (also see images of the map in Fig.3.5(e)), but lower-left and lower-right ones turn out to be too wide.

These two experimental observations allows us to conclude, that each of two peanuts which are seen in the map is a superposition of 2 contours with slightly different shape, some parts of which being suppressed by matrix element effects. Indeed, if we add a second pair of peanut-like contours, we can fit them to all experimental features on the map, including both doubled features in the upper-left petal Fig.3.5(f) and (h). This result shows that scale of changes caused by nematicity is small and is in a perfect agreement with calculations. Moreover, this result allows us to estimate a scale of energy-splitting quantitative. For this, momentum-splitting should be multiplied by Fermi velocity. The momentum-splitting near the ends of the petals is known from the pocket shape fit ($b_{long}/2 - b_{short}/2 = 0.02$ Å^{-1}), where b_{long} and

---

[3]All fits of the map presented on Fig.3.5(d)-(h) are "visual" fits done manually. An automatic fit of such map is a nontrivial task since some fragments of the map are suppressed. Such visual fit is enough to show the presence of two ellipses and make a rough estimation of the effect scale.
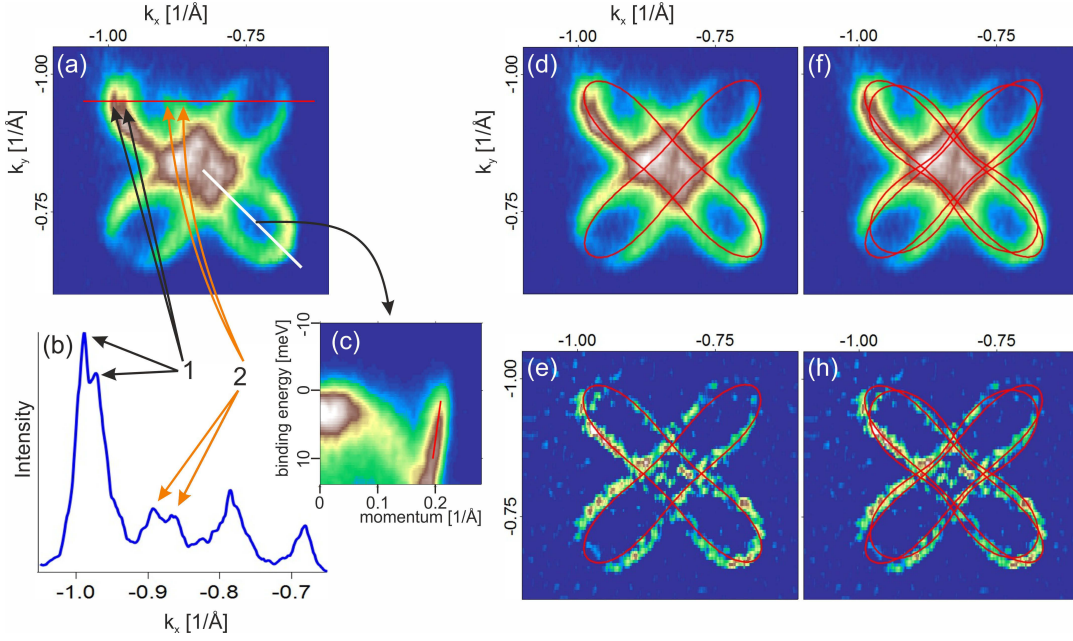
FIGURE 3.5: (a) Fermi surface map of the electron-like pocket near *A* point. (b) Momentum distribution curve taken along the red line on (a). (c) cut through the data set taken along the red line on (a). It represents the energy-momentum intensity distribution along the diagonal direction. (d), (f) one pair and two pairs of peanut-like shapes fitted to the pocket shape, respectively. (e), (h) the processed images of the map with the same contours as on (d), (f). The processing method is based on taking the 2-nd derivatives, which makes features sharper. These images cannot be treated separately from raw maps, because such processing can potentially lead to artifacts on it. However, as a supplement for raw maps, they help to make the result more ocular by emphasizes some features.

b_{short} are sizes of longer and shorter peanuts along the long axis, respectively (see Fig.A.2 in the appendix). Then the Fermi velocity can be determined from a diagonal cut (see Fig3.5(c)). For this, we fitted MDCs which allowed us obtain energy dependence of MDCs maxima position, which represent the dispersion shape, and fitted this dependence with a line. This gave us the value of Fermi velocity 0.625 eV/Å^{-1}. So, the energy splitting between two domains near the ends of the petals is $0.625 \times 0.02 = 0.0125$ eV = 12.5 meV. This result is reproducible: signs of this effect were observed in the data sets measured on another sample. For example, one can see the doubling on the left dispersion in Fig.3.4(b), near the Fermy level.

Also, in section 3.2, we will present results of high-temperature ARPES measurements, which support our interpretation. Specifically, these data shows splitting between d_{xy} and d_{yz} dispersions and elliptical shape of electron pockets in the tetragonal phase (for details see section 3.2).

3.1.2   Effects of nematicity near the center of the BZ

In order to have a general picture of the effects of nematicity in FeSe, we should also investigate the center of the BZ. For this region, the band structure calculations of the orthorhombic phase predict small changes caused by nematicity. Moreover, these changes are almost equal for both domains: blue and green lines on Fig.3.3(c) almost coincide, especially around 0.15 eV, where experimental Fermi level is. In any cyse, ARPES experiment exhibits different results. Fig.3.6 and Fig.3.7 represent experimental data obtained from two different samples in two different experimental geometries for this part of the BZ.

FIGURE 3.6: (a) Fermi surface map of the center of the BZ measured with 23 eV photons in a geometry in which analyzer slit is parallel to the edge of 2-Fe BZ. (b) and (c) spectrum measured through the pocket center in a direction shown with a dashed line on (a) and the same spectrum symmetrized with respect to zero momentum. (d) Fermi level MDC from the spectrum (b). (e) and (f) second derivative images of (b) and (c), respectively. Lines on (c) and (d) are guides to the eye, which emphases the bands position.

Fig.3.6(a) shows Fermi surface map measured with 23 eV photons, which corresponds to Γ point. This map reveals a more complex structure than just one round pocket predicted by calculations. It is more elongated along k_y direction than along k_x one and a clear double-feature can be seen in its right

part. Presence of such a double-feature in the left part of the map is not so obvious. However, high quality spectrum measured through the pocket center (see Fig.3.6(a)) displays doubling of d_{yz} dispersion on both sides of the spectrum: MDC obtained from this spectrum on the Fermi level (see Fig.3.6(d)) displays two pairs of peaks. This doubling is present not only at the Fermi level. This can be seen already from Fig.3.6(b), but it is better seen from Fig.3.6(f) which is a second derivative image of the symmetrized spectrum. Taking into account a well known fact that d_{xy} laies bellow displayed region we can conclude what we see in Fig.3.6(b, c, e, f) are the d_{xz} dispersion (top of which is below the Fermi level) and doubled d_{yz} dispersion (which crosses the Fermi level). Now, when we know that the doubling observed in the right part of the map is not an artifact and that this is not only one part of the pocket where the doubling is observed, we can interpret the map as a superposition of two orthogonal ellipses which are originated from two different domain orientations as it is shown in the figure. Indeed, most of the parts of these ellipses including ends of the horizontal ellipse on its long and short axis and ends of the vertical ellipse on its short axis correspond to features of the experimental map. A mismatch between ellipses and the experimental map is observed only near ends of the vertical ellipse on its long axis where the experimental map do not exhibit any features. The reason of such mismatch is a suppression of photoemission signal from these stats by matrix elements. This can be easily checked by carrying measurements in another geometry, for which matrix elements are different, and we have done this. Fig.3.7(a) represents a map measured with the same light, but on different azimuthal orientation: 45 degrees with respect to orientation of the previous sample. In this case, photoemission signal is present on the ends on long axes of both ellipses. Fig.3.7(b) and (e) show cuts through the map obtained in the directions shown with orange and gray line on the map, respectively. These cuts also show the doubling of the bands, which is better seen in second derivative images (Fig.3.7(c) and (f)) and even better seen on symmetrized second derivative images (Fig.3.7(d) and (g)). The energy scale of nematic splitting estimated from these cuts is 15 meV (see Fig.3.7(b)).

One can also notice a considerable intensity around $(k_x, k_y) = (0.05, 0)$Å^{-1} which dose not coincide with ellipses drawn on the map. This intensity at the Fermi level is formed by "tails" of the top of d_{xy} dispersion, which is below it, but is very intense and broad as it can be seen from Fig.3.7(b). We do not observe this in Fig.3.6(a) and in the lower part of Fig.3.7(a) because matrix
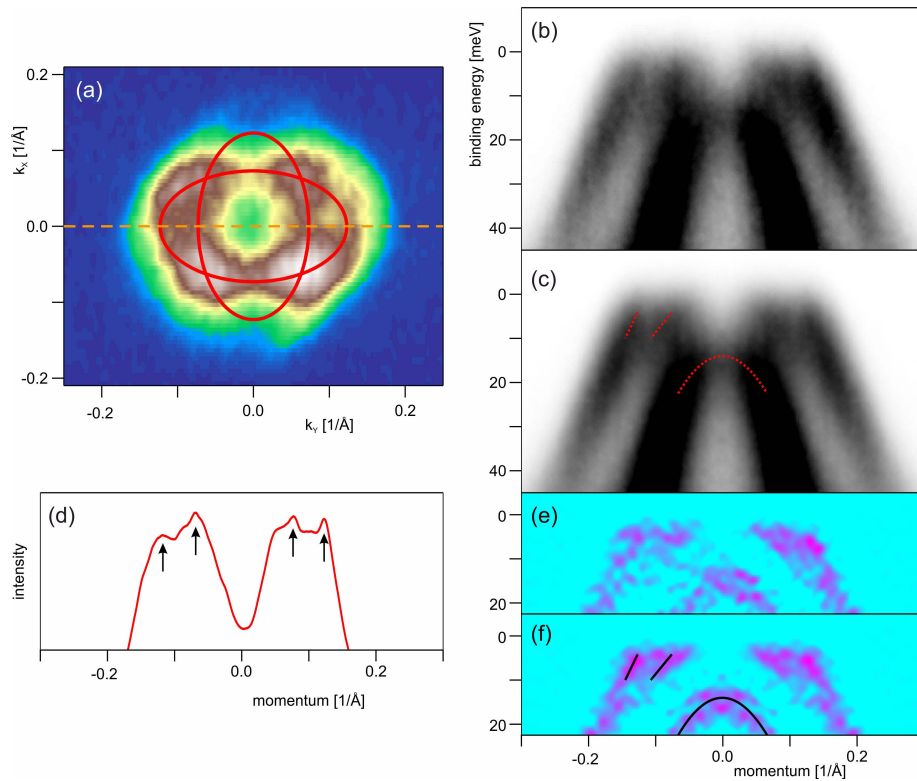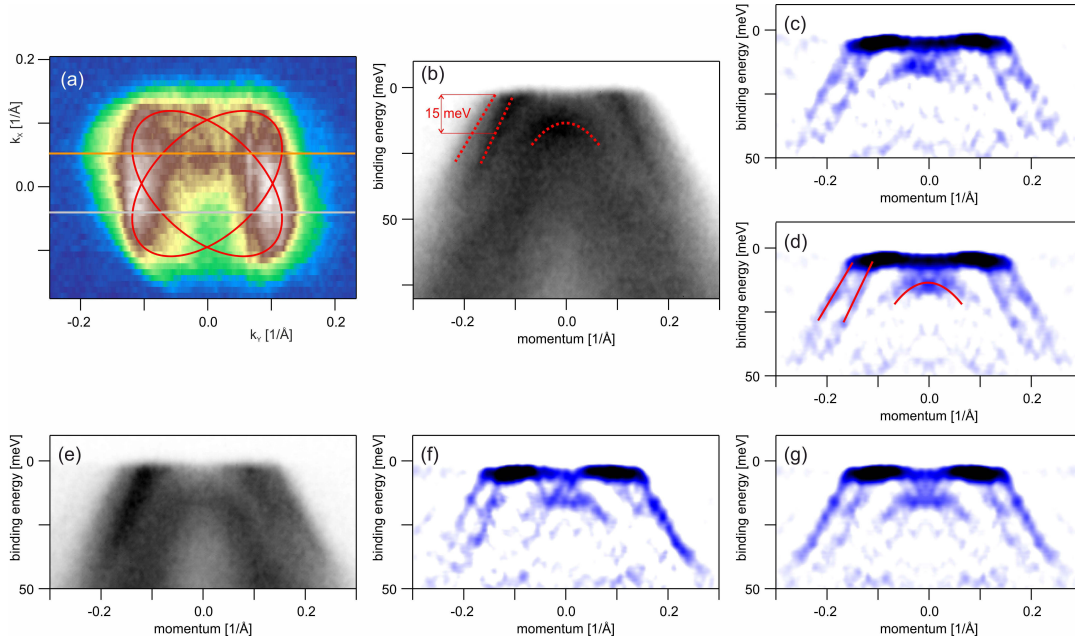
FIGURE 3.7: (a) Fermi surface map of the center of the BZ measured with 23 eV photons in a geometry in which analyzer slit is parallel to the diagonal of 2-Fe BZ. (b) and (c) cut along a direction shown on (a) with orange line and its second derivative image respectively. (d) the same as (c) but symmetrized. (e), (f) and (g) symmetrized second derivative image of three other cuts shown on (a) with gray lines depicted with the same numbers as images are.

elements are different there [4] and tops of d_{xy} dispersion are not so intense (see Fig.3.6(b) and Fig.3.7(e)). So, we conclude, that this intensity blob has nothing to do with real Fermi surface features and does not contradict the interpretation with two ellipses.

Observation of the dispersion splitting in two samples measured in different experimental geometries unambiguously demonstrates, that electronic structure in the center of the BZ is changed noticeably under nematic transition.

3.2 Temperature dependent shift of the dispersions

In this section we present the results of temperature dependent ARPES measurements in a wide rage of temperatures: from several Kelvins to values significantly above structural transition temperature. These results reveal an

---

[4]To measure the map we rotated the sample. In Fig.2.1 the beam direction is different from the direction to the analyzer. This means experiment geometries for polar position θ and $-\theta$ are not symmetric, which explains asymmetry of Fig.3.7(a).

unusual momentum dependent electronic structure evolution with temperature. Also, the results of these measurements provide additional evidence for our vision of the effects of nematicity described in the previous section.
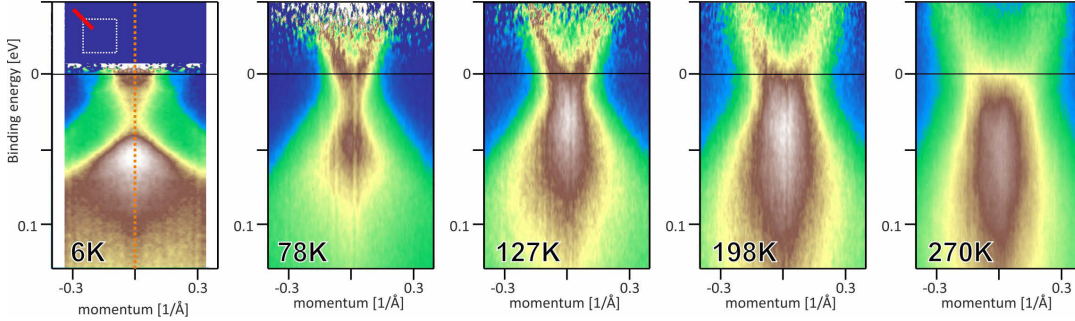

FIGURE 3.8: ARPES spectra measured at different temperatures along the diagonal direction through electron pockets in the corner of the BZ. The inset shows to which position in the BZ do these cuts correspond to. Here, all spectra are divided by Fermi function, which emphasizes the states above the Fermi level.
Adapted from [178]

We have recorded the temperature evolution of electronic structure near the center and the corner of the BZ from 6 to 270 K. Fig.3.8 shows set of spectra measured with 28 eV photons at different temperatures through electron pockets in the diagonal ($M - \Gamma$) direction (not all spectra from the set are shown). Here, it should be noticed, that these spectra[5] do not represent d_{xy} orbitals, since in this experiment geometry, photoemission from these states is suppressed by matrix elements, so, an electron-like dispersion which we see has d_{yz} orbital character. Fig.3.9 shows another set of spectra measured through electron pockets in the diagonal direction with 28 eV photons (here, also, only some spectra from the set are shown).

Already from visual inspection of these sets of spectra one can see that both of them imply the shifts of the features with temperature. In Fig.3.8, electron-like dispersions from the corner of the BZ move downward to higher binding energies with temperature increasing while the hole-like dispersions from the center of the BZ in Fig.3.9 move upward with temperature increasing. This shift is monotonic and observed in all parts of studied temperature range. This means the observed effect is somewhat different from the changes due to the nematic transition, which should occur in a relatively short range of temperatures around 90 K.

---

[5]Except of one for 6 K, which is a cut through the map measured in another experiment geometry. In this cut, both d_{xy} and d_{yz} can be seen.
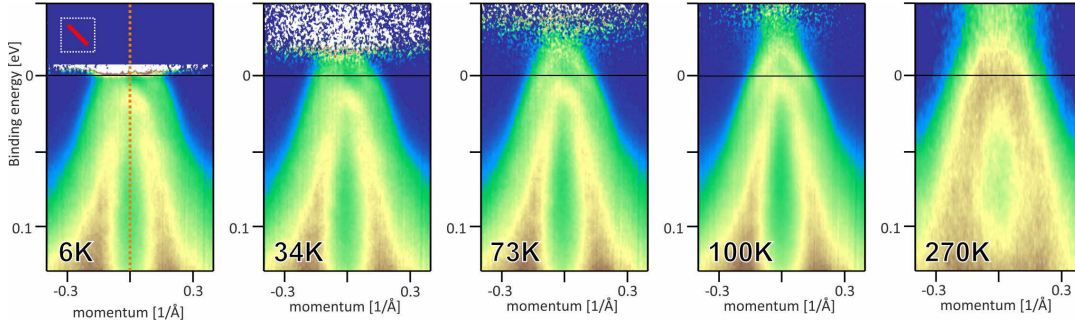
FIGURE 3.9: ARPES spectra measured with 28 eV photons at different temperatures along the diagonal direction through hole pockets in the center of the BZ. The inset shows to which position in the BZ these cuts correspond. Here, all spectra are divided by Fermi function.
Adapted from [178]

3.2.1 Shift of the despersions near the center of the BZ

For further quantification of details of the temperature evolution, we compared single energy distribution curves. Fig.3.10(a) shows intensity plot for EDCs from the center of hole-like dispersion (see orange line on Fig.3.9). This plot confirms the trend previously detected on Fig.3.9: bands shift up. The measure of the temperature-induced changes can be derived by comparing EDCs taken at the lowest and highest temperatures which are shown in Fig.3.10(b). The difference between positions of the peak, which represents the position of d_{yz} hole-like dispersion (depicted with the blue and red arrows) between 6 K and 100 K EDCs is 9.5 meV, which is well beyond the experimental errors. In Fig.3.10(d), we plot a temperature dependence of this peak position extracted from all spectra in the set (black symbols). Also, on high-temperature EDCs, another peak is observed. This peak is located above Fermi level at approximately -20 meV binding energy (see red curve in Fig.3.10(b)). It corresponds to the top of d_{xz} dispersion. We have tracked a position of this peak in the temperature range from 63 K to 100 K and plotted the result in Fig.3.10(d) with blue symbols. At lower temperatures tracking a position of this peak seems to be impossible because of too low intensity in this region of binding energies. As a consequence, signal-to-noise ratio is low. A broad shoulder in blue EDC at approximately 40 meV binding energy in Fig.3.10(b) corresponds to the d_{xy} dispersion. We did not track the temperature shift of this component because it is broad even at low temperatures.

A comparison of the EDCs from spectra measured with 23 eV photons at 6 K and 270 K in Fig.3.10(c) also demonstrates the shift. Features of 270 K EDC are extremely broad; however, the presence of two components is still detectable: right slope of the EDC has a shape, different from Gauss profile.
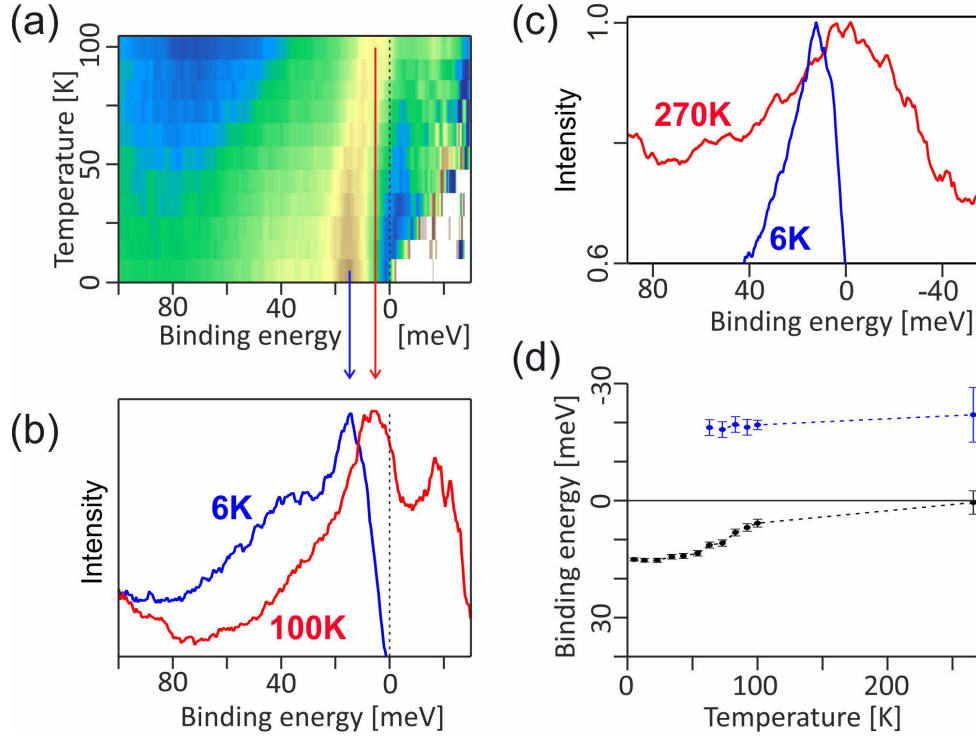
FIGURE 3.10: (a) Intensity plot which represents EDCs obtained from spectra from Fig.3.9 through the their center as a function of temperature. All EDCs are divided by the Fermi function. (b) comparison of 6 K and 100 K EDCs from (a). (c) similar to (b) but for data measured with 23 eV photons. (d) Position of maxima of EDCs as a function of temperature. Here, black dots represent lower maximum which corresponds to d_{yz} dispersion and blue dots represent higher maximum which corresponds to d_{xz} dispersion.
(a), (b) and (d) adapted from [178]

It has a kink at $\sim$ -25 meV. We have extracted positions of these two components by fitting the EDC with two Gauss profiles. A peak, which corresponds to the top of d_{yz} dispersion is located at -1.5 meV which is 13.5 meV higher than at 6 K. Since data presented in Fig.3.10(b) and (c) were collected with different photon energy and represent different k_z-s, we cannot plot the results of 270K EDC fit in Fig.3.10(d) as they are. However, from a comparison of low-temperature EDCs (blue curves in Fig.3.10(b) and (c)) we know the influence of k_z-dispersion: the peak position of the EDC obtained with 28 eV photons is 3 meV, lower than the peak position of one obtained with 23 eV photons. So, we plotted the results of the fit of 270 K EDC at 3 meV lower than their real positions to eliminate k_z-dispersion.

From Fig.3.10(d) it is seen that both d_{yz} and d_{xz} bands are sensitive to temperature and their qualitative behavior is the same. However, below the nematic transition, the lower dispersion shifts faster than the upper one. This

happens because of an additional splitting between them, caused by nematic-ity.
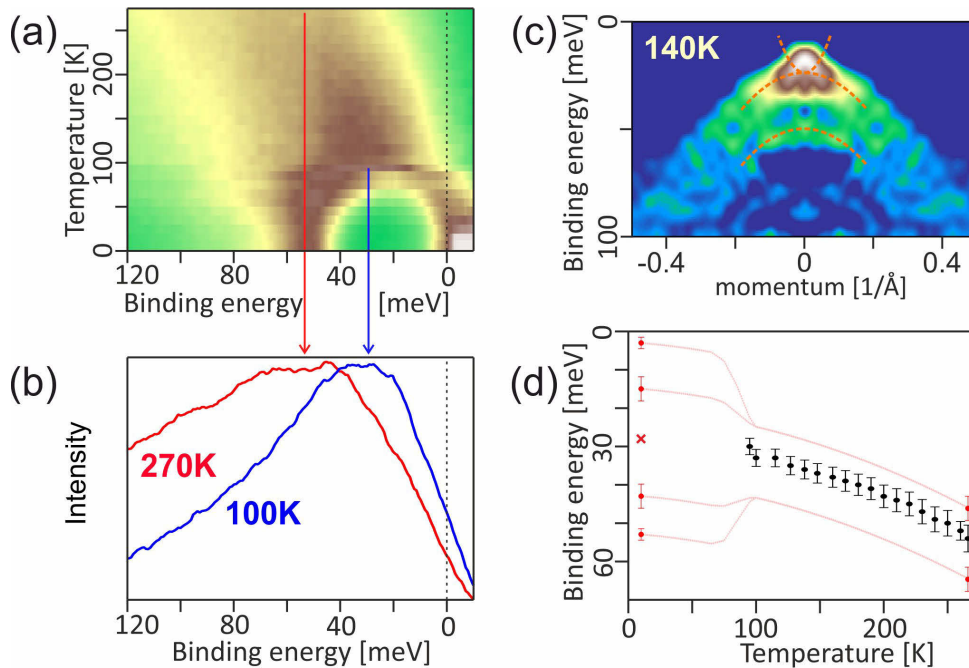

FIGURE 3.11: (a) Intensity plot which represents EDCs obtained from spectra from Fig.3.8 through their center as a function of temperature. All EDCs are divided by the Fermi function. (b) comparison of 100 K and 270 K EDCs from (a). (c) second derivative image of a spectrum measured through the corner of the BZ in the diagonal direction at 140 K. (d) overview of the temperature evolution of the band structure in the corner of the BZ: red dots represent results of multi-component fits of EDCs measured at 6 K and 270K; black dots represent single-component fits of EDCs; pink lines show sketch of the temperature evolution of the band structure which is based on our experimental results. (a) and (b) adapted from [178]

3.2.2   Evidences for band splitting in the corner of the BZ in the tetragonal phase

Fig.3.11 represents results of a similar analysis of the spectra measured through the electron dispersions. On Fig.3.11(a) we show an intensity plot which represents EDCs from the center of electron-like dispersion (see orange line on Fig.3.8). On this plot, one can see both effects temperature the gradual shift with temperature and nematic-induce changes which happen around transition temperature. At first glance, EDCs measured above nematic transition exhibit only one peak as well as in the previous studies [55, 56, 57, 58] and

support the scenario of huge nematic splitting in orthorhombic phase. Nevertheless, under close inspection, these EDCs reveal the presence of two components, as expected from the calculations of the tetragonal phase. Fig.3.11(b) shows EDCs measured in the tetragonal state for the lowest and highest temperatures. Tops of both curves are pretty flat which is different from Gauss shape which should be observed in the case of single-component EDC. The splitting is not seen directly Because of high temperatures and because of the stronger scattering in the energy range where these bands are located which is lower than the range where previously discussed tops of the hole bands are located. However, the splitting between these components can be visualized by taking a second derivative of a spectrum. A second derivative image of a high-statistic spectrum measured at 140K is sown on Fig.3.11(c). In this plot, one can track tops of two split dispersions. The lower electron-like dispersion is not seen because, as we said before, it is suppressed by matrix elements. In order to estimate the spitting size, we have fitted a part of 270 K EDCs near its top by two Gauss profiles as it is shown in the inset on Fig.3.12. Positions of the components extracted with fitting are shown in Fig.3.11(d) with two red dots at 270 K. They are split by approximately 20 meV.
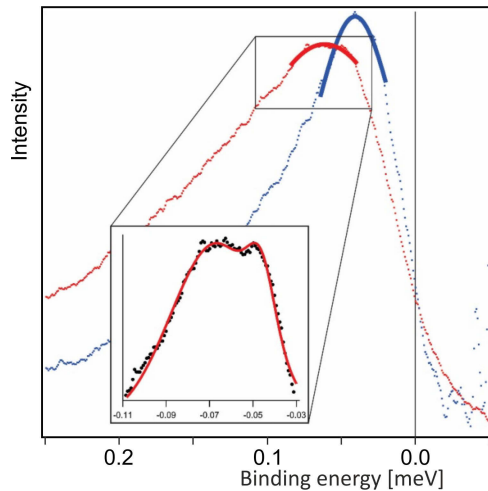
FIGURE 3.12: Details of fitting EDC from the corner of the BZ. The main plot shows EDCs from 3.11(b) (red and blue dots). Solid lines represent results of the single-component fit, without taking into account their fine structure. Such fit helps to track the temperature shift. The inset shows zoomed in the top of 270 K EDC (black dots) results of its fitting by two Gauss profiles (red line). Such fit helps to estimate band splitting in the tetragonal phase.

3.2.3   Shift of the despersions near the corner of the BZ

To estimate the band shift in the corner of the BZ above the nematic transition, we tracked the position of the maximum of a single broad feature without taking into account its fine structure. For this, we fitted tops of the EDCs (45 meV region around its maximum) with Gauss profile, like it is shown for 100 K and 270 K EDCs in Fig.3.12. Such an approach is suffusion for tracking the shift and at the same time allows to do this without a complicated

multi-component fitting which requires many parameters because of energy-dependent self-energy. The results of such fit are shown in Fig.3.11(d) with black dots. The band shift between 100 K and 270 K is 24 meV.

As we have already shown in section 3.1, in the orthorhombic phase these tow components split into four components. Four red dots in Fig.3.11(d) at 6 K represent results of fitting of orange EDC on Fig.3.4(c). Since EDCs has a more complicated structure in orthorhombic phase and their components are more spread, one can not use the same approach based on single Gauss profile fit which we use for tracking the shift in the tetragonal phase. Because of this, we consider the mean value of the binding energies of all four components as a value which catheterizes the position of the bands in the orthorhombic phase and can be compared with results of single-component fit of EDCs in the tetragonal phase in order to estimate the shift. The mean value of the binding energies of four components at 6 K is 28.5 meV which gives the total band shift between 6 K and 270 K of 27 meV.

Pink lines in Fig.3.11(d) show a sketch of the temperature evolution of the band structure in the corner of the BZ based on our experimental results. It represents both effects: the monotonic gradual shift with temperature and splitting two components into four induced by nematicity bellow 90 K.

3.2.4   Temperature evolution of the Fermi Surface

Naturally, such significant changes in the energy position of the bands should result in changes of the sizes and the shapes of the Fermi surfaces. Specifically, both electron and hole Fermi surfaces should become larger at higher temperatures. Fig.3.13(a-d) show the experimental Fermi surface maps measured at 6 K and 270 K near the center and the corner of the BZ. A direct comparison of these maps is in line with all previous statements and seems to be in agreement with the enlargement of all Fermi surfaces upon warming up the sample. We should note that a quantitative analysis of the size of the hole pocket at high temperatures seems to be very complicated. The distance between the peaks of the E_F MDC which is usually used for determining a pocket size become inconclusive because of several factors: At high temperatures the width of these peaks becomes comparable to the distance between them, also, another holelike dispersion approaches the Fermi level and modifies the E_F MDC with its spectral weight[6]. Both these factors shift the peaks

---

[6]This dispersion has a considerable spectral weight at E_F even at low temperatures when it is pretty narrow and distant from Fermi level (see Fig.3.7(b))
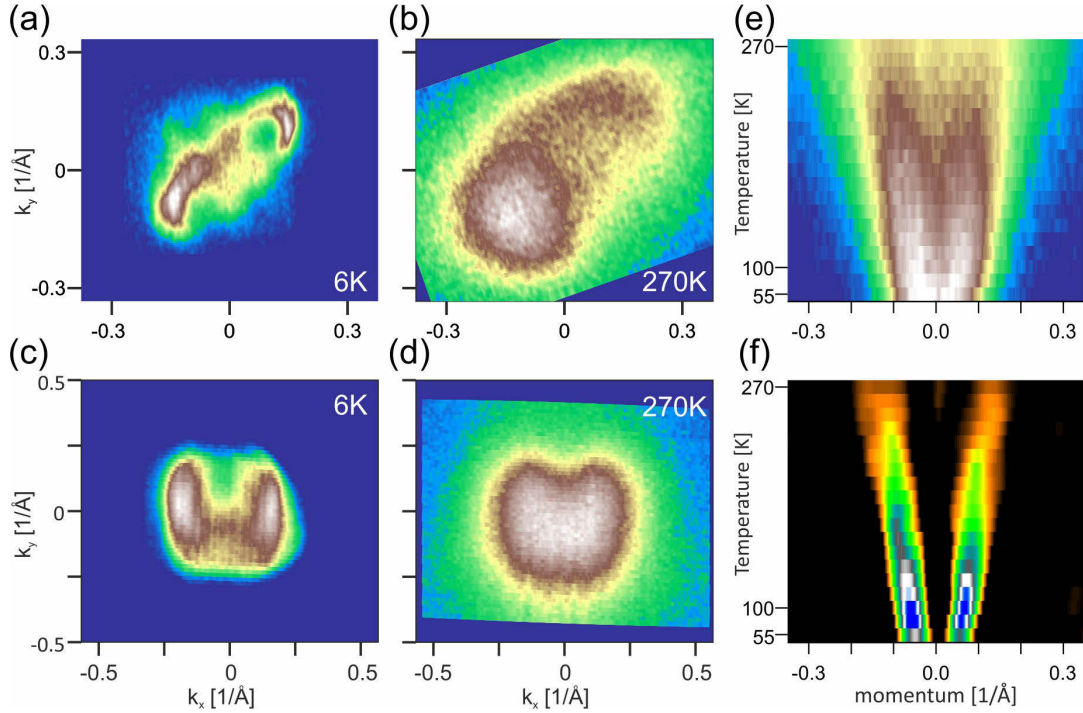
FIGURE 3.13: (a), (c) Fermi surface maps measured at 6 K near the corner and the center of the BZ, respectively. (b), (d) Similar maps measured at 270 K. (e) Intensity plot which represents E_F momentum distribution curves obtained from spectra measured at temperatures (temperature is not linear). (f) second derivative image of (e) (the second derivative is taken with respect to momentum).

to each other and as a consequence visually reduce the size of the hole pocket in Fig.3.13(d).

Changes in size of electron Fermi surface are also seen from comparison E_F MDC from spectra measured at different temperatures in the diagonal direction presented in Fig.3.13(e, f). I should remind that in such spectra only d_{yz} dispersion (one which forms the shorter axis of the peanut) is seen, and another one is suppressed by matrix elements. The temperature dependence of the momentum width of the electron pocket extracted by fitting these MDCs with two Gauss profiles is shown in Fig.3.15(b) [7]. This result confirms the shift of electronlike dispersions with temperature. Furthermore, the gradual character of the changes on whole temperature range without any considerable peculiarities near the temperature of the nematic transition confirms our previous conclusion, that influence of nematicity on the electronic structure is not as big as it was believed. Moreover, at 270 K the distance between peaks (the size the pocket along the shorter axis) is 0.26 Å^{-1},

---

[7]In Fig.3.15(b), the momentum width is shown as a fraction of it to the width obtained in band structure calculations.

which is smaller than the size the pocket along longer axis at this temperature and even smaller than it is at 6 K (0.4 Å^{-1}). In other words, the electron pocket remains elongated in the tetragonal phase, which can also be seen from the map Fig.3.13(b). This result is in contrast with an alternative interpretation in which elongated in the orthorhombic phase pocket, which is formed exclusively by $d_{xz,yz}$ dispersions, has to transform to the single one, with C4-symmetric shape in the tetragonal phase.
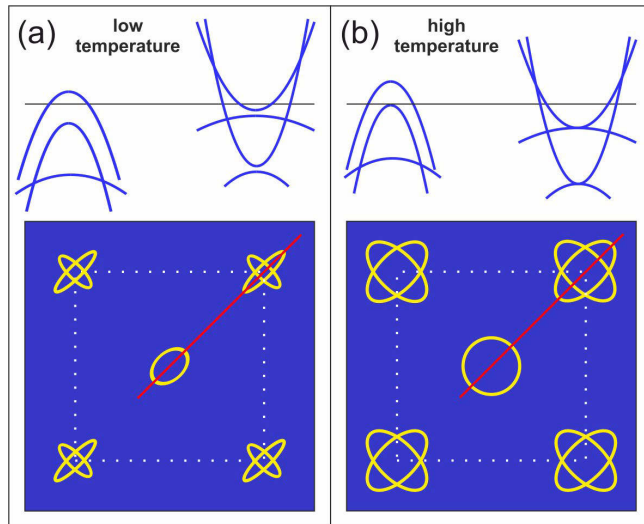
FIGURE 3.14: Sketches which represents the band structure and Fermi surface at low and high temperatures (left and right panels, respectively). Adapted from [178]

3.3   Discussion and conclusions

3.3.1   Anomalous temperature dependent shift of the dispersions

In Fig.3.14, we present a sketch which schematically summarizes the changes in the electronic structure of FeSe with temperature described in this chapter. Here, left and right panels represent low and high temperatures, respectively. The upper parts of the panels show the band structures and the bottom ones show the corresponding Fermi surfaces. Directions of the band shift near the center of the BZ as well as near its corner are opposite to the directions of the blue/red shift for these parts of the BZ. In other words, the blue/red shifts decrease with increasing temperature and the electronic structure tends to become more similar to the one predicted by calculations.

Changes in the electronic structure with temperature have been observed earlier and in different materials including IBSs. A shift of the dispersions with temperature was detected in undoped and electron-doped Ba-122 [22, 180]. Both studies show, that all dispersions shift in the same direction, which

leads to shrinking of the hole pocket and enlargement of the electron one upon warming up. As a consequence, a considerable increase of charge carrier density occurs. This is in contrast to the changes which we observe in FeSe, where sizes of all Fermi surfaces increase with temperature increasing. Interestingly, no noticeable changes in the Fermi surface of a hole-doped Ba-122 have been found between 14 K and room temperature [20]. We note that unlike FeSe, 122 compounds at low temperatures are in magnetically ordered phase and their electronic structure undergoes folding in this phase. Because of this and weaker three-dimensionality, the electronic structure of FeSe is simpler than that of 122 compounds. Thus, variations of the electronic structure with temperature should be seen more clearly in FeSe.

As it was said before, there are two theoretical approaches which attempt to explain red-blue shit. The first one is the electronic instability called the Pomeranchuk effect [24, 25, 26, 27, 28]. Forward scattering triggers a distortion of the Fermi surface which preserves the point group symmetry of the crystal. The area of both the electron and hole pockets increases (or decreases) so that the total charge density remains constant [24, 25]. The second approach is based on the renormalization of the bands by spin fluctuations via selfenergy effects [29, 30]. The blue/red shifts and shrinking of the Fermi surface reported by ARPES are considered as a direct consequence of the coupling to a bosonic mode upon a proper accounting of particle-hole asymmetry and the multiband character. It has been also suggested [181] that the blue/red shifts can be understood as a suppression of nearest-neighbor hopping due to spin/orbital orderings.

The observed by us temperature dependence of the electronic structure of FeSe may help to distinguish between these two theoretical approaches. The S_{+-} Pomeranchuk effect will result in the relative shift of the electron bands in the corners and hole bands in the center of the BZ, which will behave as in a mean-field order parameter. This shift will attenuate as temperature increases and will disappear at a particular critical temperature, as any mean-field order parameter. In the case of shift, which is induced by spin-fluctuations, the shift will decrease with temperature as well. However, it will evolve more smoothly since in this case its behavior is dictated by the softening of the spin-fluctuation spectrum.

To compare experimental results with theories, we considered two quantities which can be treated as the energy-derived and momentum-derived order parameters of the band shift. One parameter is the energy separation between the top of the d_{yz} hole-like dispersion (the middle one) and the value

which we use for characterization the band shift near the corner of the BZ (black dots and the red cross in Fig.3.11(d)). A temperature evolution of this parameter is shown in Fig.3.15(a). It is given in units of a fraction of this distance to the one obtained in LDA calculations (see Fig.3.1(c)). Another parameter is mentioned above the momentum width of the electron pocket. Temperature evolution of this parameter is shown in Fig.3.15(b) as a fraction of it to the width obtained in LDA calculations. The energy-derived order parameter in Fig.3.15(a) increases monotonicaly and slightly superlinearly with temperature increasing and exhibits week but noticeable a signature of the nematic transition. Such behavior reflects the experimental observations discussed above. The momentum-derived order parameter in Fig.3.15(b) exhibits almost perfect linear behavior on the whole range of temperatures. No noticeable signatures related to the nematic transition have been detected on it. Despite rather high temperatures, both parameters are still considerably departed from LDA calculations, especially energy-derived one, which at 270 K is less than 12% of the value obtained in LDA.
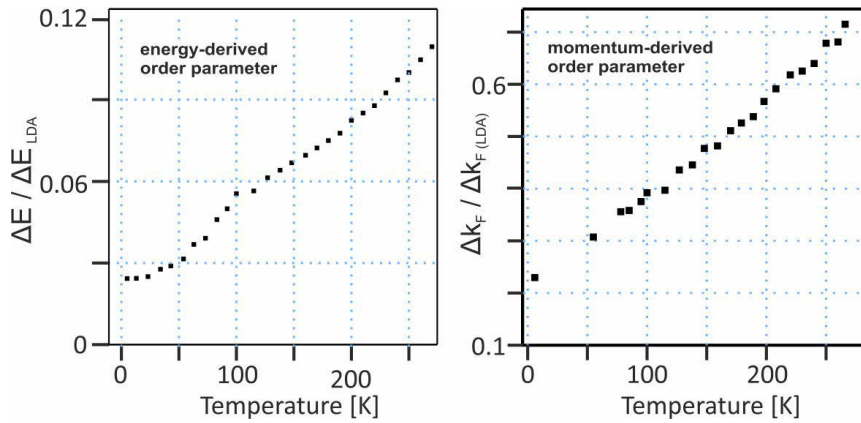
FIGURE 3.15: (a) Energy distance between the top of the middle hole band and the bottoms of the electron pockets normalized to the calculated value. (b) Momentum width of the electron pocket normalized to the calculated value.
Adapted from [178]

Neither Pomeranchuk effect based nor spin-fluctuation-based theoretical approaches seem to be in immediate agreement with the behavior of both parameters. Energy-derived order parameter does resemble the behavior of the typical mean-field order parameter in a temperature range distant from transition temperature which is expected in the case of the S_{+-} Pomeranchuk effect. However, the behavior of the momentum-derived order parameter

is not in agreement with this approach. The observed quasilinear behavior is most likely not expected also in the framework of coupling to spin-fluctuations. From this, we can conclude that if the effect is caused by Pomeranchuk instability, it has exceptionally high onset temperature and if the effect is caused by coupling to spin-fluctuations, a decay of the spin-fluctuation spectrum is very unusual. In any case, our results call for a more thorough theoretical investigation aiming at a quantitative explanation of the temperature relaxation of the blue/red shift.

3.3.2 Effects of nematicity

The observation of considerable (15 meV) splitting of d_{xz} hole-like dispersion is in contrast with our calculations which take into account only lattice deformation. Such calculations represent a case of phonon-driven structural transition (see section 1.1.5). The observed discrepancy indicates that the electronic structure deformation is probably caused by another interaction. Thus, the nematicity in FeSe is most likely not phonon- but electronically-driven.

A microscopic tight-binding model analysis [182] predicted that, nematicity increases splitting between tops of d_{yz} and d_{xz} hole-like dispersions. This is in agreement with our results (see Fig.3.10(d)) and this agreement is not only qualitative. The relation $\Delta^2 = \Delta_{SOC}^2 + \Delta_{Nem}^2$ which was suggested in [182] does work for our experimental results. Here Δ_{Nem} is nematic splitting; Δ_{SOC} is splitting between tops of hole-like dispersions in thetetragonal phase which is caused by spin-orbit coupling; Δ is the splitting in the orthorhombic phase. From Fig.3.10(d), we see that the splitting at 105 K (tetragonal phase) is 25 meV. So, the splitting in the orthorhombic phase should be $\Delta = (25^2 + 15^2)^{1/2} = 29$ meV. Which is up to errors equal to 31 meV splitting observed at 67 K (orthorhombic phase)

Also, one can notice that the energy scale of the splitting of d_{xz} hole-like dispersion and splitting between the bottom of d_{yz} and the top of d_{xz} electron-like dispersions are equal within error bars. This is consistent with results of a microscopic tight-binding model analysis [182] and is not surprising, since both splittings are associated with dispersions formed by the same orbitals.

3.3.3 Conclusions

We demonstrated that nematic transition at 87 K indeed impacts the low-energy electronic structure of FeSe near the center of the BZ as well as near its corner and established the energy and momentum scales of the nematic order. This scale is not as large as was suggested in earlier studies. The presence of two electron-like dispersions, which use to be considered as a consequence of nematicity can be reproduced by DFT band-structure calculations which do not take into account nematicity. Moreover, these two dispersions can also be distinguished in the tetragonal phase. The band-structure calculations which take into account the lattice deformation suggest small changes in this part of the electronic structure, and we detected these changes in our ARPES results. However, these calculations did not predict considerable splitting of the upper hole-like dispersion in the center of the BZ which was detected in ARPES results. This indicates to the electronic origin of the nematic order. Temperature-dependent measurements show that the electronic structure near the corner and the center of the BZ monotonically shift with temperature in opposite directions. The effect was observed in a wide temperature range which includes both tetragonal and orthorhombic phases. This shift reduces the size of the blue/red shifts and expands both parts of the Fermi surface at higher temperatures. Both parameters characterizing the effect in terms of energy and momentum are hard to reconcile with existing theoretical approaches.

Chapter 4

Three-dimensional superconducting gap in FeSe

As mentioned in the Introduction (section 1.3), despite high number of studies of the superconducting gap in FeSe and closely related compounds, there is no consensus on the size and symmetry of the gap in the full BZ. Moreover, there are no ARPES studies of the gap in pristine FeSe and results from slightly S-doped FeSe [149] are controversial. In this chapter we present the results of a high-resolution ARPES study of the superconducting gap function in whole 3D BZ in single crystals of FeSe.

To study superconducting gap with ARPES the knowledge of the details of an electronic structure of a material is necessary. Now, when we have determined the details of the low-energy electronic structure of FeSe with a high precision (see chapter 3) we can study the superconducting gap in this material.

Detailed knowledge of the gap function in iron-based superconductors can help to identify the mechanism of superconductivity in these materials.

4.1 Superconducting gap on the electron-like pockets

In order to explore the gap function in whole 3D momentum space, we have measured data sets for the center and the corner of the BZ with different photon energies. Fig.4.1 shows the experimental Fermi surface maps of electron pockets obtained from such data sets measured with 25 eV, 28 eV, 30 eV, and 42 eV photons. While 28 eV and 42 eV correspond to high-symmetry points of the BZ (A and M respectively), 25 eV and 30 eV correspond to points, which are in between them. All these data sets were measured from the sample in the superconducting state at temperature 5.5 K with linear horizontal

polarized light. As well as the results presented in the previous chapter, all
the maps exhibit two peanut-like shaped electron Fermi surfaces which cross
each other. The size of these pockets is changing with k_z. They are bigger near
A point and smaller near M point. In chapter 3, it was shown, that both these
pockets are present in the electronic structure of each of domains of the sam-
ple in the nematic phase, and that presence of two domains causes a doubling
of the pockets. In order to avoid complications with the gap magnitude ex-
traction from the data in which pockets are doubled, the data sets mentioned
above were measured in the experimental geometry in which only one set of
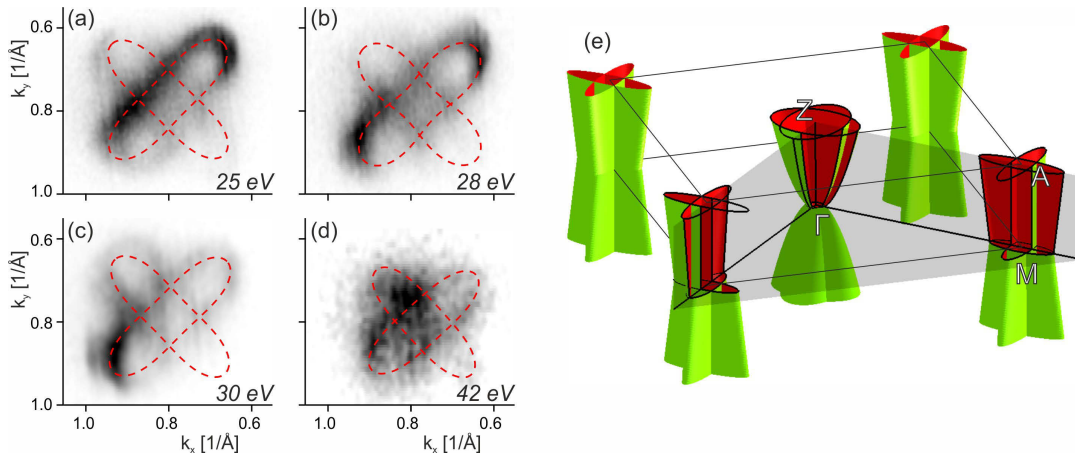pockets is visible at a time.

FIGURE 4.1: (a)-(d) Fermi surface maps of the region near the corner of the
BZ measured using different photon energies. (e) Schematic sketch of the
3D Fermi surface based on our experimental results. The fine structure of
electron pocket caused by nematicity is not displayed here.
Adapted from [183].

Now we proceed to extract the momentum variation of the superconduct-
ing gap on the electronlike pocket near the A point. Fig.4.2(a) shows the
Fermi surface maps measured with 28 eV photons. Red contour on it was
obtained by fitting a peanut-like shape (see Appendix A) on the results of
tracking the MDC peaks and represents a shape of the pocket. We started the
analysis of the gap anisotropy from comparison of the high-statistics spec-
tra (see Fig.4.2(b), (c)) measured in the superconducting state in directions
shown with horizontal lines on the map with the similar spectra measured
in the normal state. Fig.4.2(d) and (e) shows low- and high-temperature k_F-
EDCs from the spectra on Fig.4.2(b) and (c), respectively. These EDCs corre-
spond to the end of the pocket on its longer axis and the place where pockets
cross each-other (shown with stars on the map). Both pairs of EDCs exhibit

the shift of the leading edge position to higher binding energies upon entering the superconducting state indicating the gap opening. Moreover, the shift in Fig.4.2(d) is larger than shift on Fig.4.2(e). They are equal to 0.3 and 0.6 meV, respectively. This indicates that gap near the end of the pocket on its longer axis is smaller than in the place where the pockets cross each other.
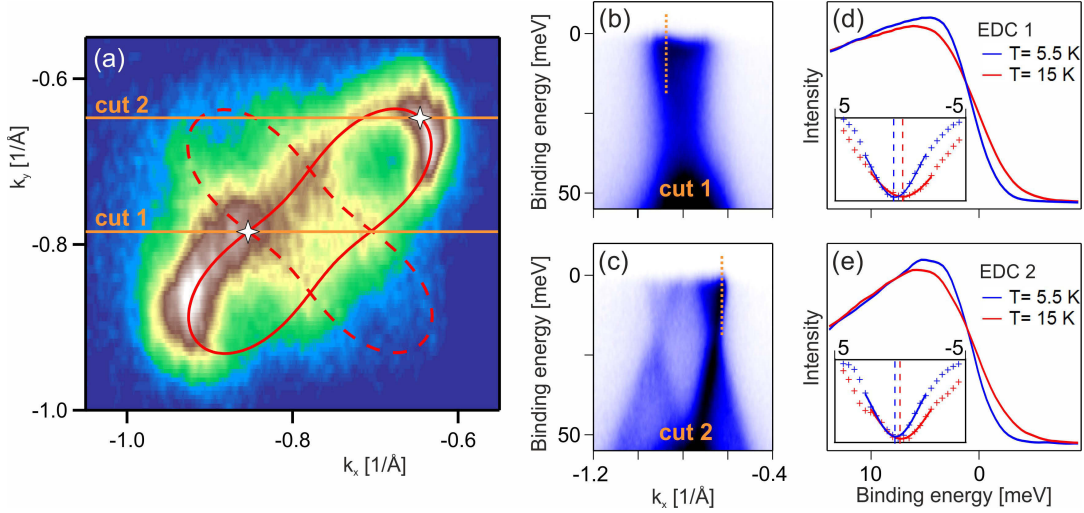

FIGURE 4.2: (a) Fermi surface map of the electron pocket near the A point (the same as Fig.4.1(b)). (b) and (c) spectra measured in the superconducting state in directions shown with horizontal orange lines on the plot (a). (d) and (e) comparison k_F EDCs from the spectra on plots (b) and (c) with EDCs from similar spectra measured in the normal state. Parts of the electronic structure from which these EDCs were obtained are marked with stars on the map and vertical lines on the spectra. The insets on (d) and (e) show curves which represent derivatives of the EDCs on these plots. The vertical dashed lines emphasis positions of extremes of the EDCs' derivatives. These extremes correspond to the leading edge positions of the EDCs.
(a), (d) and (e) adapted from [183].

For further analysis of gap superconducting anisotropy on the electron pockets we have extracted the leading edge position along the most intense peanut pocket.[1] We plotted the result as a function of angle in Fig.4.3(a). Already from this result obtained from the raw data, we can see a pattern in the leading edge gap behavior. However, in parts of the pocket where intensity is low because of the effects of matrix element the results are somewhat noisy. In order to compensate these effects and increase statistics in all parts of the pocket even more, we symmetrized the data set from Fig.4.2(a). We symmetrized it with respect to two axes: $k_x = k_y$ and $k_x + k_y + \sqrt{2}\pi/a = 0$

---

[1]Argumentation for the choice of a method of the superconducting gap magnitude extraction and description of the method can be found in Appendix B

which are longer and shorter axis of the pocket respectively. A Fermi surface map obtained from the symmetrized data set is shown on Fig.4.3(c). The result of the extraction of the binding energy of the leading edge from the symmetrized data set along the same contour is shown in Fig.4.3(b) with red markers. Also, we have extracted the leading edge position on visible parts of another peanut accentuated by black lines on top. The results for these parts are shown in Fig.4.3(b) with black markers. The angular dependence of the leading edge position is the same for both pockets which is a direct evidence of an anisotropic superconducting gap on electron pockets. The gap on these pockets has $C2$ symmetry: the gap maxima which correspond to the lowest leading-edge position are located on the shorter axis of the peanut and the gap minima which correspond to the highest leading-edge position are located on its shorter axis.
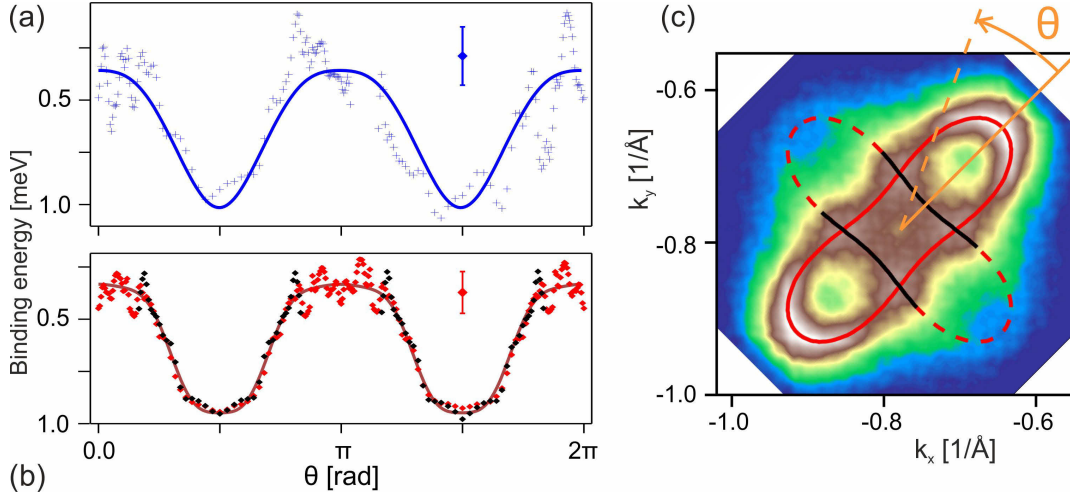
FIGURE 4.3: (a) Binding energy of the leading edge of k_F-EDCs on the electron pocket obtained from raw data. (c) Fermi surface map obtained from the symmetrized data set. (b) Binding energy of the leading edge of k_F EDCs obtained from symmetrized data set. Here red markers correspond to solid red contour on top of the map, and black markers correspond to black lines on top of the map. We shifted the black markers by 90 degrees, in order to match the results from the same parts of different ellipses. Solid lines in (a) and (b) represent the results of data fits. Adapted from [183].

Fitting the data with a periodic function $\varepsilon = A_0 + \frac{A_1}{2}cos(2\theta) + \frac{A_2}{2}cos(4\theta)$, where A_0, A_1, A_2 are free parameters gives the following results: A_1 which is an amplitude of the component with $C2$ symmetry is 0.64 ± 0.05 meV and A_2 which is an amplitude of the component with $C4$ symmetry is 0.11 ± 0.05 meV (see the solid curve in Fig.4.3(b)) which results in the total amplitude of the gap variation of 0.64 meV. Adding components with $C6$ and $C8$ symmetry

to the fitting function results in negligible amplitudes of these components. Fitting the raw data with the same function gives almost the same results (see the solid curve in Fig.4.3(a)). This proofs that symmetrization did not ruin any important features and this procedure could be used.

As mentioned in chapter 3, each of two orthogonal peanuts of the electron Fermi surface is a superposition of two components which originate from two different orthorhombic domains. Thus, it can be useful for interpreting the result, to know which exactly component has been analyzed. From the comparison of the map in Fig.4.2(a) with the one in Fig.3.5 which represents the results measured with the same light but in another experimental geometry, one can see that the size and the shape of the most intense pocket of former matches with the size and shape of the shorter peanut in Fig.3.5. Thus, we can conclude that we analyzed the shorter peanut. The finite intensity from the dispersions, which form the longer peanut, still can be present and influence our results. Specifically, it could shift the leading edge position down to the high binding energies near the ends of the shorter peanut at its longer axis. This happens because, here, the dispersion which forms the longer peanut runs just slightly below the dispersion which forms the shorter one and can contribute spectral weight near the Fermi level to EDC taken at k_F of shorter peanut. Consequently, the amplitude of the leading edge gap anisotropy can be even higher than our estimation.
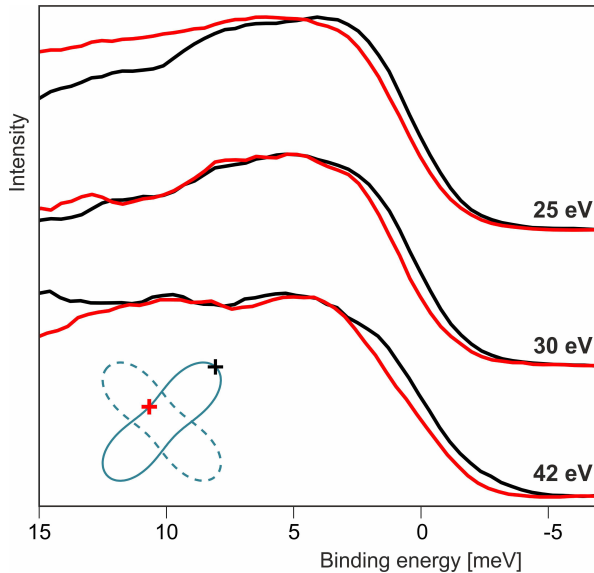
FIGURE 4.4: The EDCs taken from parts of the electron pocket marked with crosses on the schematic image of the pocket. Different pairs of EDCs correspond to data sets measured using different photon energies.

In order to extract k_z dependence of the superconducting gap on electron pockets, we have also analyzed other data sets (see Fig.4.1(a, c and d)) measured using different photon energies. We compared EDCs taken from parts of the most intense peanut on its longer and shorter axes for each of three

Photon energy	Leading edge gap anisotropy
25 eV	0.45±0.10 meV
28 eV (A-point)	0.64±0.05 meV
30 eV	0.60±0.10 meV
42 eV (M-point)	0.70±0.15 meV

TABLE 4.1: leading edge gap anisotropy on the electron pocket for different k_z values.

data sets. These EDCs are shown in Fig.4.4. All pairs of EDCs demonstrate the difference in the leading edge position. A sign of this difference is the same as for 28 eV data set analyzed above: the leading edge on the shorter axis is lower than on the longer axis. The amplitude of the leading edge gap variation, i.e., the difference in the leading edge position between EDCs on Fig.4.4, is given in Table 4.1. From this table one can see that while the pattern of the gap anisotropy remains the same, its amplitude changes with k_z. The amplitude of the gap anisotropy near high-symmetry points is apparently larger than between them.

4.2   Superconducting gap on the hole-like pocket
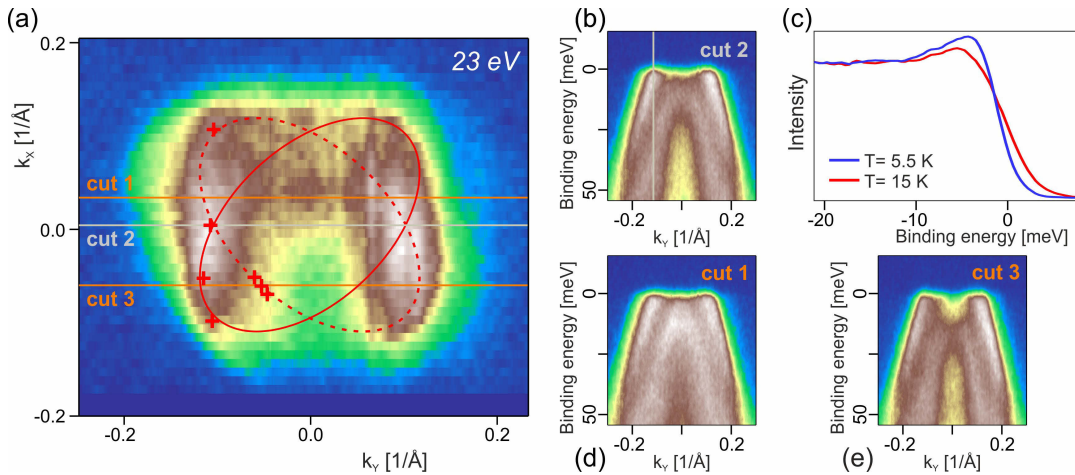
FIGURE 4.5: (a) Fermi surface map of the hole pocket measured at 5.5 K with 23 eV photons (corresponds to Z point). (b), (d) and (e) spectra measured in directions shown with lines on the map. (c) k_F EDCs obtained from spectrum in (b) and a similar spectrum measured in the normal state. Adapted from [183]

Now let us turn to the hole Fermi surface in the center of the BZ. Fig.4.5(a) shows a Fermi surface map of the hole pocket measured with 23 eV photons which corresponds to Z point in 3D BZ. It exhibits two elliptical hole pockets

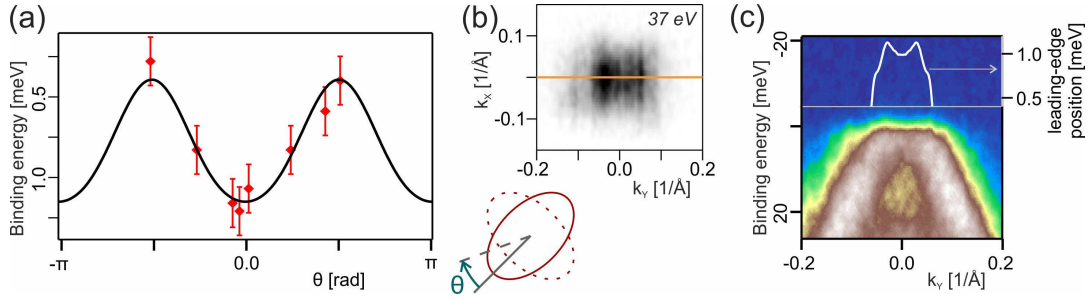FIGURE 4.6: (a) Binding energy of the leading edge of the k_F EDCs taken from parts of the hole pocket marked with crosses in Fig.4.5(a). (b) Fermi surface map of the hole pocket measured at 5.5 K with 27 eV photons (corresponds to Γ point). (c) cut through the direction shown with a line on (b). White line represents a variation the leading edge position near zero momentum.
Adapted from [183].

which originate from two different domain orientations in the nematic state (for details see subsection 3.1.2). The presence of the superconducting gap on the hole pocket can be seen from comparison k_F EDCs in Fig.4.5(c) which are obtained from the spectrum measured in the superconducting state (see Fig.4.5(b)) and a similar spectrum measured in the normal state. The leading-edge shift between these EDCs is 0.8 meV. In order to estimate the superconducting gap anisotropy on this Fermi surface, we have analyzed EDCs from its parts marked with the red crosses on the map. We did not analyze the right part of the map because of a stripe-like artifact on it which most likely is originated from the sensor defect. Also, we did not analyze the part of the pocket depicted with solid ellipse in ($k_x > 0$, $k_y < 0$) quarter because intensity of another hole-like dispersion (d_{yz} dispersion) is high in this part of the data set (see Fig.4.5(d)), while in ($k_x < 0$, $k_y < 0$) quarter, it is considerably lower (see Fig.4.5(e)). This bright dispersion can influence the leading edge position of k_F EDCs, and, in addition, it makes it difficult to determine k_F with proper precision. Results of expression the leading edge position from the analyzed EDCs are shown in Fig.4.6(a). This plot clearly shows that superconducting gap on hole Fermi surface is also anisotropic and its maximal value is larger than on electron pocket. The gap is maximal on the shorter axis of the pocket and minimal on its longer axis. Fitting these results with a periodic function yields a difference between the gap minimum and maximum of 0.75 ± 0.1 meV.

Upon approaching the Γ point, the hole pocket becomes considerably

smaller (see Fig.4.6(b)). Small pocket size (about 0.06 $\overset{\circ}{A}^{-1}$ in diameter) together with lower resolution at higher photon energies (for measuring electronic structure near Γ point we should use 37 eV photons) makes impossible to disentangle details of the Fermi surface which apparently also consists of two ellipses originated from two domain orientations and, as a consequence, a proper analysis of the leading edge gap anisotropy seems to be impossible. However, the presence of the gap itself is apparent. Moreover, the presence of the gap follows from the leading edge position behavior (see the inset on Fig.4.6(c)) extracted from the cut shown in Fig.4.6(c) which is taken through the pocket center. Presence of a minimum in the angular dependence of the leading edge position indicates the back-folding of the dispersion due to superconductivity: In such case, when the top of the dispersion is located close to the Fermi level, opening of the gap results exactly in this behavior of the leading edge position [184]. In the case of absence of the gap, the angular dependence the leading edge position should be almost flat near the top dictated mostly by the Fermi function. This happens because the dispersion is broad and its top is near the Fermi level, which results in nearly uniform density of states near the Fermi level in the momentum range in between the Fermi level crossings.

4.3   Discussion and conclusions

In Fig.4.7 we present an overview of our experimental findings as regards the 3D gap function in FeSe. Here, the variation of the gap magnitude is shown with different colors of the corresponding parts of the Fermi surface. In this figure, we show only the Fermi surface corresponding to a single domain. The superconducting gap on both parts of the Fermi surface is anisotropic in k_x-k_y plane as well as in k_z direction. The gap on all Fermi surface sheets has two-fold symmetry. A maximal magnitude of the gap on the hole pocket is bigger than a maximal magnitude of the gap on the electron pockets.

This result is in agreement with a previously detected correlation between the size of the gap and degree of spin-orbit splitting (see Ref.[185]). Indeed, the gap is larger near the center of the BZ where the spin-orbit splitting is also larger (see chapter 3), and it is smaller near the corner of the BZ, where the spin-orbit splitting is smaller. Besides, a correlation between the gap magnitude and orbital character can be noticed. The gap is larger on parts of the Fermi surface which are formed by d_{xz}/d_{yz} states: the hole pocket and parts of the electron pockets near the shorter axes, and it is small on parts which are
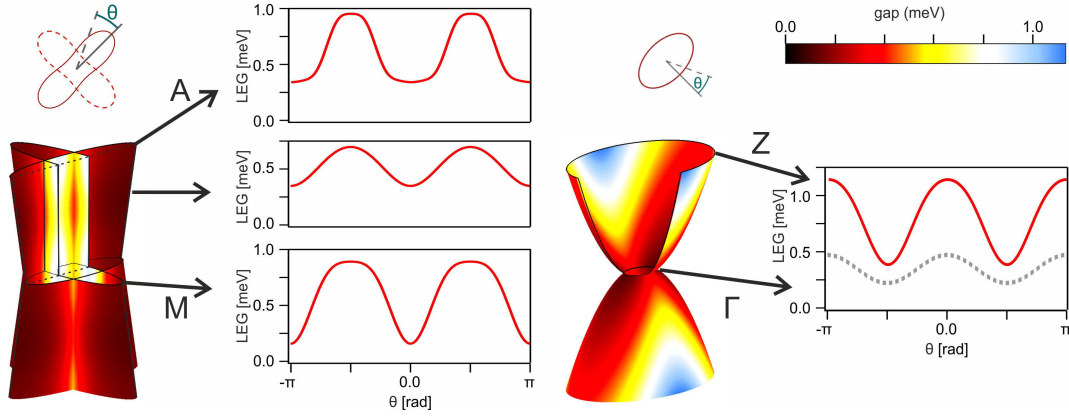
FIGURE 4.7: Overview plot which shows variation of the superconducting gap magnitude in on all sheets of the Fermi surface. Here, the variation of the gap magnitude is shown with different colours of the corresponding parts of the Fermi surface.

formed by d_{xy} states: parts of the electron pockets near there longer axes. A similar correlation was observed in hole-doped $BaFe_2As_2$ [186]. This pattern of the gap anisotropy is in a qualitative agreement with the one obtained in QPI study [151]. As we said before, leading edge gap is always smaller than the real gap size, and this explains the difference in absolute values of the gap between studies.

4.3.1 Theoretical interpretation

Strong anisotropy of the superconducting gap observed on all Fermi surface sheets in FeSe is contrasting with the gap structure expected in conventional spin fluctuation pairing theory. In case of FeSe, this theory predicts almost isotropic gap on the hole pocket and anisotropic gap on electron pocket, but this anisotropy is in antiphase to one, observed in the experiment [187] [151, Supplementary materials]. However, our experimental results can be explained with the concept of orbital-selective Cooper pairing suggested recently [151, 188]. According to this concept, the concentration of the pairing in the particular orbital channel may arise from differences in the correlation strength for electrons with different orbital character. Within this concept, smaller gap in regions, where d_{xy} is dominant, can be explained by correlations which generate incoherence for these states [189, 190] and suppress pairing. On the other hand, the realization of this scenario requires quasiparticle spectral weights for the d_{xz} and d_{yz} stats be different. However, our ARPES results do not exhibit significantly different Z-weights of these orbitals, because both electron pockets are present within a single domain

and the corresponding peaks of the spectral function are equally sharp (see Fig.3.5).

Also, the observed variations of the superconducting gap can be explained by the influence of nematicity by itself. Theoretical study presented in [191] demonstrates that in case of breaking the rotational symmetry, s-wave and d-wave pairing channels mix, resulting in the gap with two-fold symmetry. This approach does not require different Z-factors for each orbital.

4.3.2 Conclusions

We have demonstrated the presence of the superconducting gap on the electron Fermi surfaces of FeSe which was not observed in ARPES before because of its small size. Moreover, we have extracted the gap variation across these Fermi surfaces at deferment k_zs as well as across the hole Fermi surface. The gaps on all Fermi surfaces are strongly anisotropic with two-fold symmetry. No nodes were observed. Our results are in approximate agreement with QPI results. Such gap variations can be explained by both orbital-selective Cooper pairing as well as the influence of nematicity by itself.

Chapter 5

Superconductivity-induced nematicity in LiFeAs

The influence of nematic order on the electronic structure and superconductivity in FeSe has been discussed in the previous chapters. The question arises whether the nematic fluctuations are universal in IBS. As was discussed in the first chapter, LiFeAs is a very important representative of IBS and any relation between the nematicity and electronic structure of this well-known material would be of great interest. Since previous studies have not found any noticeable influence, in order to study possible signs of nematicity in LiFeAs we revisited its electronic structure including the gap function using the highest possible energy and momentum resolutions. In this chapter we discuss the results of these experiments.

For this study, LiFeAs single-crystal plates with dimensions of $3 \times 3 \times 0.1$ mm^3 have been selected, which were grown by self-flux using the standard method. [98] The samples have cleaved in the ultra-high vacuum at low temperatures. All cleaves resulted in mirror-like surfaces.

We start presenting our ARPES data by showing the Fermi surface map in Fig.5.1(a) and a spectrum in Fig.5.1(b) measured in a high-symmetry direction which is diagonal of the 2-Fe BZ. These two plots represent all main features of the electronic structure of LiFeAs. They exhibit two Fermi surfaces centered around Γ point (the center of BZ) which are formed by hole-like dispersions. The larger hole pocket which has square-like shape is formed by d_{xy} dispersion and the smaller hole pocket which appears on the map as a "dumbbell" at (0 Å^{-1}, 0 Å^{-1}) and as four-points feature at (-1.2 Å^{-1}, -1.2 Å^{-1})(the center of the second BZ) is formed by d_{xz}/d_{yz} dispersion. There is one more hole-like dispersion which does not cross the Fermi level and has d_{yz}/d_{xz} orbital character.[1] There are also two Fermi surfaces centered around M point (the corner of the BZ) which are formed by electron-like

---

[1]Two central dispersions (one which forms the small pocket and one which is below Fermi level) changes their orbital character under rotation in XY plane. For the direction

dispersions. These two Fermi surfaces cannot be resolved on Fig.5.1(a) be-
cause this map was measured with high-energy photons (80 eV). However,
dispersions which form inner and outer electron pockets are can be resolved
on the spectrum in Fig.5.1(b) measured with 21 eV photons. The dispersion
which forms the inner electron pocket has d_{xy} orbital character. The disper-
sion which forms the outer pocket has d_{yz} orbital character for a direction
shown with a dashed line on the map and d_{xz} for another one.
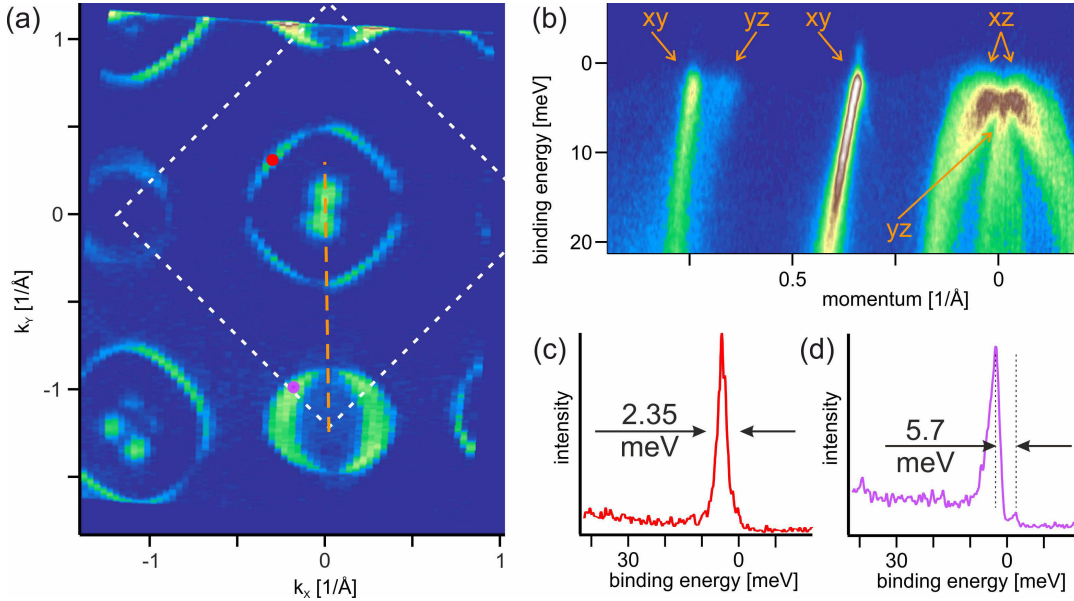
FIGURE 5.1: (a) Overview Fermi surface map of LiFeAs measured with
80 eV photons. (b) Spectrum measured in a direction shown the dashed
line in (a) using 21 eV photons. This spectrum represents all dispersions
which cross the Fermi level. (c-d) k_f-EDCs obtained from parts of the
Fermi surface marked with dots.

To underline the precision of our measurements, in Fig.5.1(c, d), we show
two typical k_F-EDCs obtained from spectra measured through the hole and
electron pockets with 18 eV and 21 eV photons, respectively. A high resolu-
tion which follows from sharp EDC peaks together with an ability to resolve
coherence peaks above the Fermi level demonstrates that the superconduct-
ing gap in LiFeAs can be measured by ARPES with very high precision.

5.1 Superconducting gap

Fig. 5.2 shows the temperature evolution of the spectrum from Fig. 5.1(b).
Here, all spectra are divided by Fermi function in order to enhance a signal

---

shown with a dashed line on the map, the orbital character is d_{xz} for the former one and d_{yz}
for the latter one, as it is depicted in Fig.5.1(b).

from states above the Fermi level. It is seen that the gap opens up at ∼17 K and gradually increases with the temperature lowering. This critical temperature is in line with earlier studies. Besides, d_{xy} hole-like dispersion which is well separated from other dispersions demonstrates a back-folding which is an attribute of the gap opening (see 6.2 K plot in Fig.5.2). Already from visual inspection, it is seen that the largest superconducting gap is on the small hole pocket, the next in magnitude is the gap on the inner electron pocket, and the smallest gap is on the large hole pocket. The inset in Fig.5.2 shows a zoomed-in region of the spectrum where the smallest gap is located. This plot is another piece of evidence that the resolution is good.
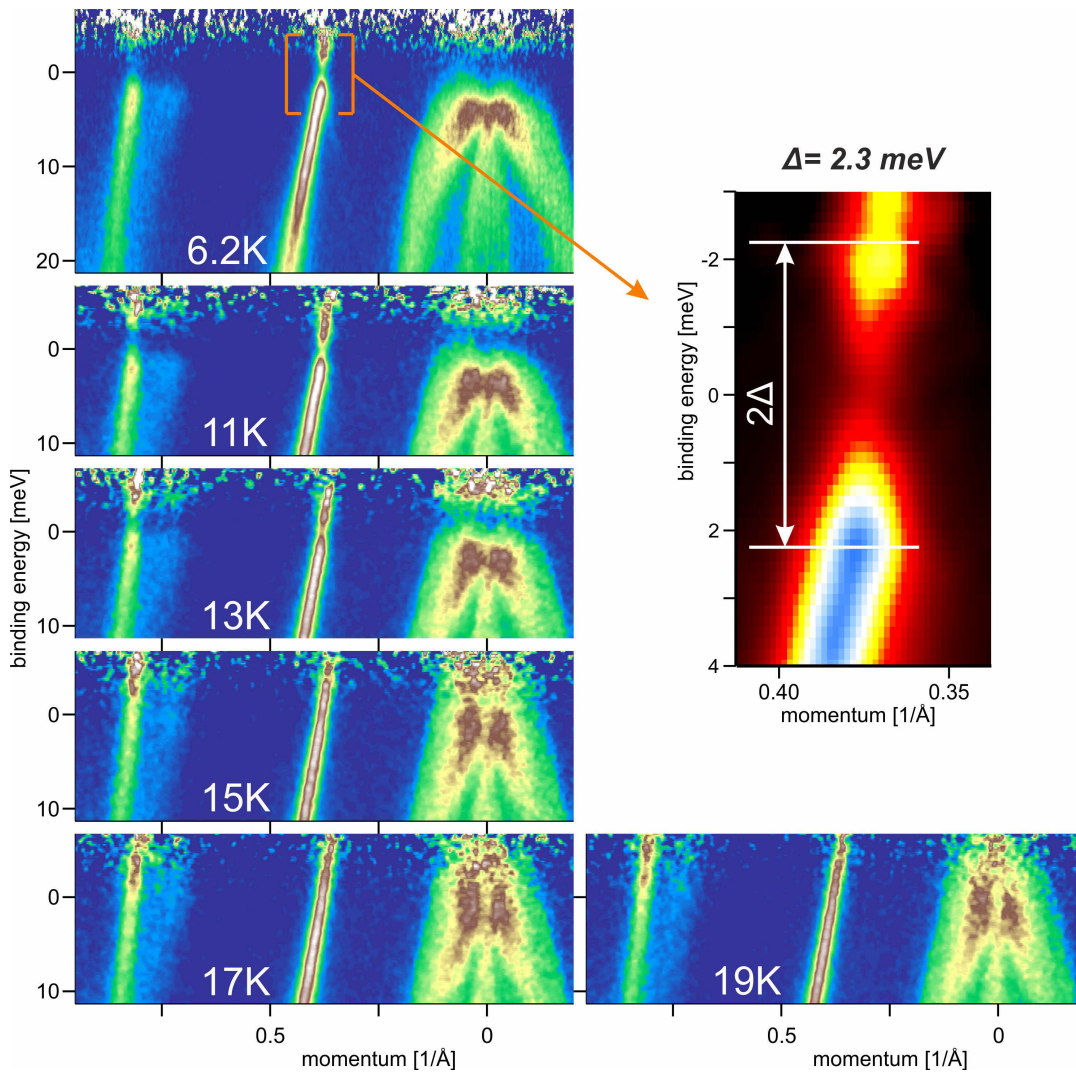

FIGURE 5.2: Intensity plots which show temperature evolution of the spectrum in Fig.5.1(b). Here, all spectra are divided by the Fermi function to enhance the signal from stats above the Fermi level. (inset) A zoomed-in region of the 6 K spectrum where the smallest gap is located.

For extracting magnitudes of these gaps we analyzed EDCs from spectra in Fig.5.2 (not divided by Fermy function). Fig.5.3 shows EDCs obtained from k_F for d_{xy} hole-like dispersion (the one which forms the larger pocket), d_{xy} electron-like dispersion (the one, which forms the inner pocket) and d_{xz} hole-like dispersion (the one, which forms the small pocket). EDC for d_{xy} hole-like dispersion was obtained from the 6K spectrum. Two other EDCs were obtained from the 11K spectrum[2]. For all EDCs the presence of the second coherent peak can be seen. For EDC obtained from d_{xz} hole-like dispersion this peak is more distant from the Fermi level and because of this is more suppressed and appears as a shoulder. For d_{xy} electron-like dispersion the second coherence peak is the most pronounced one, and we can easily extract a distance between coherent peaks. It is about 5 meV, but this distance is smaller than the real doubled gap size because the shape of the second peak is heavily distorted by the Fermi function. In order to extract the real gap size, one should fit this EDC with a function, which includes the influence of the Fermi function. We fit EDCs with a function which consists of a constant background and two peaks multiplied by the Fermi function. Both peaks are Voigt profiles (convolution of a Lorentz profile and a Gaussian profile) with the same shape and size. They are located at equal distances from the Fermi level. The fitting function is the following:

$$I(\varepsilon) = I_0 + \big(I_1 + V(\varepsilon - E_F - \Delta, A, W, S) + V(\varepsilon - E_F + \Delta, A, W, S) \big) F(\varepsilon, E_F, T),$$

where $F(\varepsilon, E_F, T) = \big(1 + exp\frac{\varepsilon - E_F}{kT}\big)^{-1}$ is the Fermi function and $V(x, A, W, S)$ is a Voigt profile. Here, ε is binding energy; A, W and S are numbers which represent the area, width, and ratio of Lorentz and Gaussian components of Voigt profile respectively; E_F is the Fermi level position; Δ is SC gap size; T is temperature; k is Boltzmann constant. The term $I_0 + I_1 F(\varepsilon, E_F, T)$ represents a background. For the fitting I_0, I_1, E_F, Δ, A, W, S, T are fit coefficients and ε is an independent variable. During the fitting coefficient I_1 was hold on a value which was estimated from part of the spectrum without bands. Changing of this coefficient in a reasonable range can only make negligible changes in the fitting results. So, holding of I_1 should not cause inaccuracy in the gap size determination, and we can treat data in this way. Despite there is no clear second coherence peak in EDC obtained from d_{xz} hole-like dispersion but only the shoulder, the gap still can be extracted from the fitting procedure. Results of fitting these EDCs with our function are given in Table. 5.1.

---

[2]The gap on these pockets is big which means the second coherence peaks is distinct from the Fermi level and as consequence it is too weak in 6 K spectrum.
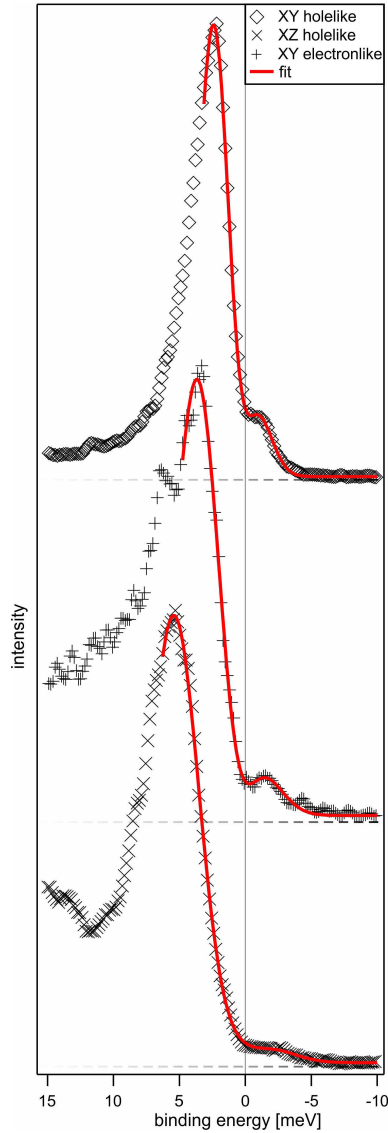
FIGURE 5.3: EDCs obtained from k_F for d_{xy} hole-like dispersion, d_{xy} electron-like dispersion and d_{xz} hole-like dispersion. Results of fitting these EDCs whith our 2-peak function are shown with red curves. There is one more peak in EDC taken through d_{xy} electron-like dispersion at ~ 6.5 meV. This peak originated from the d_{xz} electron-like dispersion (one which forms the outer pocket).

5.1.1 Superconducting gap anisotropy on the hole Fermi surfaces

In order to determine the anisotropy of the superconducting gap on different Fermi surfaces we have measured detailed data sets. Let us start form consideration of hole pockets at the center of the BZ. The high-resolution map of these pockets is shown in Fig. 5.4(a). This map was obtained from a data-set which was measured with 25 eV photons (approximately corresponds to Γ point) under special geometry in which an angle between the analyzer slit and $\Gamma - M$ direction is $\pi/8$. In such experimental geometry, the d_{xy}-states are not critically suppressed along any direction in the k-space and all parts of the large hole pocket can be seen. While in the case of zero angle (see Fig.5.1(a) and Fig.5.5(a)), parts of this pocket which point to electron pockets are dramatically suppressed. Also, we face a similar problem if measure

Band	Gap size
d_{xy} hole-like	2.30±0.07 meV
d_{xy} electron-like	3.57±0.03 meV
d_{xz} hole-like	5.41±0.10 meV

TABLE 5.1: Magnitude of the gap on different pockets obtained by EDC fitting.

under geometry in which an angle between the analyzer slit and $\Gamma - M$ direction is $\pi/4$. This makes the data set measured under our experimental geometry the most suitable for the gap extraction from the EDC-lineshape. However, even in this data set, the intensity is not equal for different parts of the pocket as well, but this does not change the EDC lineshape, and there is still enough intensity for the EDC lineshape analysis in all the parts. Intensity plot in Fig.5.4(c) represents k_f-EDCs obtained from all parts of large hole pocket with 5° step. Some of these EDCs are also shown in Fig.5.4(d) as curves which are more common and easily understood. This set of EDCs clearly shows the presence of the superconducting gap anisotropy on this pocket. Both, a coherent peak and a leading-edge position of the EDCs periodically vary with the direction and have two minima and two maxima. For numerical estimation of the gap anisotropy, we extracted the leading-edge position from these EDCs. The result is presented in Fig.5.4(e). It shows the gaps magnitude as a function of the angle along the Fermi surfaces. Here, an angle is counted anticlockwise from k_y direction. It is distinctly seen from this graph, that the gap function has C_2 symmetry, which is in contrast with previous ARPES studies of LiFeAs [175, 113] wher the gap with C_4 symmetry was observed on this pocket. The amplitude of the observed gap oscillations is considerable and well above the error bars. Fitting of this result with a periodic function gives 0.9 meV difference between maximal and minimal gap size.

We have also analyzed the leading edge gap anisotropy on the large d_{xy} hole pocket from another data set measured on a different sample under different experimental geometry with different photon energy (18 eV, which approximately corresponds to Z point). Fig.5.5(a) shows the Fermi surface map obtained from this data set, and Fig.5.5(b) shows leading edge position extracted from k_f-EDCs obtained from this data set as a function of angle. Anisotropy of the leading edge position is clearly seen from this plot, which indicates anisotropy of the superconducting gap. This result is consistent with C_2 and cannot be explained in terms of C_4 symmetry. An amplitude of the oscillations is very similar to the one extracted from 25 eV data set. This
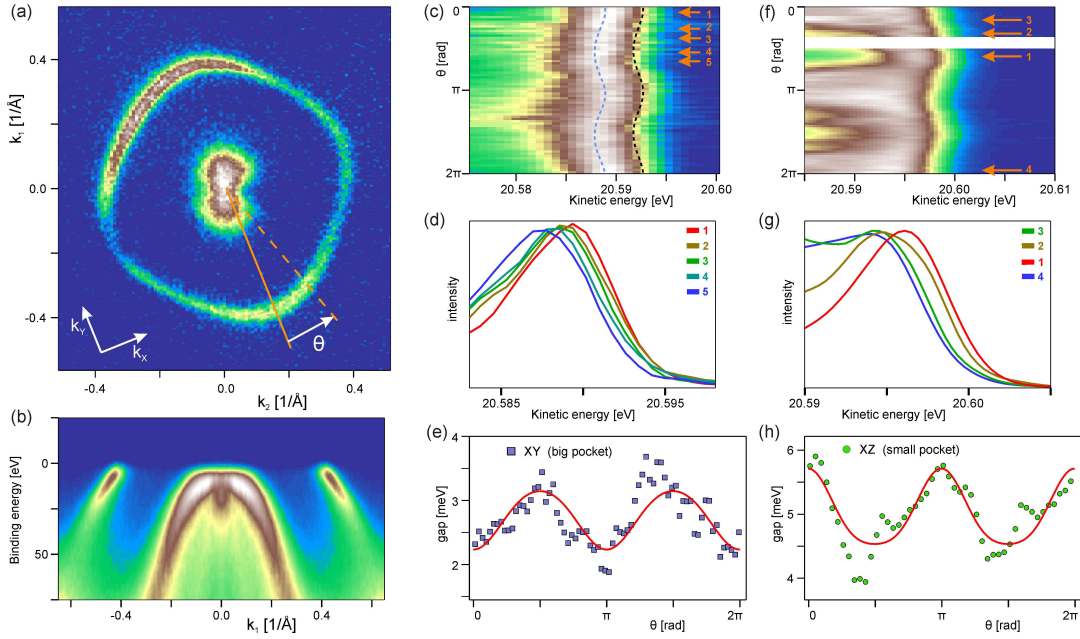
FIGURE 5.4: (a) Fermi surface map of the center of the BZ measured in the superconducting state with 25 eV photons. (b) Spectrum measured through the center of the BZ under the same conditions as map in (a). (c) Intensity plot which represents k_f-EDCs obtained around large hole pocket. Here the angle is counted anticlockwise from k_y direction. (d) EDCs from (c) according arrows. (e) Gap function of the large hole-pocket extracted from linesape of EDCs in (c). Red represents a result of the fit. (f) - (h) the same as (c) - (e) but for small hole pocket.

confirms our findings.

Now let us consider the superconducting gap on the small d_{xz} hole pocket. For this we also analyzed 25 eV data set. Actually, at this k_z, which is near Γ-point, d_{xz} dispersion does not cross the Fermi level (see Fig.5.4(b) and Fig.5.7(b)). However, it goes close enough to the Fermi level, and its top "feels" the gap. We have analyzed this pocket in the same way: obtained a set of EDCs around the pocket (see Fig.5.4(f, g)) and extracted the leading edge position from them. The gaps magnitude variation extracted in this way is shown in Fig.5.4(h). It clearly shows that the gap on this pocket also has C_2 and is in anti-phase with the one on the large hole pocket.

5.1.2 Superconducting gap anisotropy on the electron Fermi surfaces

Now let us turn to the electron Fermi surfaces near the corner of the BZ. Fig.5.6(a, c) shows the high-resolution maps of these pockets taken using 25 eV and 23 eV photons, respectively. At a first glance, these maps consist of
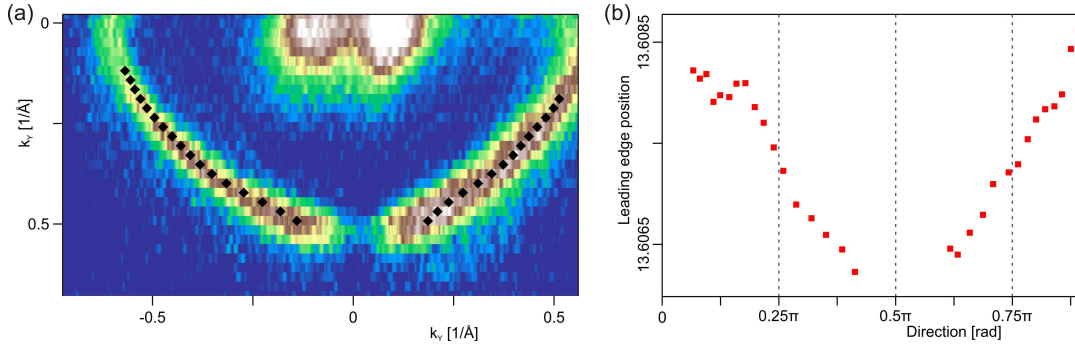
FIGURE 5.5: (a) Fermi surface measured in the superconducting state using 18 eV photons. (b) Leading edge positions of the k_f-EDCs from parts of the map marked on the map with the black dots.

two crossed ellipses. However, from the earlier study [8] we know, that electron pockets hybridize along the lines, which connect them, because of the spin-orbit interaction. Thus, it is better to describe this structure as inner and outer pockets. Anisotropy of the gap on the inner pocket can be seen from comparison of EDCs obtained from parts of the maps marked with crosses (see insets in Fig.5.6(b, d)). Both, a coherent peak and a leading-edge position are different for both pairs of EDCs. As well as for the hole pockets, for further analysis of the gap anisotropy on both electron pockets we extracted the leading edge position from k_f-EDCs from parts of the maps marked with red dots. The results for 25 eV and 23 eV data sets are shown in Fig.5.6(b) and (d) respectively. The outer electron pocket in Fig.5.6(a) appears blurred on the maps. This happens because of strong k_z-dispersion and low k_z resolution[3]. Because of this and low intensity of this pocket, only small parts of the pocket, where k_f can be determined with proper precision, were analyzed. In another map the outer electron pocket is more intense and larger and, as a consequence, is better distinguishable from the inner one. Thus, we were able to analyze lager portion of this pocket. Coming back to Fig.5.6(b, d)), both these plots show that the superconducting gap on both electron pockets is strongly anisotropic with C_2 symmetry. The gap on the outer pocket is slightly smaller than on the inner one and varies with the same amplitude. Such superconducting gap anisotropy on electron pockets is also in contrast with previous ARPES studies of LiFeAs [175, 113].

---

[3]As it was mentioned in section 2.2, k_z resolution is better than it was expected, but still considerably lower than in-plane momentum resolution.
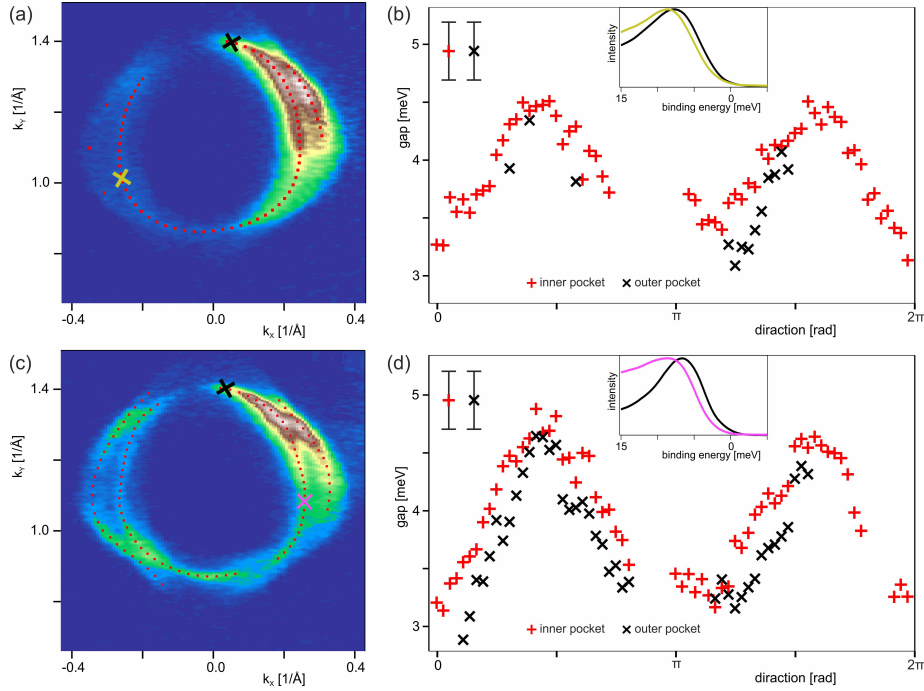
FIGURE 5.6: (a) and (c) Fermi surface map of electron pockets measured with 25 eV and 23 eV photons respectively. (b) and (d) gap functions on the inner (red markers) and outer (black markers) electron pockets extracted from data sets measured with 25 eV and 23 eV photons respectively. Here, the angle is counted anticlockwise from k_y direction. Insets show k_F-EDCs from the points on the maps marked by the crosses of the same color.

5.2 Nematicity

It was believed that LiFeAs is a perfect C_4 symmetric material: none of the structural, orbital and magnetic orderings which brake the rotation symmetry were observed in it (see section 1.2). However, in the previous section, we show that the superconducting gap has C_2 symmetry on all Fermi surface sheets of LiFeAs. Such gap symmetry is not expected in a perfect C_4 material. This motivated us to reexamine the electronic structure of LiFeAs and find out whether it is relay C_4 symmetric. In this section, we present the results of this investigation.

Let us start from hole pockets in the center of the BZ. Intensity plots in Fig.5.7(b) represent cuts through hole pockets obtained in directions shown with dashed lines on the map in Fig.5.7(a) (these directions are orthogonal to each other and coincide with high-symmetry directions). Comparison of the MDC obtained from these at the Fermi level (see insets in Fig.5.7(b)) show that the large hole-like pocket is anisotropic. Specifically, the peaks of the lower curve are more spread than the peaks of the upper one, which means

that the pocket is elongated in the k_y-direction. Furthermore, this deformation is observed not only at the Fermi level. To show this, we extracted the position of the MDC maxima at different binding energies from both cuts and plotted the result in Fig.5.7(c). This plot shows that the deformation persists to all binding energies. In order to describe the deformation numerically, we define a deformation coefficient as $D = 2\frac{L_y - L_x}{L_y + L_x}$, where L_y and L_x are the pocket sizes (distances between MDC peaks) in k_x and k_y directions, respectively. The average value of the deformation coefficient for the d_{xy} dispersions in the analyzed range of binding energies is 4 % (see insets in Fig.5.7(c))

A similar deformation we also observe for outer (d_{xz}) and inner (d_{yz}) hole-like dispersions. Fig.5.8(a) shows k_x and k_y cuts taken through the center of the bands. Since the tops of these dispersions are close to each other, and the Fermi level, the precise extraction of positions of all four MDC components at low binding energies is complicated. Because of this, we extracted the deformation of these dispersions at higher binding energies. Fig.5.8(a) shows L_x and L_y for both the inner and outer dispersions as a function of the binding energy. One can see from these data that for the outer dispersion where such distances are of the order of 0.35-0.55 Å^{-1}, the L_x (red curve) is larger than L_y (blue curve), while for the inner dispersion the effect is opposite sign: L_y is larger than L_x. Fig.5.8(a) shows the magnitude of the deformation coefficient for these dispersions as a function of the binding energy. The average value of the deformation coefficients for the inner and outer dispersions are 7.0% and -2.4%, respectively. Since for the inner dispersion, the distance between the MDC maxima is smaller, the error bars of the deformation resulting from the two subtractions of the dispersions are larger. Nevertheless, averaging over the energy indicates the presence of the effect.

Now, we consider a temperature evolution of the effect. Fig.5.7(d) demonstrates shapes of the d_{xy} dispersion extracted from k_y cuts taken from data sets measured on the same sample but at different temperatures. Light-blue curves represent 7K (superconducting state) data set and red curves represent 23K (normal state) data set. The difference in the shape of these dispersions cannot be reconciled entirely with the gap opening. Usually, the gap opening results in the so-called S-shaped dispersion, which going towards the Fermi level first slows down after then strongly accelerates crosses Fermi level at the same momentum as it did in the normal state, thus showing no change of the Fermi surface size or shape (for details see Ref.[192, 193]). Blue curves which represent the superconducting state does not show S-shape,
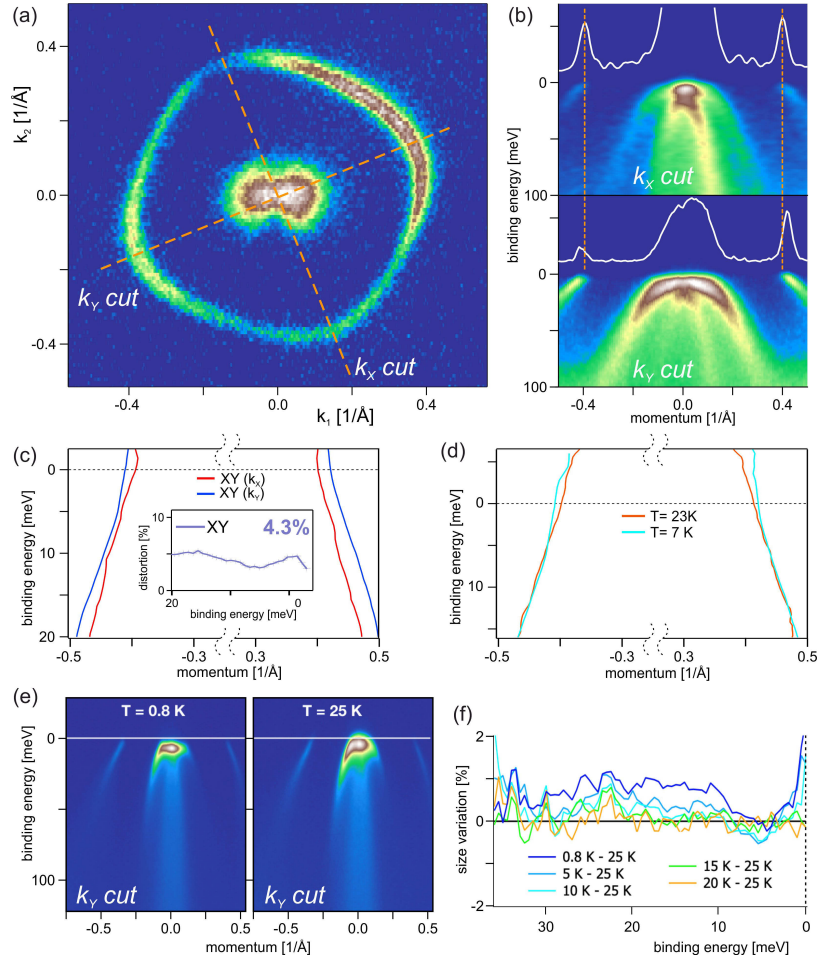
FIGURE 5.7: (a) Fermi surface map of the center of the BZ (the same as Fig. 5.4(a)). (b) Intensity distributions along the k_x and k_y cuts (directions of the cuts are shown with dashed lines on the map). White curves represent E_F-MDCs. (c) Dispersions corresponding to d_{xy} hole pocket extracted from the k_x and k_y cuts. The inset represents the behavior of the deformation coefficient. (d) Dispersions corresponding to d_{xy} hole pocket extracted in k_y direction from the data sets measured at 7 K and 23 K. (e) Spectra taken in k_y direction with 35 eV photons at 0.8 K and 25 K. (f) Size variation caused by temperature, calculated by subtracting the red curve (25 K) from all others and dividing the result by the average value, similar to deformation coefficient.

but it demonstrates repulsion of the dispersion (blue curves are wider spread than red curves), which makes pocket longer in k_y direction in the superconducting state. This implies that the deformation is interconnected with the superconductivity.

We have also performed a more detail analysis of the temperature evolution of d_{xy} distension on another sample. For this sample, six spectra at different temperatures from 0.8K to 25K were measured along k_y direction (two of them are shown in Fig. 5.7(e)). We extracted the dispersion shape from all these spectra by tracking MDC peaks positions. Then we obtain the value which characterize changes in the dispersion shape in comparison to the normal state dispersion (at 25K): $D_T = 2\frac{L_y - L_{yNorm}}{L_y + L_{yNorm}}$, where L_{yNorm} is value L_y for the normal state. We plotted this value as a function of binding energy for different temperature in Fig.5.7(f). It shows that the deformation is the largest at the lowest temperature and decreases with temperature increasing. The orange curve which represents a difference between dispersions at 20 K and 25 K does not significantly deviate from zero in the full energy range signaling the absence of any change in the dispersion as a function of temperature in the normal state. Also one can see another effect: in a small range of binding energies (from 3 to 8 meV) near the gap value no considerable deformation is observed at any temperature. This is because in this region the described above effect competes with developing of S-shape dispersion caused by the gap opening.

Another piece of evidence of the interconnection between the deformation and superconductivity comes from a temperature evolution of the deformation of d_{xz} and d_{yz} dispersions. We provide a similar analysis of the shape of these dispersions for high-temperature data set as for the low-temperature one. Results of this analysis (see Fig.5.8(c, d, f)) show that the deformation disappears in the normal state: the average values of the deformation coefficients are equal to zero for both inner and outer pockets within error bars.

Besides, we have observed breaking of the rotational symmetry in the shape of the electron pockets. Fig.5.9 demonstrates the results of the analysis of the same two data sets measured with 25 eV and 23 eV from which we expected the gap anisotropy. We start the analysis from a comparison of E_F MDCs in Fig.5.9(c, d) which were obtained from these data sets in k_x and k_y directions (see dashed lines on the maps in Fig.5.9(a, b)). Both of these pairs of MDCs show that the inner pocket is longer along k_y direction. similar to for hole pockets, the deformation is present not only near the Fermi level but persists to higher binding energies. This is demonstrated in Fig.5.9(e) which
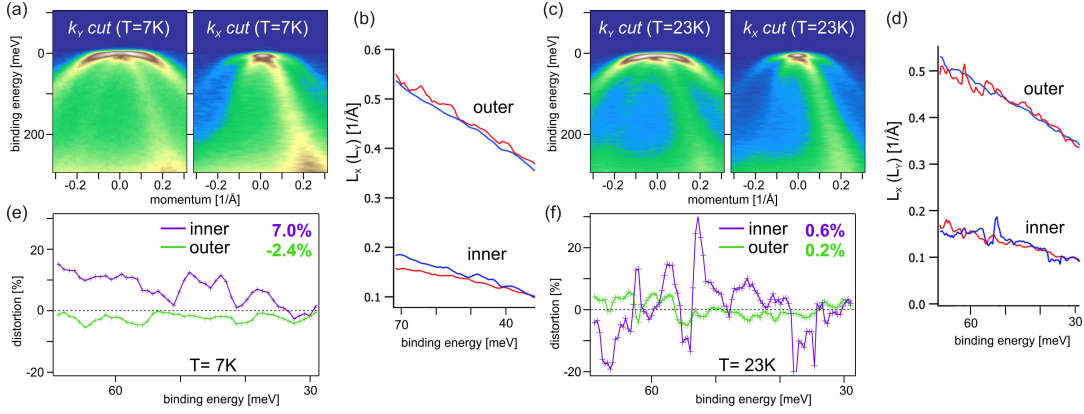
FIGURE 5.8: Intensity distributions along the k_x and k_y cuts obtained from the data set measured at 7 K. (b) Distances between the dispersions extracted from the cuts in (a). Blue and red curves correspond to k_x and k_y directions, respectively. (e) Deformation coefficient for the inner and outer hole-like pockets. (c), (d), and (f) the same as (a), (b), and (e) but for the data set measured at 23 K.

represents a shape of the desperation which forms the inner pocket extracted from the 23 eV data set in k_x and k_y directions. The average value of the deformation coefficient is 3.6% (see the inset in Fig.5.9(e)). We are not able to determine a deformation of the outer electron pocket because the intensity of the dispersion which forms this pocket in k_y direction is too low to be analyzed.

Fig.5.10 demonstrates the results of the analysis of another data set which was measured on another sample using 21 eV photons. This data set again demonstrate a differences in the shape of the dispersion (the one, which forms the inner pocket) between k_x and k_y directions. However, this difference is of opposite sign (see Fig.5.9(c)). We will discuss possible interpretations of this result later. In Fig.5.10(d, e) we present the temperature dependence of the dispersions obtained from both cuts. Since in this data set the pockets are better separated, it is possible also to extract the d_{xy} dispersion which supports the outer pocket in k_x direction, but in k_y direction it is still too weak. From Fig.5.10(d) one can see that the size of the both pockets along k_x becomes smaller upon temperature unceasing, it is even better seen from the inset which shows D_T for these dispersions. Along k_x (Fig.5.10(e)) no changes were detected. This result confirms, that deformation tends to disappear with temperature increasing.
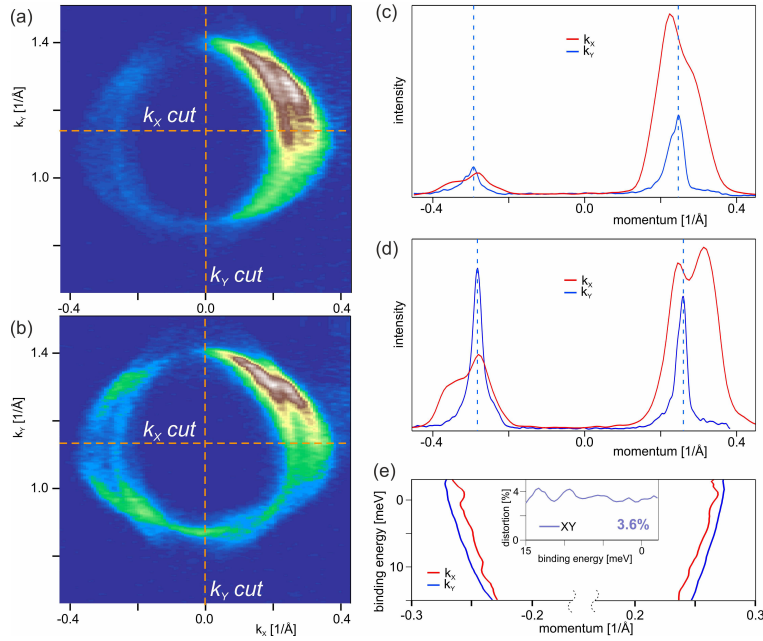
FIGURE 5.9: (a) and (b) Fermi surface map of electron pockets measured with 25 eV and 23 eV photons, respectively (the same as in Fig. 5.6). (c) and (d) E_F MDCs obtained in k_x and k_y directions from the maps in (a) and (b), respectively. (e) Dispersions which form the inner electron pocket in k_x and k_y directions obtained from 23 eV data set. Inset shows the deformation coefficient.

5.3 Discussion and conclusions

Fig. 5.11 summarize the results of this chapter. It represents the observed deformations of the Fermi surface and the superconducting gap anisotropy. A sketch in Fig. 5.11(a) schematically shows the Fermi surface of LiFeAs in the normal state is given in Fig. 5.11(a). The orbital character of the Fermi surface sheets is depicted with black letters on the plot. At $k_z = 0$, there is no small d_{xz}/d_{yz} hole pocket because the dispersions which form this pocket at other k_zs runs close to the Fermi level but does not cross it at this k_z value. Fig. 5.11(b) corresponds to the superconducting state. Here, shapes of the contours represent the shape of the Fermi surface, and the contours' thickness represents the gap magnitude on corresponding parts of the Fermi surface. The thicker parts correspond to the larger gap. To underline the directions of the Fermi surface deformations, we added arrows on the plot. Question marks indicate parts where deformation was not determined. The possible reason for different signs of the deformation of electron pockets at $k_z = 0$ and $k_z = \pi$ is the additional in-plane interaction channel which is present at $k_z = \pi$ were d_{xz}/d_{yz} dispersions form small hole Fermi surface and absent at $k_z = 0$ where this Fermi surface is absent. However, taking in to account the
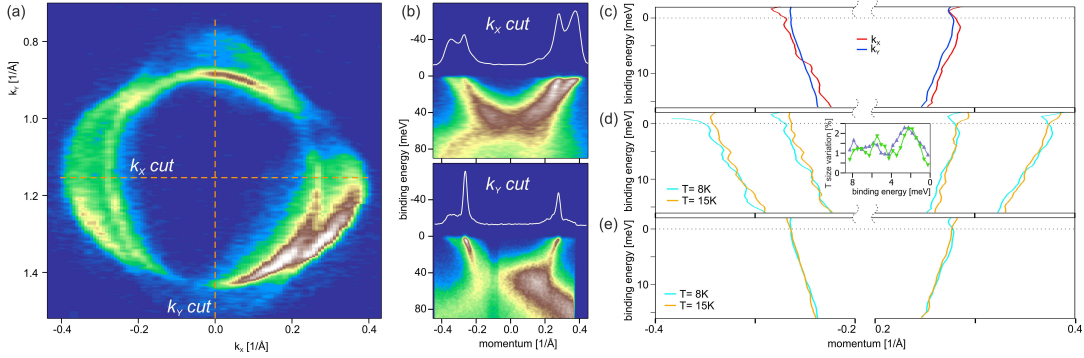
FIGURE 5.10: (a) Fermi surface map of electron pockets measured with 21 eV photons at 8 K. (b) Intensity distribution along k_x- and k_z-cuts obtained from the same data set as (a). White curves represent E_F MDCs. (c) Dispersions which form the inner electron pocket in k_x and k_y. (d) Dispersions extracted in k_x direction from the data sets measured at 8 K and 15 K. (e) Dispersions extracted in k_y direction from the data sets measured at 8 K and 15 K. No matching of the zero position has been done in (c-e).

fact that the results for $k_z = \pi$ where obtained from another sample, we cannot exclude that the sign is different because of another preferable domain orientation in this sample. While the detailed k_z-dependence of the observed effects still needs to be refined, calling for further, even more thorough experimental studies, Fig. 5.11 provides an overview of a spontaneous rotational symmetry breaking in the superconducting state of LiFeAs.

A possible reason why in previous ARPES studies of the gap anisotropy in LiFeAs [85, 113] the four-fold symmetric gap had been observed is thous in that studies superposition of several domains was measured which is typical for ARPES, because of the finite size of the beam spot. While in our present study a signal from one domain orientation is dominating (this follows from the presence of only one set of deformed Fermi surface pockets at low temperatures). A posseble reason for this could be a small detwinning force due to the glue, cleavage, cooling, etc. This force makes one domain orientation more preferable than the other one. However, this force is not strong enough to noticeably change the electronic structure itself (this follows from the absence of the Fermi surface deformation at high temperatures). Also, in earlier ARPES studies the data quality is lower, and only some parts of the pockets are analyzed. Regarding QPI studies, most of the results were obtained by using C_4 symmetrization procedure, since the gap symmetry different from C_4 was not expected.
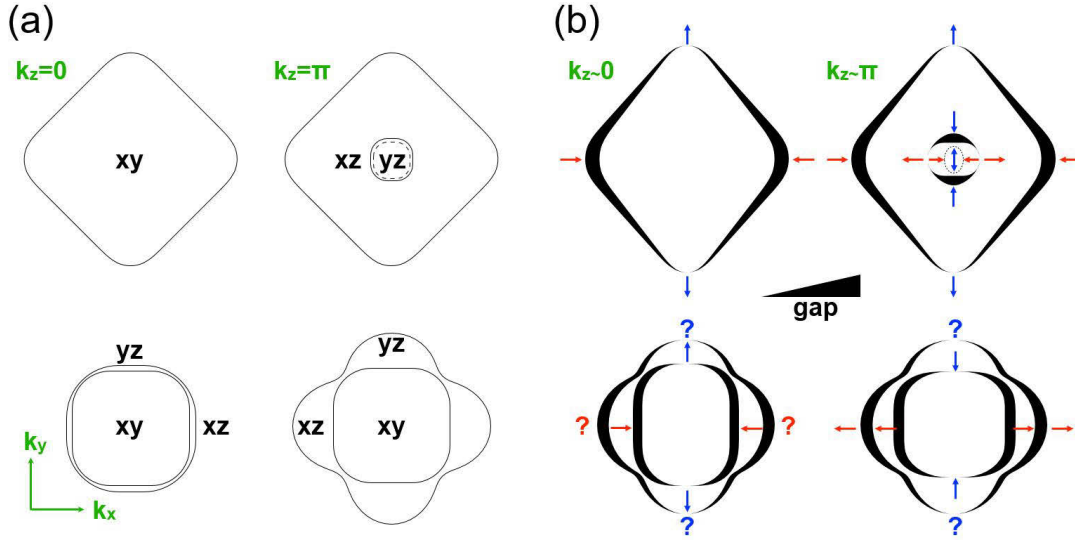
FIGURE 5.11: (a) Schematic representation of the Fermi surface shape of LiFeAs in the normal state. Dashed contour represents the d_{yz}/d_{xz} dispersion which do not cross the Fermi level. (b) Sketch which qualitatively shows the changes of of the Fermi surface shape at low temperatures and the gap anisotropies. The gap magnitude variation is shown by the modulation of the contours' thickness.

5.3.1   Theoretical interpretation

The $\cos 2\theta$ variation of the gap (four-fold symmetry) along this pocket d_{xy} hole pocket together with an absence of the gap nodes on this pocket indicate that the superconducting gap in LiFeAs has both $s-$wave and $d-$wave components. Such behavior is indeed expected for a system with broken C_4 symmetry. In such a case, developing one pairing component can act as a field for the other component, and, as a result, both are present.

As has been shown, the electronic structure of LiFeAs is different from those of other IBS. Its Fermi surface has cylindrical sheets, which exist for all k_z values, such pockets are the two electron pockets and the large d_{xy} hole pocket, centered at $k_x = \pm\pi$ $k_y = \pm\pi$ in 1-Fe BZ, and small d_{xz}/d_{yz} hole pocket, centered at $k_x = k_y = 0$ which exists only around $k_z = \pi$. In such electronic structure, a number of pairing states possibly can be realized. It can be a conventional s^{+-} with sign change between all hole and all electron pockets, orbitally antiphase s^{+-} with sign change between two hole pockets, as well as several $d-$wave gap structures. Our ARPES results show that at T = 23K which is slightly above critical temperature C_4 symmetry still is preserved, while deep inside the superconducting state (at 7K) rotational symmetry is broken showing a nematic order. The theoretical explanation for this result was developed by A. Chubukov and described in Ref.[194].

According to this explanation, the $s-$ wave which develops at T_c induces instability which leads to the C_4 symmetry breaking and, as a consequence, the appearance of the $d-$wave component of the gap.

5.3.2 Conclusions

We demonstrated spontaneous breaking of the rotational symmetry in the superconducting state of LiFeAs. It manifests in two-fold symmetry of the superconducting gap and unidirectional distortion of the Fermi surface which is observed in the superconducting state but not in the normal state. Both these effects were observed on all hole and electron sheets of the Fermi surface. These results demonstrate the realization of a novel phenomenon of superconductivity-induced nematicity.

Summary

In this thesis, we analyze the electronic structure of two members of the family of Fe-based superconductors: FeSe and LiFeAs. These pristine materials can superconduct without any doping, which makes them different from other Fe-based superconductors. Also, these materials do not exhibit a magnetic ordering typical for underdoped superconductors and their parent compounds. Concerning nematicity, it has been observed in FeSe by various experimental techniques but it has not been observed in LiFeAs before our study.

It used to be believed that, in FeSe nematicity causes large (more than 50 meV) splitting of the dispersions near the corner of the BZ. In our study, we have shown that both dispersions, which were associated with the presence of two domain in the orthorhombic phase, are present in the tetragonal phase as well. Also, their existence is predicted by a band structure calculations. The further low-temperature measurements reveal an additional splitting of both of these dispersions. This indicates that nematicity indeed influences the electronic structure near the corner of the BZ, but the scale of the changes are not so big ($\sim$ 15 meV). Changes in the electronic structure near the center of the BZ have the same scale. The electronic structure calculations which take in to account the lattice deformation in the orthorhombic phase are in good agreement with the experimental results for the corner of the BZ but do not predict a considerable splitting near the center of the BZ which is observed in the experiment. This discrepancy indicates that the nematic transition is not phonon-driven but has an electronic origin. FeSe is not only one material where an influence of nematicity was overestimated, e.g., another our study [43] reveals that in Ba122, a scale of the changes caused by nematicity is $\sim$ 20 meV in contrast to $\sim$ 70 meV in earlier studies.

Besides rapid changes of the electronic structure of FeSe around 87K, related to a nematic transition, we have observed another temperature dependent effect: the dispersions located near the center of the BZ shift up with temperature increasing when the dispersions located near the corner of the BZ shift down. These shifts are observed in both orthorhombic and tetragonal phases. These changes tend to decrease the size of the "red-blue" shift.

The comparison of a temperature behavior of the shifts with those for existing theories, which describe the red-blue shift, shows an immediate agreement neither with Pomeranchuk nor with spin fluctuation scenario. Both suggested by us order parameters of the effect demonstrate almost linear behavior, which is not expected in the spin fluctuation scenario. In the framework of the Pomeranchuk scenario, our results imply an extremely high onset temperature of the Pomeranchuk instability, which is also unlikely. To quantitatively explan our experimental results more theoretical investigations are needed.

Concerning the superconducting gap in FeSe, our ARPES measurements show that it is strongly anisotropic but nodeless on hole Fermi surface as well as on electron Fermi surfaces. These results are in agreement with the results of the QPI study. Such gap anisotropy can be explained with orbital-selective Cooper pairing. Another explanation for it is a mixing of s-wave and d-wave pairing channels caused by nematicity.

The detection of the breaking of C4 rotational symmetry in LiFeAs was a real wonder for us. However, the facts presented below made us to believe in this. The breaking of the rotational symmetry has been detected in both, the Fermi surface shape and the superconducting gap symmetry. The unidirectional deformation of the Fermi surface and underlying dispersions was observed for nearly all Fermi surface sheets on several samples. Moreover, the sign of the deformation is not equal for all Fermi surface sheets. Such deformations are present in the superconducting state and disappears in the normal state. This is an uncommon behavior, since most Fe-based superconductors undergo nematic transitions at temperatures higher than temperatures of superconducting transition. To explain this phenomenon, a concept of superconductivity-induced nematicity was suggested. In this concept, the gap with $s-$ wave symmetry which develops in the superconducting state induces instability which leads to the rotational symmetry breaking and, as a consequence, the appearance of the $d-$wave component of the gap. Observation of such an unusual phenomenon in LiFeAs call for further studies of this material with other experimental techniques.

I hope, our results will help to solve one of the biggest miseries in solid-state physics and bring closer an era of really high-temperature superconductors.

Appendix A

Fitting a pocket shape with peanut-like contour
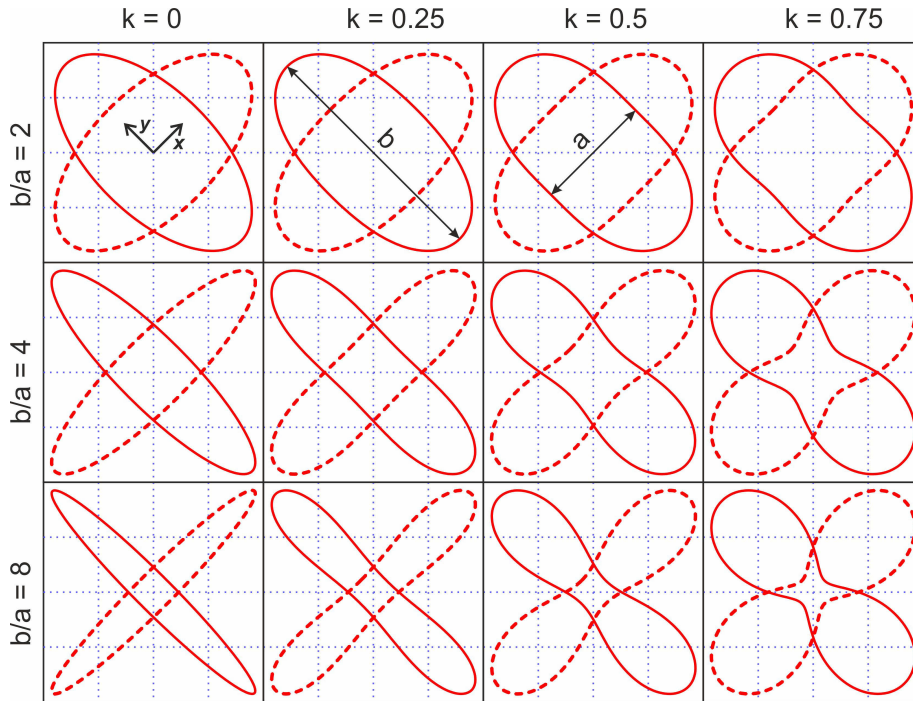
FIGURE A.1: Examples of the shapes described by equation A.1 for different parameter values (solid contour). The dashed contour has the same shape but rotated by $\pi/2$.

For describing the shape of electron pockets on the Fermi surface of FeSe we used a contour which is defined by following parametric equations of x and y:

$$x = \left(a + k(b-a)sin^2(t)\right) * cos(t)$$
$$y = \left(b - k(b-a)cos^2(t)\right) * sin(t) \tag{A.1}$$
$$\text{for } 0 \leq t < 2\pi$$

Here $a > 0$ and $b > 0$ are dimensions of the contour along its sort and long axis respectively and $0 \leq k \leq 1$ is a parameter which describes deviation from the elliptical shape. Several examples of such contour for different parameter values are shown in Fig.A.1. If $k = 0$ the contour is perfect elliptical, at high k its shape becomes similar to peanut.

For proper fitting electron pockets observed in ARPES one should take into account nematicity and presence of domains. Nematicity results in difference in shapes of two orthogonal peanuts. Presence of two different domains orientations leads to overlapping signals from them and as a consequence adding a second pair of peanuts which is the same as a first one but rotated by $\pi/2$. Because of this, for fitting electron pockets we used four peanut contours (see Fig.A.2) one pair of equal orthogonal peanuts for shorter contours and another pair for longer ones.
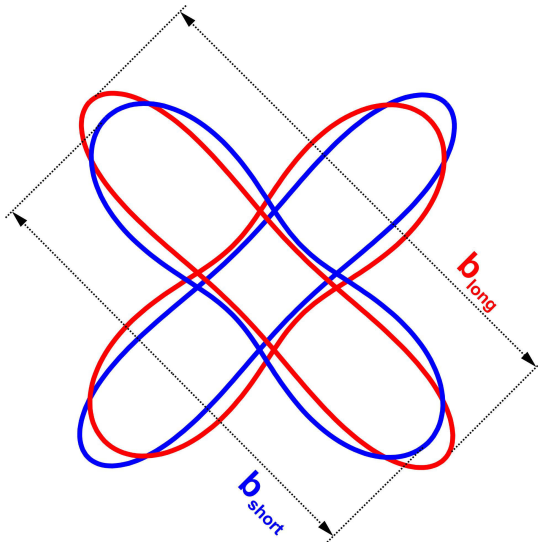

FIGURE A.2: The results of fitting of four peanuts on the experimental Fermi surface. Here different colors represent different domains.

Appendix B

Extraction of the superconducting gap

The most common way to extract the gap from ARPES results is symmetrization. In this method, one extracts a distance between peaks of a symmetrized k_F-EDC. This distance is interpreted as double size of the. In most cases this method provides reliable results. However, in case of a small gap (or bad experimental resolution) when it is smaller then the experimental resolution the peaks can be considerably shifted, or even the symmetrized curve can become gapless as it is shown with simulations [195] (see the third column on Fig.B.1). Another factor which can influence on the peak position is a proximity of other dispersions[1]. Because of a finite energy width of the neighbor dispersions, there "tails" can visually shift the coherent peek.

All these issues are inherent for IBS which have a complicated electronic structure where bands have neighbors in close vicinity of them (especially in the nematic phase), and the gaps are relatively small. Thus, extraction of the gap size on the electron pockets of FeSe by symmetrization of the ARPES results failed [149]: no gap was observed.

Because of this, we use a shift of EDC leading edge [196] between the normal and the superconducting state as a measure of the gap size. We determine the leading edge position as a position of the highest absolute value of the EDC's derivative. For this we took the EDC derivative and fitted the region near its minimum with Gauss profile with no background. The simulations [195] show that this method in case of a small gap is less sensitive to the experimental resolution (see the fourth column on Fig.B.1). Moreover,

---

[1]It can be a real neighbor dispersion as well as a dispersion originated from another domain of the sample in the nematic phase.

the leading edge is more distant from neighbor dispersions which can lay below[2] the analyzed dispersion than the coherent peak is. Therefore, the leading edge position is less sensitive to the tails of these neighbors. As a rule, a shift of EDC leading edge between the normal and the superconducting state which is also called a leading edge gap is smaller than the real gap size [196, 195]. Nevertheless, it is a good qualitative measure of the superconducting gap and can be used to estimate the gap anisotropy.
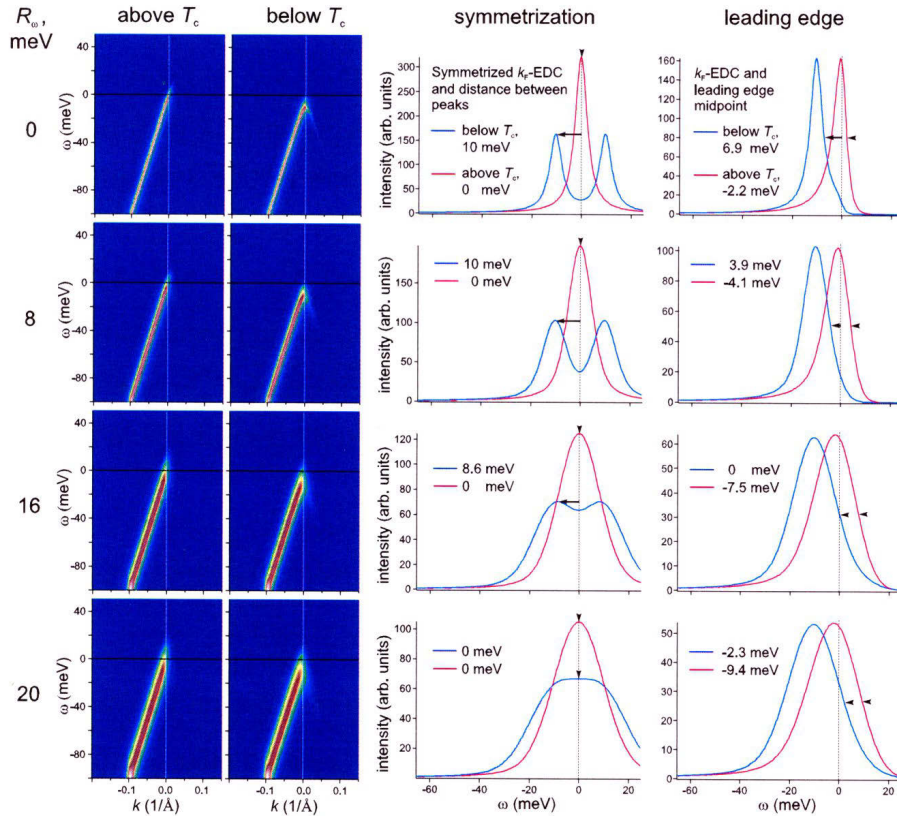
FIGURE B.1: First and second columns: ARPES spectra with one feature which crosses Fermi level simulated for different experimental resolutions for the normal and the superconducting state, respectively. Third and fourth columns: Determination of the gap with symmetrization versus leading edge, respectively. Adapted from [195]

---

[2]Neighbor dispersions which lay above the analyzed dispersion do not modify the EDC since they are suppressed by Fermi function.

Bibliography

[1] Yoichi Kamihara et al. "Iron-based layered superconductor: LaOFeP". In: *Journal of the American Chemical Society* 128.31 (2006), pp. 10012–10013.

[2] Yoichi Kamihara et al. "Iron-based layered superconductor La[O_{1-x} F_x]FeAs (x= 0.05- 0.12) with T_c= 26 K". In: *Journal of the American Chemical Society* 130.11 (2008), pp. 3296–3297.

[3] J George Bednorz and K Alex Müller. "Possible high T_c superconductivity in the Ba- La- Cu- O system". In: *Zeitschrift für Physik B Condensed Matter* 64.2 (1986), pp. 189–193.

[4] Zhi-An Ren et al. "Superconductivity and phase diagram in iron-based arsenic-oxides ReFeAsO$_{1-\delta}$ (Re= rare-earth metal) without fluorine doping". In: *EPL (Europhysics Letters)* 83.1 (2008), p. 17002.

[5] Marianne Rotter et al. "Superconductivity and crystal structures of (Ba$_{1-x}$K$_x$) Fe2As2 (x= 0 − 1)". In: *Angewandte Chemie International Edition* 47.41 (2008), pp. 7949–7952.

[6] H Okabe et al. "Pressure-induced high-T_c superconducting phase in FeSe: Correlation between anion height and T_c". In: *Physical Review B* 81.20 (2010), p. 205119.

[7] Johnpierre Paglione and Richard L Greene. "High-temperature superconductivity in iron-based materials". In: *Nature physics* 6.9 (2010), p. 645.

[8] S V Borisenko, D V Evtushinsky, Liu, et al. "Direct observation of spin-orbit coupling in iron-based superconductors". In: *Nature Physics* 12.4 (2016), pp. 311–317.

[9] II Mazin et al. "Unconventional superconductivity with a sign reversal in the order parameter of LaFeAsO$_{1-x}$F$_x$". In: *Physical Review Letters* 101.5 (2008), p. 057003.

[10] PJ Hirschfeld, MM Korshunov, and II Mazin. "Gap symmetry and structure of Fe-based superconductors". In: *Reports on Progress in Physics* 74.12 (2011), p. 124508.

[11] DV Evtushinsky et al. "High-energy electronic interaction in the 3d band of high-temperature iron-based superconductors". In: *Physical Review B* 96.6 (2017), p. 060501.

[12] A A Kordyuk et al. "Electronic band structure of ferro-pnictide super-conductors from ARPES experiment". In: *Journal of superconductivity and novel magnetism* 26.9 (2013), pp. 2837–2841.

[13] Janek Maletz et al. "Unusual band renormalization in the simplest iron-based superconductor $FeSe_{1-x}$". In: *Physical Review B* 89.22 (2014), p. 220506.

[14] SV Borisenko et al. "Superconductivity without nesting in LiFeAs". In: *Physical Review Letters* 105.6 (2010), p. 067002.

[15] AA Kordyuk et al. "Angle-resolved photoemission spectroscopy of superconducting LiFeAs: Evidence for strong electron-phonon coupling". In: *Physical Review B* 83.13 (2011), p. 134513.

[16] Laura Fanfarillo et al. "Orbital-dependent Fermi surface shrinking as a fingerprint of nematicity in FeSe". In: *Physical Review B* 94.15 (2016), p. 155138.

[17] Johannes Ferber et al. "LDA+ DMFT study of the effects of correlation in LiFeAs". In: *Physical Review B* 85.9 (2012), p. 094505.

[18] Markus Aichhorn et al. "Theoretical evidence for strong correlations and incoherent metallic state in FeSe". In: *Physical Review B* 82.6 (2010), p. 064504.

[19] Gabriel Kotliar et al. "Electronic structure calculations with dynamical mean-field theory". In: *Reviews of Modern Physics* 78.3 (2006), p. 865.

[20] V B Zabolotnyy et al. "(π, π) electronic order in iron arsenide super-conductors". In: *Nature* 457.7229 (2009), pp. 569–572.

[21] M Yi et al. "Electronic structure of the $BaFe_2As_2$ family of iron-pnictide superconductors". In: *Physical Review B* 80.2 (2009), p. 024515.

[22] V Brouet et al. "Large temperature dependence of the number of carriers in Co-doped $BaFe_2As_2$". In: *Physical review letters* 110.16 (2013), p. 167002.

[23] Felix Lochner et al. "Electronic properties, low-energy Hamiltonian, and superconducting instabilities in $CaKFe_4As_4$". In: *Physical Review B* 96.9 (2017), p. 094521.

[24] Hui Zhai, Fa Wang, and Dung-Hai Lee. "Antiferromagnetically driven electronic correlations in iron pnictides and cuprates". In: *Physical Review B* 80.6 (2009), p. 064517.

[25] J C Séamus Davis and Dung-Hai Lee. "Concepts relating magnetic interactions, intertwined electronic orders, and strongly correlated superconductivity". In: *Proceedings of the National Academy of Sciences* 110.44 (2013), pp. 17623–17630.

[26] Andrey V Chubukov, Maxim Khodas, and Rafael M Fernandes. "Magnetism, Superconductivity, and Spontaneous Orbital Order in Iron-Based Superconductors: Which Comes First and Why?" In: *Physical Review X* 6.4 (2016), p. 041045.

[27] Rui-Qi Xing et al. "Competing instabilities, orbital ordering, and splitting of band degeneracies from a parquet renormalization group analysis of a four-pocket model for iron-based superconductors: Application to FeSe". In: *Physical Review B* 95.8 (2017), p. 085108.

[28] Laura Classen et al. "Interplay between Magnetism, Superconductivity, and Orbital Order in 5-Pocket Model for Iron-Based Superconductors: Parquet Renormalization Group Study". In: *Physical Review Letters* 118.3 (2017), p. 037001.

[29] Luciano Ortenzi et al. "Fermi-surface shrinking and interband coupling in iron-based pnictides". In: *Physical review letters* 103.4 (2009), p. 046404.

[30] L Benfatto and E Cappelluti. "Effects of the Fermi-surface shrinking on the optical sum rule in pnictides". In: *Physical Review B* 83.10 (2011), p. 104516.

[31] Y Zhang et al. "Nodeless superconducting gap in $A_x Fe_2 Se_2$ (A= K, Cs) revealed by angle-resolved photoemission spectroscopy". In: *Nature materials* 10.4 (2011), p. 273.

[32] J Maletz et al. "Photoemission and muon spin relaxation spectroscopy of the iron-based $Rb_{0.77} Fe_{1.61} Se_2$ superconductor: Crucial role of the cigar-shaped Fermi surface". In: *Physical Review B* 88.13 (2013), p. 134501.

[33] F Chen et al. "Electronic identification of the parental phases and mesoscopic phase separation of $K_x Fe_{2-y} Se_2$ superconductors". In: *Physical Review X* 1.2 (2011), p. 021020.

[34] S Nandi et al. "Anomalous suppression of the orthorhombic lattice distortion in superconducting $Ba(Fe_{1-x}Co_x)_2As_2$ single crystals". In: *Physical Review Letters* 104.5 (2010), p. 057006.

[35] Hai-Hu Wen and Shiliang Li. "Materials and novel superconductivity in iron pnictide superconductors". In: *Annu. Rev. Condens. Matter Phys.* 2.1 (2011), pp. 121–140.

[36] RM Fernandes, AV Chubukov, and J Schmalian. "What drives nematic order in iron-based superconductors?" In: *Nature Physics* 10.2 (2014), p. 97.

[37] Naoyuki Katayama et al. "Investigation of the Spin-Glass Regime between the Antiferromagnetic and Superconducting Phases in $Fe_{1+y}Se_xTe_{1-x}$". In: *Journal of the Physical Society of Japan* 79.11 (2010), p. 113702.

[38] H Luetkens et al. "The electronic phase diagram of the $LaO_{1-x}F_xFeAs$ superconductor". In: *Nature materials* 8.4 (2009), p. 305.

[39] Athena S Sefat. "Pressure effects on two superconducting iron-based families". In: *Reports on progress in physics* 74.12 (2011), p. 124502.

[40] Andrey V Chubukov and Peter J Hirschfeld. "Iron-based superconductors: seven years later". In: *Physics Today* 68 (2015), p. 46.

[41] AA Kordyuk. "Iron-based superconductors: Magnetism, superconductivity, and electronic structure". In: *Low Temperature Physics* 38.9 (2012), pp. 888–899.

[42] Matthew D Watson et al. "Three-dimensional electronic structure of the nematic and antiferromagnetic phases of NaFeAs from detwinned angle-resolved photoemission spectroscopy". In: *Physical Review B* 97.3 (2018), p. 035134.

[43] Alexander Fedorov et al. "Energy scale of nematic ordering in the parent iron-based superconductor: $BaFe_2As_2$". In: *arXiv preprint arXiv: 1811.02430* (2018).

[44] Aliaksei Charnukha et al. "High-temperature superconductivity from fine-tuning of Fermi-surface singularities in iron oxypnictides". In: *Scientific reports* 5 (2015), p. 18273.

[45] Sevda Avci et al. "Phase diagram of $Ba_{1-x}K_xFe_2As_2$". In: *Physical Review B* 85.18 (2012), p. 184507.

[46]   Samuel Lederer et al. "Enhancement of superconductivity near a nematic quantum critical point". In: *Physical review letters* 114.9 (2015), p. 097001.

[47]   Avraham Klein et al. "Dynamical susceptibility of a near-critical nonconserved order parameter and quadrupole Raman response in Fe-based superconductors". In: *Physical Review B* 98.4 (2018), p. 041101.

[48]   Jiun-Haw Chu et al. "In-plane resistivity anisotropy in an underdoped iron arsenide superconductor". In: *Science* 329.5993 (2010), pp. 824–826.

[49]   MA Tanatar et al. "Uniaxial-strain mechanical detwinning of $CaFe_2As_2$ and $BaFe_2As_2$ crystals: Optical and transport study". In: *Physical Review B* 81.18 (2010), p. 184508.

[50]   MG Kim et al. "Character of the structural and magnetic phase transitions in the parent and electron-doped $BaFe_2As_2$ compounds". In: *Physical Review B* 83.13 (2011), p. 134522.

[51]   Ming Yi et al. "Symmetry-breaking orbital anisotropy observed for detwinned $Ba(Fe_{1-x}Co_x)_2As_2$ above the spin density wave transition". In: *Proceedings of the National Academy of Sciences* 108.17 (2011), pp. 6878–6883.

[52]   S Kasahara et al. "Electronic nematicity above the structural and superconducting transition in $BaFe_2(As_{1-x}P_x)_2$". In: *Nature* 486.7403 (2012), p. 382.

[53]   Jiun-Haw Chu et al. "Divergent nematic susceptibility in an iron arsenide superconductor". In: *Science* 337.6095 (2012), pp. 710–712.

[54]   Jiun-Haw Chu et al. "In-plane electronic anisotropy in underdoped $Ba(Fe_{1-x}Co_x)_2As_2$ revealed by partial detwinning in a magnetic field". In: *Physical Review B* 81.21 (2010), p. 214502.

[55]   T Shimojima et al. "Lifting of xz/yz orbital degeneracy at the structural transition in detwinned FeSe". In: *Physical Review B* 90.12 (2014), p. 121111.

[56]   K Nakayama et al. "Reconstruction of band structure induced by electronic nematicity in an FeSe superconductor". In: *Physical review letters* 113.23 (2014), p. 237001.

[57]   Peng Zhang et al. "Observation of two distinct d_{xz}/d_{yz} band splittings in FeSe". In: *Physical Review B* 91.21 (2015), p. 214503.

[58] M D Watson et al. "Emergence of the nematic electronic state in FeSe". In: *Physical Review B* 91.15 (2015), p. 155106.

[59] SH Baek et al. "Orbital-driven nematicity in FeSe". In: *Nature materials* 14.2 (2015), p. 210.

[60] RM Fernandes et al. "Preemptive nematic order, pseudogap, and orbital order in the iron pnictides". In: *Physical Review B* 85.2 (2012), p. 024534.

[61] CR Rotundu and RJ Birgeneau. "First-and second-order magnetic and structural transitions in $BaFe_{2(1-x)}Co_{2x}As_2$". In: *Physical Review B* 84.9 (2011), p. 092501.

[62] EC Blomberg et al. "Sign-reversal of the in-plane resistivity anisotropy in hole-doped iron pnictides". In: *Nature communications* 4 (2013), p. 1914.

[63] Weicheng Lv and Philip Phillips. "Orbitally and magnetically induced anisotropy in iron-based superconductors". In: *Physical Review B* 84.17 (2011), p. 174512.

[64] C-C Chen et al. "Orbital order and spontaneous orthorhombicity in iron pnictides". In: *Physical Review B* 82.10 (2010), p. 100504.

[65] Eduardo Fradkin et al. "Nematic Fermi fluids in condensed matter physics". In: *Annu. Rev. Condens. Matter Phys.* 1.1 (2010), pp. 153–178.

[66] Jian-Feng Ge et al. "Superconductivity above 100 K in single-layer FeSe films on doped $SrTiO_3$". In: *Nature materials* 14.3 (2015), p. 285.

[67] Defa Liu et al. "Electronic origin of high-temperature superconductivity in single-layer FeSe superconductor". In: *Nature communications* 3 (2012), p. 931.

[68] EM Lifshitz and LP Pitaevskii. *Statistical Physics Part 2: Theory of the condensed state*. 1980.

[69] W Kohn and JM Luttinger. "New mechanism for superconductivity". In: *Physical Review Letters* 15.12 (1965), p. 524.

[70] DS Inosov et al. "Normal-state spin dynamics and temperature-dependent spin-resonance energy in optimally doped $BaFe_{1.85}Co_{0.15}As_2$". In: *Nature Physics* 6.3 (2010), p. 178.

[71] Andrey Chubukov. "Pairing mechanism in Fe-based superconductors". In: *Annu. Rev. Condens. Matter Phys.* 3.1 (2012), pp. 57–92.

[72] Seiichiro Onari and Hiroshi Kontani. "Violation of Anderson's theorem for the sign-reversing s-wave state of iron-pnictide superconductors". In: *Physical review letters* 103.17 (2009), p. 177001.

[73] Hiroshi Kontani and Seiichiro Onari. "Orbital-fluctuation-mediated superconductivity in iron pnictides: analysis of the five-orbital Hubbard-Holstein model". In: *Physical review letters* 104.15 (2010), p. 157001.

[74] Yuki Yanagi, Youichi Yamakawa, and Yoshiaki Ōno. "Two types of s-wave pairing due to magnetic and orbital fluctuations in the two-dimensional 16-band d- p model for iron-based superconductors". In: *Physical Review B* 81.5 (2010), p. 054518.

[75] Alexander F Kemper et al. "Sensitivity of the superconducting state and magnetic susceptibility to key aspects of electronic structure in ferropnictides". In: *New Journal of Physics* 12.7 (2010), p. 073030.

[76] Kazuhiko Kuroki et al. "Pnictogen height as a possible switch between high-T_c nodeless and low-T_c nodal pairings in the iron-based superconductors". In: *Physical Review B* 79.22 (2009), p. 224511.

[77] T Qian et al. "Absence of a holelike Fermi surface for the iron-based $K_{0.8}Fe_{1.7}Se_2$ superconductor revealed by angle-resolved photoemission spectroscopy". In: *Physical review letters* 106.18 (2011), p. 187001.

[78] Alexander A Kordyuk. "Electronic band structure of optimal superconductors: from cuprates to ferropnictides and back again". In: *Low Temperature Physics* 44.6 (2018), pp. 477–486.

[79] IM Lifshitz et al. "Anomalies of electron characteristics of a metal in the high pressure region". In: *Sov. Phys. JETP* 11.5 (1960), pp. 1130–1135.

[80] Daniil V. Evtushinsky et al. "Propeller-Like Low Temperature Fermi Surface of Ba1-x K x Fe2As2 from Magnetotransport and Photoemission Measurements". In: *Journal of the Physical Society of Japan* 80.2 (2011), p. 023710.

[81] DV Evtushinsky et al. "Momentum-resolved superconducting gap in the bulk of Ba1- xKxFe2As2 from combined ARPES and μSR measurements". In: *New Journal of Physics* 11.5 (2009), p. 055069.

[82] S Aswartham et al. "Hole doping in BaFe 2 As 2: the case of Ba 1-x Na x Fe 2 As 2 single crystals". In: *Physical Review B* 85.22 (2012), p. 224520.

[83]   DV Evtushinsky et al. "Electronic band structure and momentum de-
       pendence of the superconducting gap in Ca 1- x Na x Fe 2 As 2 from
       angle-resolved photoemission spectroscopy". In: *Physical Review B* 87.9
       (2013), p. 094501.

[84]   Chang Liu et al. "Importance of the Fermi-surface topology to the su-
       perconducting state of the electron-doped pnictide Ba (Fe 1- x Co x) 2
       As 2". In: *Physical Review B* 84.2 (2011), p. 020509.

[85]   Sergey V Borisenko et al. "One-sign order parameter in iron based
       superconductor". In: *Symmetry* 4.1 (2012), pp. 251–264.

[86]   S Thirupathaiah et al. "Weak-coupling superconductivity in electron-
       doped NaFe 0.95 Co 0.05 As revealed by ARPES". In: *Physical Review
       B* 86.21 (2012), p. 214508.

[87]   C He et al. "Electronic-structure-driven magnetic and structure tran-
       sitions in superconducting NaFeAs single crystals measured by angle-
       resolved photoemission spectroscopy". In: *Physical review letters* 105.11
       (2010), p. 117002.

[88]   A Charnukha et al. "Interaction-induced singular Fermi surface in a
       high-temperature oxypnictide superconductor". In: *Scientific reports* 5
       (2015), p. 10392.

[89]   Andrea Perali et al. "The gap amplification at a shape resonance in a
       superlattice of quantum stripes: A mechanism for high Tc". In: *Solid
       State Communications* 100.3 (1996), pp. 181–186.

[90]   Davide Innocenti et al. "Shape resonance for the anisotropic supercon-
       ducting gaps near a Lifshitz transition: the effect of electron hopping
       between layers". In: *Superconductor Science and Technology* 24.1 (2010),
       p. 015012.

[91]   Davide Innocenti et al. "Resonant and crossover phenomena in a multi-
       band superconductor: Tuning the chemical potential near a band edge".
       In: *Physical Review B* 82.18 (2010), p. 184528.

[92]   Antonio Bianconi. "Quantum materials: Shape resonances in super-
       stripes". In: *Nature Physics* 9.9 (2013), p. 536.

[93]   Rocchina Caivano et al. "Feshbach resonance and mesoscopic phase
       separation near a quantum critical point in multiband FeAs-based su-
       perconductors". In: *Superconductor Science and Technology* 22.1 (2008),
       p. 014004.

[94] Antonio Bianconi et al. "Intrinsic arrested nanoscale phase separation near a topological Lifshitz transition in strongly correlated two-band metals". In: *Superconductor Science and Technology* 28.2 (2015), p. 024005.

[95] XC Wang et al. "The superconductivity at 18 K in LiFeAs system". In: *Solid State Communications* 148.11-12 (2008), pp. 538–540.

[96] Michael J Pitcher et al. "Structure and superconductivity of LiFeAs". In: *Chemical Communications* 45 (2008), pp. 5918–5920.

[97] Joshua H Tapp et al. "LiFeAs: An intrinsic FeAs-based superconductor with T_c= 18 K". In: *Physical Review B* 78.6 (2008), p. 060505.

[98] Igor Morozov et al. "Single crystal growth and characterization of superconducting LiFeAs". In: *Crystal Growth & Design* 10.10 (2010), pp. 4428–4432.

[99] SJ Zhang et al. "Effect of pressure on the iron arsenide superconductor Li_xFeAs (x= 0.8, 1.0, 1.1)". In: *Physical Review B* 80.1 (2009), p. 014506.

[100] Melissa Gooch et al. "Pressure shift of the superconducting T_c of LiFeAs". In: *EPL (Europhysics Letters)* 85.2 (2009), p. 27005.

[101] YM Dai et al. "Spin-Fluctuation-Induced Non-Fermi-Liquid Behavior with Suppressed Superconductivity in $LiFe_{1-x}Co_x$As". In: *Physical Review X* 5.3 (2015), p. 031035.

[102] S Aswartham et al. "Suppressed superconductivity in charge-doped $Li(Fe_{1-x}Co_x)$As single crystals". In: *Physical Review B* 84.5 (2011), p. 054534.

[103] Michael J Pitcher et al. "Compositional control of the superconducting properties of LiFeAs". In: *Journal of the American Chemical Society* 132.30 (2010), pp. 10467–10476.

[104] O Heyer et al. "Resistivity and Hall effect of LiFeAs: Evidence for electron-electron scattering". In: *Physical Review B* 84.6 (2011), p. 064512.

[105] David J Singh. "Electronic structure and doping in $BaFe_2As_2$ and LiFeAs: Density functional calculations". In: *Physical Review B* 78.9 (2008), p. 094511.

[106] Igor Aleksandrovich Nekrasov, Zlata Viktorovna Pchelkina, and Mikhail Vissarionovich Sadovskii. "Electronic structure of new LiFeAs high-T_c superconductor". In: *JETP letters* 88.8 (2008), pp. 543–545.

[107] CW Chu et al. "The synthesis and characterization of LiFeAs and NaFeAs". In: *Physica C: Superconductivity* 469.9-12 (2009), pp. 326–331.

[108]   Hisashi Kotegawa, Hitoshi Sugawara, and Hideki Tou. "Abrupt emer-
        gence of pressure-induced superconductivity of 34 K in $SrFe_2As_2$: A
        resistivity study under pressure". In: *Journal of the Physical Society of
        Japan* 78.1 (2008), p. 013709.

[109]   Kazuyuki Matsubayashi et al. "Intrinsic Properties of A Fe2As2 (A=
        Ba, Sr) Single Crystal under Highly Hydrostatic Pressure Conditions".
        In: *Journal of the Physical Society of Japan* 78.7 (2009), p. 073706.

[110]   F Rullier-Albenque et al. "Hall effect and resistivity study of the mag-
        netic transition, carrier content, and Fermi-liquid behavior in $Ba(Fe_{1-x}Co_x)_2As_2$".
        In: *Physical review letters* 103.5 (2009), p. 057001.

[111]   S Kasahara et al. "Evolution from non-Fermi-to Fermi-liquid trans-
        port via isovalent doping in $BaFe_2(As_{1-x}P_x)_2$ superconductors". In:
        Physical Review B 81.18 (2010), p. 184519.

[112]   FL Pratt et al. "Enhanced superfluid stiffness, lowered superconduct-
        ing transition temperature, and field-induced magnetic state of the
        pnictide superconductor LiFeAs". In: *Physical Review B* 79.5 (2009),
        p. 052508.

[113]   K Umezawa et al. "Unconventional anisotropic s-wave superconduct-
        ing gaps of the LiFeAs iron-pnictide superconductor". In: *Physical Re-
        view Letters* 108.3 (2012), p. 037002.

[114]   RA Jishi and HM Alyahyaei. "Electronic and lattice dynamical prop-
        erties of the iron-based superconductors LiFeAs and NaFeAs". In: *Ad-
        vances in Condensed Matter Physics* 2010 (2010).

[115]   K Kadowaki and SB Woods. "Universal relationship of the resistivity
        and specific heat in heavy-fermion compounds". In: *Solid state com-
        munications* 58.8 (1986), pp. 507–509.

[116]   U Stockert et al. "Specific heat and angle-resolved photoemission spec-
        troscopy study of the superconducting gaps in LiFeAs". In: *Physical
        Review B* 83.22 (2011), p. 224512.

[117]   David J Singh. "Electronic structure of Fe-based superconductors". In:
        Physica C: Superconductivity 469.9-12 (2009), pp. 418–424.

[118]   N Qureshi et al. "Inelastic neutron-scattering measurements of in-
        commensurate magnetic excitations on superconducting LiFeAs sin-
        gle crystals". In: *Physical review letters* 108.11 (2012), p. 117001.

[119] Meng Wang et al. "Effect of Li-deficiency impurities on the electron-overdoped LiFeAs superconductor". In: *Physical Review B* 86.14 (2012), p. 144511.

[120] N Qureshi et al. "Fine structure of the incommensurate antiferromagnetic fluctuations in single-crystalline LiFeAs studied by inelastic neutron scattering". In: *Physical Review B* 90.14 (2014), p. 144503.

[121] J Knolle et al. "Incommensurate magnetic fluctuations and Fermi surface topology in LiFeAs". In: *Physical Review B* 86.17 (2012), p. 174519.

[122] MP Allan et al. "Anisotropic energy gaps of iron-based superconductivity from intraband quasiparticle interference in LiFeAs". In: *Science* 336.6081 (2012), pp. 563–567.

[123] Christian Hess et al. "Interband quasiparticle scattering in superconducting LiFeAs reconciles photoemission and tunneling measurements". In: *Physical review letters* 110.1 (2013), p. 017006.

[124] Torben Hänke et al. "Probing the unconventional superconducting state of LiFeAs by quasiparticle interference". In: *Physical review letters* 108.12 (2012), p. 127001.

[125] Mahmoud Abdel-Hafiez et al. "Superconducting properties of sulfur-doped iron selenide". In: *Physical Review B* 91.16 (2015), p. 165109.

[126] Wilfried Schuster, Helga Mikler, and Kurt L Komarek. "Transition metal-chalcogen systems, VII.: The iron-selenium phase diagram". In: *Monatshefte für Chemie/Chemical Monthly* 110.5 (1979), pp. 1153–1170.

[127] Fong-Chi Hsu et al. "Superconductivity in the PbO-type structure α-FeSe". In: *Proceedings of the National Academy of Sciences* 105.38 (2008), pp. 14262–14264.

[128] Xiaofang Lai et al. "Observation of superconductivity in tetragonal FeS". In: *Journal of the American Chemical Society* 137.32 (2015), pp. 10148–10151.

[129] S Medvedev et al. "Electronic and magnetic phase diagram of β-Fe$_{1.01}$Se with superconductivity at 36.7 K under pressure". In: *Nature materials* 8.8 (2009), p. 630.

[130] S Margadonna et al. "Pressure evolution of the low-temperature crystal structure and bonding of the superconductor FeSe (T$_c$= 37 K)". In: *Physical Review B* 80.6 (2009), p. 064506.

[131] Soon-Gil Jung et al. "Enhanced critical current density in the pressure-induced magnetic state of the high-temperature superconductor FeSe". In: *Scientific reports* 5 (2015), p. 16385.

[132] Yoshikazu Mizuguchi et al. "Substitution effects on FeSe superconductor". In: *Journal of the Physical Society of Japan* 78.7 (2009), pp. 074712–074712.

[133] AV Fedorchenko et al. "Magnetic and superconducting properties of $FeSe_{1-x}Te_x$ ($x \sim 0$, 0.5, and 1.0)". In: *Low Temperature Physics* 37.1 (2011), pp. 83–89.

[134] M D Watson et al. "Suppression of orbital ordering by chemical pressure in $FeSe_{1-x}S_x$". In: *Physical Review B* 92.12 (2015), p. 121108.

[135] Mahmoud Abdel-Hafiez et al. "Impurity scattering effects on the superconducting properties and the tetragonal-to-orthorhombic phase transition in FeSe". In: *Physical Review B* 93.22 (2016), p. 224508.

[136] MA Tanatar et al. "Origin of the resistivity anisotropy in the nematic phase of FeSe". In: *Physical review letters* 117.12 (2016), p. 127001.

[137] R Khasanov et al. "Iron isotope effect on the superconducting transition temperature and the crystal structure of $FeSe_{1-x}$". In: *New Journal of Physics* 12.7 (2010), p. 073024.

[138] Serena Margadonna et al. "Crystal structure of the new $FeSe_{1-x}$ superconductor". In: *Chemical Communications* 43 (2008), pp. 5607–5609.

[139] Ekaterina Pomjakushina et al. "Synthesis, crystal structure, and chemical stability of the superconductor $FeSe_{1-x}$". In: *Physical Review B* 80.2 (2009), p. 024517.

[140] TM McQueen et al. "Tetragonal-to-orthorhombic structural phase transition at 90 K in the superconductor $Fe_{1.01}Se$". In: *Physical Review Letters* 103.5 (2009), p. 057002.

[141] Jasmine N Millican et al. "Pressure-induced effects on the structure of the FeSe superconductor". In: *Solid State Communications* 149.17-18 (2009), pp. 707–710.

[142] Tyrel M McQueen et al. "Extreme sensitivity of superconductivity to stoichiometry in $Fe_{1+\delta}Se$". In: *Physical Review B* 79.1 (2009), p. 014522.

[143] Shinji Kitao et al. "Spin ordering in LaFeAsO and its suppression in superconductor $LaFeAsO_{0.89}F_{0.11}$ probed by Mössbauer spectroscopy". In: *Journal of the Physical Society of Japan* 77.10 (2008), p. 103706.

[144] AE Böhmer et al. "Origin of the tetragonal-to-orthorhombic phase transition in FeSe: A combined thermodynamic and NMR study of nematicity". In: *Physical review letters* 114.2 (2015), p. 027001.

[145] Qisi Wang et al. "Strong interplay between stripe spin fluctuations, nematicity and superconductivity in FeSe". In: *Nature materials* 15.2 (2016), p. 159.

[146] AE Böhmer et al. "Lack of coupling between superconductivity and orthorhombic distortion in stoichiometric single-crystalline FeSe". In: *Physical Review B* 87.18 (2013), p. 180505.

[147] Y Suzuki et al. "Momentum-dependent sign inversion of orbital order in superconducting FeSe". In: *Physical Review B* 92.20 (2015), p. 205117.

[148] Z R Ye et al. "Simultaneous emergence of superconductivity, inter-pocket scattering and nematic fluctuation in potassium-coated FeSe superconductor". In: *arXiv preprint arXiv: 1512.02526* (2015).

[149] HC Xu et al. "Highly Anisotropic and Twofold Symmetric Superconducting Gap in Nematically Ordered $FeSe_{0.93}S_{0.07}$". In: *Physical review letters* 117.15 (2016), p. 157003.

[150] Lin Jiao et al. "Superconducting gap structure of FeSe". In: *Scientific reports* 7 (2017), p. 44024.

[151] Peter O Sprau et al. "Discovery of orbital-selective Cooper pairing in FeSe". In: *Science* 357.6346 (2017), pp. 75–80.

[152] SA Moore et al. "Evolution of the superconducting properties in $FeSe_{1-x}S_x$". In: *Physical Review B* 92.23 (2015), p. 235113.

[153] Shigeru Kasahara et al. "Field-induced superconducting phase of FeSe in the BCS-BEC cross-over". In: *Proceedings of the National Academy of Sciences* 111.46 (2014), pp. 16309–16313.

[154] Udai Raj Singh et al. "Spatial inhomogeneity of the superconducting gap and order parameter in $FeSe_{0.4}Te_{0.6}$". In: *Physical Review B* 88.15 (2013), p. 155124.

[155] Can-Li Song et al. "Direct observation of nodes and twofold symmetry in FeSe superconductor". In: *Science* 332.6036 (2011), pp. 1410–1413.

[156] T Watashige, Y Tsutsumi, T Hanaguri, et al. "Evidence for time-reversal symmetry breaking of the superconducting state near twin-boundary interfaces in FeSe revealed by scanning tunneling spectroscopy". In: *Physical Review X* 5.3 (2015), p. 031022.

[157] K Okazaki et al. "Evidence for a cos(4 φ) Modulation of the Superconducting Energy Gap of Optimally Doped $FeTe_{0.6}Se_{0.4}$ Single Crystals Using Laser Angle-Resolved Photoemission Spectroscopy". In: *Physical review letters* 109.23 (2012), p. 237011.

[158] Hu Miao et al. "Isotropic superconducting gaps with enhanced pairing on electron Fermi surfaces in $FeTe_{0.55}Se_{0.45}$". In: *Physical Review B* 85.9 (2012), p. 094506.

[159] Yue Sun et al. "Symmetry-unprotected nodes or gap minima in the s++ state of monocrystalline FeSe". In: *Physical Review B* 96.14 (2017), p. 140505.

[160] B Zeng et al. "Anisotropic structure of the order parameter in $FeTe_{0.45}Se_{0.55}$ revealed by angle-resolved specific heat". In: *Nature communications* 1 (2010), p. 112.

[161] J-Y Lin et al. "Coexistence of isotropic and extended s-wave order parameters in FeSe as revealed by low-temperature specific heat". In: *Physical Review B* 84.22 (2011), p. 220507.

[162] Edward L Wolf. *Principles of electron tunneling spectroscopy*. Vol. 152. Oxford University Press, 2012.

[163] Heinrich Hertz. "Ueber einen Einfluss des ultravioletten Lichtes auf die electrische Entladung". In: *Annalen der Physik* 267.8 (1887), pp. 983–1000.

[164] Albert Einstein. "Über einen die Erzeugung und Verwandlung des Lichtes betreffenden heuristischen Gesichtspunkt". In: *Annalen der physik* 322.6 (1905), pp. 132–148.

[165] HY Fan. "Theory of photoelectric emission from metals". In: *Physical Review* 68.1-2 (1945), p. 43.

[166] Peter J Feibelman and DE Eastman. "Photoemission spectroscopy — correspondence between quantum theory and experimental phenomenology". In: *Physical Review B* 10.12 (1974), p. 4932.

[167] M Pl Seah and WA Dench. "Quantitative electron spectroscopy of surfaces: A standard data base for electron inelastic mean free paths in solids". In: *Surface and interface analysis* 1.1 (1979), pp. 2–11.

[168] W. Heisenberg. "Über den anschaulichen Inhalt der quantentheoretischen Kinematik und Mechanik". In: *Zeitschrift für Physik* 43.3 (1927), pp. 172–198.

[169] Friedrich Reinert and Stefan Hüfner. "Photoemission spectroscopy—from early days to recent applications". In: *New Journal of Physics* 7.1 (2005), p. 97.

[170] Mohit Randeria et al. "Momentum distribution sum rule for angle-resolved photoemission". In: *Physical review letters* 74.24 (1995), p. 4951.

[171] Neville V Smith and Morton M Traum. "Angular Dependence of Photoemission from the (110) Face of GaAs". In: *Physical Review Letters* 31.20 (1973), p. 1247.

[172] G Beamson et al. "Performance and application of the scienta ESCA300 spectrometer". In: *Surface and Interface Analysis* 15.9 (1990), pp. 541–549.

[173] *www.scientaomicron.com*. https://www.scientaomicron.com/en/products/353/1170.

[174] M Hoesch et al. "A facility for the analysis of the electronic structures of solids and their surfaces by synchrotron radiation photoelectron spectroscopy". In: *Review of Scientific Instruments* 88.1 (2017), p. 013106.

[175] SV Borisenko. ""One-cubed" ARPES User Facility at BESSY II". In: *Synchrotron Radiation News* 25.5 (2012), pp. 6–11.

[176] *www.diamond.ac.uk*. https://www.diamond.ac.uk/.

[177] Shigemi Sasaki. "Analyses for a planar variably-polarizing undulator". In: *Nuclear Instruments and Methods in Physics Research Section A: Accelerators, Spectrometers, Detectors and Associated Equipment* 347.1-3 (1994), pp. 83–86.

[178] YS Kushnirenko et al. "Anomalous temperature evolution of the electronic structure of FeSe". In: *Physical Review B* 96.10 (2017), p. 100504.

[179] A Fedorov et al. "Effect of nematic ordering on electronic structure of FeSe". In: *Scientific reports* 6 (2016), p. 36834.

[180] R S Dhaka et al. "Unusual Temperature Dependence of Band Dispersion in Ba(Fe$_{1-x}$Ru$_x$)$_2$As$_2$ and its Consequences for Antiferromagnetic Ordering". In: *Physical review letters* 110.6 (2013), p. 067002.

[181]   Yu V Pustovit and A A Kordyuk. "Metamorphoses of electronic structure of FeSe-based superconductors (Review Article)". In: *Low Temperature Physics* 42.11 (2016), pp. 995–1007.

[182]   Rafael M Fernandes and Oskar Vafek. "Distinguishing spin-orbit coupling and nematic order in the electronic spectrum of iron-based superconductors". In: *Physical Review B* 90.21 (2014), p. 214514.

[183]   YS Kushnirenko et al. "Three-dimensional superconducting gap in FeSe from angle-resolved photoemission spectroscopy". In: *Physical Review B* 97.18 (2018), p. 180501.

[184]   D V Evtushinsky et al. "Fusion of bogoliubons in $Ba_{1-x}KxFe_2As_2$ and similarity of energy scales in high temperature superconductors". In: *arXiv preprint arXiv: 1106.4584* (2011).

[185]   Sergey V Borisenko. "Superconductivity: Fewer atoms, more information". In: *Nature materials* 12.7 (2013), pp. 600–601.

[186]   DV Evtushinsky et al. "Strong electron pairing at the iron $3d_{xz,yz}$ orbitals in hole-doped $BaFe_2As_2$ superconductors revealed by angle-resolved photoemission spectroscopy". In: *Physical Review B* 89.6 (2014), p. 064514.

[187]   Shantanu Mukherjee et al. "Model of electronic structure and superconductivity in orbitally ordered FeSe". In: *Physical review letters* 115.2 (2015), p. 026402.

[188]   Andreas Kreisel et al. "Orbital selective pairing and gap structures of iron-based superconductors". In: *Physical Review B* 95.17 (2017), p. 174504.

[189]   Zhe Wang et al. "Tuning orbital-selective correlations in superconducting $R_{0.75}Fe_{1.6}Se_{2-z}S_z$". In: *Physical Review B* 93.10 (2016), p. 104522.

[190]   Ming Yi et al. "Observation of universal strong orbital-dependent correlation effects in iron chalcogenides". In: *Nature communications* 6 (2015), p. 7777.

[191]   Jian Kang, Rafael M Fernandes, and Andrey Chubukov. "Superconductivity in FeSe: the role of nematic order". In: *Physical review letters* 120.26 (2018), p. 267001.

[192]   MR Norman et al. "Momentum distribution curves in the superconducting state". In: *Physical Review B* 64.18 (2001), p. 184508.

[193] AV Chubukov and MR Norman. "Dispersion anomalies in cuprate superconductors". In: *Physical Review B* 70.17 (2004), p. 174505.

[194] YS Kushnirenko et al. "Superconductivity-induced nematicity". In: *arXiv preprint arXiv:1810.04446* (2018).

[195] Daniil Evtushinsky. "Physical properties of layered superconductors from angle-resolved photoemission spectroscopy". PhD thesis. Zellescher Weg 12-14, 01062 Dresden, Germany: Fakultät Mathematik und Naturwissenschaften Der Technische Universität Dresden, 2011.

[196] AA Kordyuk et al. "Measuring the gap in angle-resolved photoemission experiments on cuprates". In: *Physical Review B* 67.6 (2003), p. 064504.

Acknowledgements

I would like to thank Prof. Bernd Büchner for the possibility to make studies at IFW Dresden. This work would not have been possible without the supervision and support of Dr. Sergey Borysenko the head of Synchrotron methods group. I also thank all my colleagues, and especially E. Haubold, A.V. Fedorov, and S. Thirupathaiah.

I am grateful to S. Aswartham, I. Morozov, and T. Wolf for providing me with high-quality single-crystal samples for my studies and to R. Hübel, M. Nauman, and S. Leger for the technical support.

I also acknowledge following collaborations: T. Kim (Diamond Light Source), E. Rienks (Helmholtz-Zentrum Berlin), and D. V. Evtushinsky (Helmholtz-Zentrum Berlin) for support at the synchrotrons and fruitfully discussions, A.V. Chubukov (University of Minnesota) for developing the theoretical explanation of the effects observed by us in LiFeAs, A. Yaresko (Max Planck Institute) for the DFT calculations.

This work was supported by DFG No. BO1912/6-1 and SPP1458.

Symbols and abbreviations

ARPES	Angle-resolved photoemission spectroscopy
STS / STM	scanning tunneling spectroscopy / microscopy
QPI	quasiparticle interference
LDA	local density approximation
DFT	density functional theory
IBS	iron-based superconductor / superconductors
BZ	Brillouin zone
EDC	energy distribution curve
MDC	momentum distribution curve
SDW	Spin density wave
T_c	critical temperature (superconducting transition temperature)
T_{nem}	temperature of the nematic transition
T_{mag}	temperature of the magnetic transition
k_x, k_y, k_z	three components of the momentum of an electron
k_F	Fermi momentum (momentum at which a dispersion crosses the Fermi Level)

Publication List

- S. Thirupathaiah, D. Efremov, Y. Kushnirenko, E. Haubold, T.K. Kim, B.R. Pienning, I. Morozov, S. Aswartham, B. Büchner, S.V. Borisenko "Massive Dirac fermions in layered $BaZnBi_2$". In: *Physical Review Materials* 3, 024202 (2019)

- Y.S. Kushnirenko, D.V. Evtushinsky, T.K. Kim, I.V. Morozov, L. Harnagea, S. Wurmehl, S. Aswartham, A.V. Chubukov, S.V. Borisenko "Superconductivity-induced nematicity". In: *arXiv preprint arXiv:1810.04446* (2018)

- Y.S. Kushnirenko, A. V. Fedorov, E. Haubold, S. Thirupathaiah, T. Wolf, S. Aswartham, I. Morozov, T. K. Kim, B. Büchner, and S.V. Borisenko "Three-dimensional superconducting gap in FeSe from angle-resolved photoemission spectroscopy". In: *Physical Review B* 97, 180501 (2018)

- S. Thirupathaiah, I. Morozov, Y. Kushnirenko A.V. Fedorov, E. Haubold, T.K. Kim, G. Shipunov, A. Maksutova, O. Kataeva, S. Aswartham, B. Büchner, and S.V. Borisenko "Spectroscopic evidence of topological phase transition in the three-dimensional Dirac semimetal $Cd_3(As_{1-x}P_x)_2$". In: *Physical Review B* 98, 085145 (2018)

- S. Thirupathaiah, Y. Kushnirenko, E. Haubold, A.V. Fedorov, E.D.L. Rienks, T.K. Kim, A.N. Yaresko, C.G.F. Blum, S. Aswartham, B. Büchner, and S. V. Borisenko "Possible origin of linear magnetoresistance: Observation of Dirac surface states in layered $PtBi_2$". In: *Physical Review B* 97, 035133 (2018)

- A. Fedorov, A. Yaresko, E. Haubold, Y. Kushnirenko, T. Kim, B. Buechner, S. Aswartham, S. Wurmehl, S. Borisenko "Energy scale of nematic ordering in the parent iron-based superconductor:$BaFe_2As_2$". In: *arXiv preprint arXiv:1811.02430* (2018)

- E. Haubold, A. Fedorov, I.P. Rusinov, T.V. Menshchikova, V. Duppel, D. Friedrich, F. Pielnhofer, R. Weihrich, A. Pfitzner, A. Zeugner, A. Isaeva, S. Thirupathaiah, Y. Kushnirenko, E. Rienks, T. Kim, E. V. Chulkov, B.

Büchner, S.V. Borisenko "Possible Experimental Realization of a Basic Z2 Topological Semimetal". In: *arXiv preprint arXiv:1812.01668* (2018)

- <u>Y.S. Kushnirenko</u>, A.A. Kordyuk, A.V. Fedorov, E. Haubold, T. Wolf, B. Büchner, and S.V. Borisenko "Anomalous temperature evolution of the electronic structure of FeSe". In: *Physical Review B* 96, 100504(R) (2017)

- E. Haubold, K. Koepernik, D. Efremov, S. Khim, A. Fedorov, <u>Y. Kushnirenko</u>, J. van den Brink, S. Wurmehl, B. Büchner, T.K. Kim, M. Hoesch, K. Sumida, K. Taguchi, T. Yoshikawa, A. Kimura, T. Okuda, and S.V. Borisenko "Experimental realization of type-II Weyl state in noncentrosymmetric TaIrTe$_4$". In: *Physical Review B* 95, 241108 (2017)

- A. Fedorov, A. Yaresko, T. K. Kim, <u>Y. Kushnirenko</u>, E. Haubold, T. Wolf, M. Hoesch, A. Grüneis, B. Büchner, S. V. Borisenko "Effect of nematic ordering on electronic structure of FeSe". Scientific reports 6, 36834 (2016)

- R. Lou, Z. Liu, W. Jin, H. Wang, Z. Han, K. Liu, X. Wang, T. Qian, <u>Y. Kushnirenko</u>, S.-W. Cheong, R M. Osgood Jr., H. Ding, and S. Wang "Sudden gap closure across the topological phase transition in Bi$_{2-x}$In$_x$Se$_3$". In: *Physical Review B* 92, 115150 (2015)

Versicherung

Hiermit versichere ich, dass ich die vorliegende Arbeit ohne unzulässige Hilfe Dritter und ohne Benutzung anderer als der angegebenen Hilfsmittel angefertigt habe; die aus fremden Quellen direkt oder indirekt übernommenen Gedanken sind als solche kenntlich gemacht. Die Arbeit wurde bisher weder im Inland noch im Ausland in gleicher oder ähnlicher Form einer anderen Prüfungsbehörde vorgelegt.

Die Dissertation wurde am Leibniz-Institut für Festkörper- und Werkstoffforschung Dresden unter Betreuung von Dr. Sergey Borisenko und Prof. Dr. Bernd Büchner angefertigt.

Unterschrift:

_____

Datum:

_____